Invention and Advancement of Sonoselective Focused Ultrasound for Transfection of the Cerebral Vasculature

---

A

Dissertation

Presented to

the faculty of the School of Engineering and Applied Science

University of Virginia

---

in partial fulfillment

of the requirements for the degree

Doctor of Philosophy

by

Catherine Gorick

August 2021

APPROVAL SHEET

This

Dissertation

is submitted in partial fulfillment of the requirements
for the degree of

Doctor of Philosophy

Author: Catherine Gorick

This Dissertation has been read and approved by the examing committee:

Advisor: Richard Price

Advisor:

Committee Member: Jeffrey Saucerman

Committee Member: Gary Owens

Committee Member: Mete Civelek

Committee Member: John Lukens

Committee Member:

Committee Member:

Accepted for the School of Engineering and Applied Science:

Craig H. Benson, School of Engineering and Applied Science

August 2021

Acknowledgements

I owe a debt of gratitude to so many people for their support, scientific or otherwise, over the course of my PhD journey. First and foremost, I must acknowledge and thank my advisor, Dr. Richard Price. Graduate school is a miserable journey sometimes, but you never contributed to that. Instead, you were patient and supportive and available to offer advice at any time. You gave me the freedom to try new things without being afraid to fail, which is perhaps the greatest gift a scientist can receive. Thank you for building up my confidence to pursue my own ideas, even when we were both in way over our heads. Second, I have to thank Ji Song for being an absolute wizard at the bench as well as an organizational mastermind, and facilitating all of the lab's research behind the scenes. It's my goal to be as skilled a researcher as you one day, and I'm honored to call you my friend.

I would also like to thank my entire committee, past and present. Dr. Saucerman, Dr. Owens, Dr. Civelek, Dr. Lukens, and Dr. Kalani – thank you for your guidance, advice, and for putting up with the pain of scheduling my defense. In particular, thank you to Dr. Saucerman for your invaluable advice on the conception and development of the computational model featured in Chapter 5 of this thesis. Your willingness to help and advise even amidst the craziness of the early pandemic days is truly appreciated.

Thank you to our collaborators for their absolutely crucial contributions to these projects. My work (and the lab's as a whole) would be nowhere without the tremendous skills of Dr. Wilson Miller and Will Garrison. Thank you for the long hours in the Snyder basement, the humor that kept me sane, and for explaining the basics of MRI to me for the 100th time. Thank you also to Dr. Petr Tvrdik and Dr. Khadijeh Sharifi. You've taught me more about the brain than I ever could've imagined, have helped take FUS into brand new biological applications, and are two of the smartest people I've ever met. Thank you to Jeremy Gatesman, the tail vein wizard himself, for the vital assistance with all of our animal projects and for being a ray of light in the middle of long experiment days.

Next, I would like to thank the Price Lab students (#PriceLabSolidarity). The advice I received when selecting a lab for graduate school was that "Everyone's research sucks some days. Choose the people you want to be around on those days." I took that advice and I've never regretted it. Thank you to Kelsie Timbie, Brian Mead, and Colleen Curley for teaching me the ropes of focused ultrasound and gene delivery. Thank you to Josh Heuslein for your incredible patience with me as a novice graduate student, for giving me opportunities to get

involved, and for never making me feel like an idiot when I had silly questions. Thank you to Natasha Sheybani for the years of JV office fun and commiseration, for being my go-to roommate at conferences, and for always inspiring me to do my best. Thank you to Alex Mathew for being my longest-running collaborator (I still don't understand boron nanoparticles), for answering all of my nonsensical medical questions, and for your genuine warmth and kindness over the years. Thank you to Andrew Thim for being the only real contributor to our tug-of-war team, for turning everyone's PCD data into something meaningful, and for always being willing to help anyone with anything. Thank you to Delaney Fisher for being the best roommate/co-worker a gal could ask for, for demonstrating how to correctly draw a brain, and for setting an example of the kind of woman in STEM I aspire to be. Thank you to Tor Breza for brightening up the lab with your art, for always being down for a coffee walk, and for motivating us all to get fit during quarantine. Thank you to Mark Schwarz and Anna Debski for making me smile every day, for teaching me a thing or two about cell culture, and for putting up with doing Maxipreps with me for hours on end. Thank you to Kathy Nowak for your hilarious honesty, for bringing some BIMS wisdom into our engineering lab, and for sharing pictures of your adorable dog.

I want to thank the undergraduate students I've worked with, as well. Over the course of four Capstone teams and multiple independent research projects, I've had the honor of getting to know and work with 11 of you personally. It's been a privilege and a highlight of my graduate school career to watch you all develop your skills as scientists, and I can't wait to see what you all accomplish in your careers. In particular, thank you to Caitleen Copeland and Rebecca Della Croce for putting up with me and my bad jokes for so many years. I promise someday I'll remember whether or not you're lefthanded.

Finally, I must express my gratitude to my family, who for years now have supported me in my never-ending quest for more education. I would be nowhere without their love and encouragement. Thank you to Mom and Dad for doing your best not to ask me when I'll be done with the degree, and for giving me the confidence that I can accomplish anything I set my mind to. Thank you to my siblings, Carolyn and Will, for always being available to listen to me vent and for sending me funny pictures to make me smile. Thank you to my classmate, best friend, and husband, Lee, for supporting me through the ups and downs of the past 6 years and for helping to co-parent our very good dog.

I couldn't have done it without every single one of you. Thank you.

Table of Contents

Chapter 1: Preface

1.1 Abstract

Many pathologies of the brain, including neurodegenerative diseases, glioma, and stroke, are characterized by both devastating daily effects for patients and daunting challenges and limitations to treatment for physicians. The endothelial cells of the brain serve many important functions (in both normal physiology and in disease), including comprising the BBB and regulating blood flow and nutrient exchange, and maintaining cerebral homeostasis. Treatment of many pathologies of the brain could be improved markedly by the development of non-invasive therapeutic approaches that elicit robust, endothelial cell-selective, gene expression in specific regions of the brain. Focused ultrasound (FUS) in conjunction with gas-filled microbubbles (MBs) has emerged as a non-invasive modality for MR image-guided gene delivery to the brain, by transiently disrupting the BBB to facilitate transport of gene products into the brain parenchyma. However, this disruption may induce inflammatory responses.

In the first aim of this dissertation, we introduce a new MR image-guided FUS method that elicits endothelial-selective transfection of the cerebral vasculature (i.e. “sonoselective” transfection), without opening the BBB. We demonstrate that activating circulating, cationic plasmid-bearing, MBs with pulsed very low-pressure FUS facilitates sonoselective gene delivery to the endothelium without MRI-detectable disruption of the BBB. The degree of endothelial selectivity varies inversely with the FUS pressure, with higher pressures consistently inducing BBB opening and extravascular transfection. Bulk RNA sequencing analyses reveals that the sonoselective low pressure regimen does not upregulate inflammatory or immune responses. This approach permits targeted gene delivery to blood vessels and could be used to facilitate gene therapy for a variety of brain pathologies where BBB disruption is contraindicated.

Next, in the second aim of this thesis, we seek to better characterize the effects of FUS-mediated BBB opening, and the ways in which different peak-negative pressures (PNPs) of

FUS affect transfected cell populations Following plasmid delivery to and across the BBB with FUS, we use single cell RNA-sequencing to identify the different populations of transfected cells, which prove to be highly dependent on PNP. Cells of the BBB (i.e. endothelial cells, pericytes, and astrocytes) are enriched following 0.1 and 0.2 MPa FUS, while transfection of cells distal to the BBB (i.e. neurons, oligodendrocytes, and microglia) is augmented at 0.4 MPa. Pressure-dependent differential gene expression is observed for multiple cell types, with cell stress genes upregulated proportionally to PNP, independent of cell type. These results underscore how FUS may be tuned to bias transfection toward specific brain cell types in-vivo and predict how those cells will respond to transfection.

Although many signaling pathways in brain endothelial cells have been implicated in disease, optimal molecular targets for endothelial cell-based drug or gene therapy can be difficult to determine. To address this need, in the third aim of this dissertation, we develop a large-scale computational model of brain endothelial cell signaling, capable of identifying the most influential molecules for pharmaceutical targeting to promote therapeutic changes in the endothelial cell phenotype. The model, which integrates 63 nodes and 82 reactions, is validated against independent literature studies, with the model yielding correct predictions 73% of the time. We use the model to identify influential and sensitive nodes under different physiological or pathological contexts, including glioma, Alzheimer's disease, and ischemic stroke. We then identify nodes (or combinations of nodes) with the greatest influence over combinations of desired model outputs as potential druggable targets for these disease conditions.

In summary, these studies develop a novel platform for targeted transfection of the cerebral vasculature with FUS, characterize the responses of individual brain cell populations to FUS and MBs, and permit predictions of the impacts of different FUS-mediated therapeutic interventions on brain endothelial cells in a variety of disease contexts.

1.2 Preview of Dissertation

In Chapter 2 of this dissertation, we will introduce topics related to diseases of the central nervous system and associated drug and gene delivery challenges. We review the structure of the BBB, the use of FUS and MBs for BBB disruption, and FUS-mediated delivery of gene products to the brain. Chapter 3 will discuss the development of a platform for targeted transfection of the cerebral vasculature without BBB disruption using low-pressure MRI-guided FUS in conjunction with MBs electrostatically conjugated to plasmids of interest, as well as characterization of bulk brain transcriptomic responses to FUS-mediated MB activation at different peak-negative pressures. In Chapter 4, we conduct a single cell transcriptomic analysis of the different cell types transfected by FUS and MB BBB opening at different pressures, addressing both the change in transfected cell types and both cell-type-specific and brain-wide changes in transcription following FUS. Chapter 5 details the development of a large scale computational model of brain endothelial cell signaling, which can be used to predict the effects of pharmaceutical interventions and FUS-mediated gene delivery on the endothelium in the context of multiple disease states. Lastly, Chapter 6 will explore future research questions related to the findings in this dissertation.

Chapter 2: Introduction

2.1 Clinical Significance

Many pathologies of the brain are characterized by both devastating daily effects for patients as well as daunting challenges and limitations to treatment for physicians. Neurodegenerative diseases, including dementia, Alzheimer's, Parkinson's, and Huntington's, affect an increasing proportion of society as the global population ages. These conditions cause a host of debilitating symptoms, including impairments to memory and cognitive abilities, and limitations to the patient's ability to move, speak, or breathe(1, 2). Primary and metastatic brain tumors are associated with low survival rates even with aggressive standard-of-care therapy. Glioblastoma, the most common malignant primary brain tumor, has a median survival rate of just 15 months(3, 4). Ischemic and hemorrhagic strokes affect over 16 million people each year, and are a leading cause of death and disability worldwide(5, 6). These conditions vary widely in their incidence, molecular mechanisms, and progression, and yet all remain inherently difficult to treat. At least some of the challenge of treatment rests in the nature of the brain structure itself, and more specifically, the blood-brain barrier.

2.2 The Blood-Brain Barrier

The brain is a particularly well-protected organ, making its treatment an especially formidable challenge. The root of this protection is the blood-brain barrier (BBB), which prevents penetration of the vast majority of systemically administered therapeutics into the brain parenchyma(7). We ascribe the term "blood-brain barrier" to the network of blood vessels that support the central nervous system (CNS), referring to their unique properties that allow for precise control over the transport of molecules and cells to and from the brain. This tight regulation helps provide the ideal environment for sensitive neural cells by maintaining specific concentrations of solutes and neurotransmitters, and protecting the CNS from damage that could be induced by circulating toxins or pathogens(8, 9).

The primary physiological basis of the BBB is the continuous, non-fenestrated layer of brain capillary endothelial cells which line the cerebral microvasculature. The endothelial cells which make up the capillaries of the brain are notably much thinner than the endothelium of other tissues(10), and highly polarized(11, 12). Brain endothelial cells are held together by tight junctions, which consist of several proteins including claudins, occludins, and junctional adhesion molecules (JAMs)(13). These tight junctions serve as a barrier to paracellular passive diffusion of materials from the systemic circulation into the surrounding brain tissue. Small lipid soluble molecules can diffuse across the endothelium, and most other substances, including the nutrients required for neural cell function, must be actively transported across the CNS endothelial cells(14). The brain endothelium also expresses drug efflux pumps, such as p-glycoprotein, to continuously remove potentially harmful materials from the CNS(15). Thus, in essence, brain endothelial cells are the gatekeepers to the brain – the only mechanisms by which molecules can reach the brain are through the endothelial cells themselves. Finally, the BBB is further supported by interactions between the endothelial cells and surrounding pericytes, astrocytes, and a continuous basement membrane which further make up the neurovascular unit (NVU)(16, 17).

Clearly, the CNS has adapted a highly effective system for maintaining brain tissue homeostasis. While the BBB protects the cerebral parenchyma from potentially neurotoxic materials, it is also represents a barrier to therapeutic delivery for brain pathologies. The BBB is only naturally permeable to very small lipophilic molecules that can freely diffuse across the endothelial cell membranes. As such, the structure of the intact BBB serves to block more than 98% of small molecule drugs and 100% of large molecule therapeutics from entering the brain tissue from the systemic circulation(7).

2.3 Conventional Methods of Bypassing the Blood-Brain Barrier

While the BBB provides many physiological benefits by maintaining proper homeostasis of metabolites and nutrients, as well as blocking dangerous substances from accessing sensitive brain tissue, there are many occasions where it hinders therapy for diseases of the CNS. In the case of these often serious and potentially fatal conditions, the risks associated with BBB disruption may pale in comparison to the potential benefits of an effective therapeutic delivery. For these reasons, clinicians and researchers alike have long sought out safe and reproducible methods of disrupting, permeabilizing, or bypassing the BBB to deliver drugs, genes, proteins, or even cells to help treat disease or injury. In this section, we will review a number of these methods and their relative strengths and weaknesses.

2.3.1 Trans-Cranial Drug Delivery

Perhaps the most immediately obvious solution to limited transport across the BBB is direct delivery of the therapeutic molecule to the disease site via transcranial injection or implantation. Such direct intracranial administration permits high local concentrations of drug without the potential off-target effects of systemic delivery. Drug-releasing devices or materials can be directly implanted into resected brain tissue. Such approaches have, for example, been employed to release chemotherapeutics directly at the site of a prior glioma(18, 19) or provide dopamine directly to neurons in Parkinson's patients(20, 21). Unfortunately, these implants are severely limited by the minimal degree of diffusion of drugs and therapeutic molecules that can occur over large distances in brain parenchyma. Indeed, the vast majority of small molecules or proteins released by these implants remains concentrated within 2-5 millimeters of the implant itself(22, 23). Injections of therapeutics directly into the ventricles of the brain, which produce and transport cerebrospinal fluid, are similarly limited in their drug penetration and distribution(24–26).

Compared to other direct injection approaches, convection-enhanced delivery has demonstrated enhanced drug distribution into CNS tissue(27, 28). This technique generates bulk flow through hydrostatic pressure differentials to force fluid through the brain, carrying drugs further into the brain parenchyma. This method has been explored in both clinical and preclinical trials(29, 30), but is still limited by high levels of risk associated with surgical complications in the brain. In particular, the concern over morbidity associated with intracranial surgery makes these direct local applications unappealing for drugs which need to be applied across a large area, or which need to dosed repeatedly.

2.3.2 Systemic BBB Disruption

As direct injection has been shown to carry significant risks associated with transcranial surgery, non-surgical strategies have arisen to enhance transport across the BBB. One such option is to deliver a hypertonic solution, such as mannitol, into the bloodstream. Such solutions induce the osmotic shrinkage of endothelial cells, physically disrupting the tight junctions to create fenestrations in the vasculature, and allow paracellular transport of drugs or therapeutics into the surrounding tissue(31, 32). However, this approach is associated with toxicity to the brain, including inducing vasculopathy(33), chronic neuropathologic changes(32), and seizures(34). Bradykinin-like molecules have also been studied as a potential pharmacological disruptor of the BBB, as these molecules can induce both vasodilatory effects and disruption of tight junction structure via activation of nitric oxide synthase. These effects enhance paracellular diffusion of drugs into the BBB(35, 36). However, this approach is more effective in tumors than normal brain tissue(37), and clinical trials of bradykinin analogs in glioma have shown limited effectiveness(38). Additionally, like mannitol, risks associated with brain-wide BBB disruption are of concern.

2.3.3. Intranasal Delivery

An alternative non-invasive method of drug delivery to the brain is intranasal administration. The rationale behind this approach is that drugs may pass through the submucous space of the nose, across the nasal epithelium, and across the arachnoid membrane to enter into the olfactory cerebrospinal fluid (CSF). The drug could then exit the CSF into the brain tissue similarly to an intraventricular injection(7). However, drugs delivered in this manner still face the same challenges associated with diffusion from the CSF. An additional limitation is that the arachnoid membrane is heavily lined with tight junctions which prevent large molecules from crossing into the olfactory CSF(39). While intranasal delivery has many attractive advantages, including ease and safety of administration, the relatively small number of molecules that can cross the olfactory epithelium and arachnoid membrane greatly limits its application.

2.4. Focused Ultrasound-Mediated BBB Disruption

In response to limitations of many pre-existing methods of bypassing the BBB, focused ultrasound (FUS) has arisen as an attractive alternative approach to deliver drugs and genes to specific regions of the brain in a targeted, noninvasive, and repeatable manner. In conjunction with gas-filled microbubbles and magnetic resonance imaging (MRI) for guidance, this technique is now widely used to open the BBB for therapeutic delivery in a host of different pathologies. It has gained significant traction in clinical trials of individuals with Alzheimer's disease(40), amyotrophic lateral sclerosis (ALS)(41), and brain tumors(42).

2.4.1. History and Principles of Focused Ultrasound

Ultrasound consists of pressure waves occurring at frequencies beyond the scope of human hearing. An ultrasound waveform is transmitted into a region of interest when specific piezoelectric elements positioned on the face of a transducer are activated by an appropriate electrical signal. The generated acoustic energy propagates through the tissue, encountering regions of varying acoustic (i.e., mechanical) impedance. These mechanical heterogeneities modify the ultrasound beam through attenuation and diffraction as well as reflection and scattering. In diagnostic ultrasound imaging, reflected and scattered energy returns to the transducer, which now behaves as a receiver, converting the mechanical acoustic energy into electrical energy. A meaningful image can then be displayed when these electrical signals are processed appropriately. Following decades of technological innovation and testing, ultrasound began seeing use as a diagnostic medical tool in the 1940s and 1950s, when it was utilized to image internal organ structures, ovarian cysts, and developing fetuses(43).

In contrast to diagnostic ultrasound, which most frequently utilizes a flat transducer face to produce and receive planar pressure waves, focused ultrasound (FUS) refers to the use of a curved or spherical transducer to concentrate the waves within a relatively small volume (modern devices have sub-millimeter precision). This energy deposition in a small volume can produce heat or mechanical disruption of the tissue within the focus. The concept of focusing ultrasound has existed since the 1930s, but was first actualized for therapeutic use in humans in the 1950s and 1960s, when high intensity FUS was utilized to lesion the brain in patients with severe pain or Parkinson's(44). However, in this early era of the technology, there was little to no image guidance associated with treatments, which severely limited the technology's application. While FUS continued to be developed and used as a method for ablating tumors in the body for decades (up to and including present day), its applications in the brain largely stagnated until the 1990s. In 1992, it was combined with MRI guidance for the first time, and the field of FUS for neurological applications began in earnest(45). A few years later, in 2001, the

concept of using FUS to safely and reversibly disrupt the blood-brain barrier was demonstrated by Kullervo Hynynen(46). With further refinement and investigation over the next 2 decades, FUS-mediated drug delivery to the brain in humans has been made possible.

Reflection and diffraction of ultrasound waves at material interfaces (i.e. skull-tissue interface) can distort the focus and decrease the energy delivered at the target. While the rodents used in many pre-clinical studies have skull thicknesses thin enough to allow for the use of single-element transducers for treatment, the far thicker bone and more complex topography of the human skull requires the use of a multi-element array (often with phase-correction software) to refocus the ultrasound beam as it passes through the skull. There are many combinations of FUS parameters (frequency, pressure, pulsing protocol) suitable for FUS-mediated BBB disruption (a number of which will be discussed later in this dissertation), but lower frequencies (≤1.0 MHz) experience less attenuation and distortion by the skull(47).

2.4.2. Mechanisms of FUS-Mediated BBB Opening

As an ultrasound wave passes through tissue, that tissue experiences alternating periods of high pressure (compression) and low pressure (rarefaction). After many years of use as a minimally invasive imaging modality, it was discovered that ultrasound in conjunction with FDA-approved gas-filled contrast agent microbubbles (which enhance blood echogenicity and, consequently, the contrast between tissues during an ultrasound exam) could also be used for other applications. These microbubbles (MBs) are often a few microns in diameter, and typically consist of a lipid or protein shell surrounding an inert perfluorocarbon gas core. The MBs circulating within the bloodstream can be destroyed by ultrasound waves, facilitating the assessment of tissue perfusion by its correlation to MB replenishment in a given region(48, 49). Concerns about the possible deleterious bioeffects from ultrasonic MB destruction fueled investigations into the impact of this phenomenon on surrounding tissues. Observations from these studies have shown that localized regions of microvessels experienced increases in

permeabilization as indicated by red blood cell (RBC) extravasation from sites of intravascular ultrasound + MB interactions(50–53). Based on these findings, significant interest was generated in possibly exploiting these ultrasound + MB-induced bioeffects for beneficial purposes. It was discovered that the gas-filled MBs could be used in combination with low-power FUS in the brain to disrupt the BBB, without inducing further tissue damage(54).

Interactions between relatively low-power ultrasound and circulating MBs elicit a range of bioeffects through mechanisms that remain only partially understood(55, 56). Studies of ultrasound + MBs in peripheral (non-CNS) tissues revealed an increase in microvascular permeability(51, 52), hemolysis (i.e., RBC destruction)(57–60) and arterial vasospasms(61) near sites of ultrasound + MB interactions. Additionally, cavitation of MBs by ultrasound may cause free radical production(62–64), heating(65–67), shockwave emanation resulting in microstreaming(68–70), and bubble fragmentation producing microjets(56, 71). These effects may individually or collaboratively impact the surrounding microenvironment to elicit tissue level consequences (e.g., capillary disruptions, wound healing pathways, hemostasis, inflammation signaling pathways).

In the brain, there has been extensive pre-clinical research dedicated to investigating the mechanisms by which low pressure FUS and stably oscillating MBs induce BBB disruption. The disruption is thought to be due to three key phenomena: disruption of tight junctional protein complexes, enhanced transcytosis, and sonoporation of endothelial cell membranes. Following FUS with MBs, the level of tight junctional proteins is reduced in BBB vessels, and the distribution of these proteins is altered, with reduced clustering at the edges of the endothelial cells(72). The reduced levels of claudins and occludins at the endothelial cell edges indicates a reduction in functional tight junction complexes. This functional loss of BBB integrity was confirmed by the observation of intravenously delivered horseradish peroxidase and lanthanum chloride leaking into the brain parenchyma, which continued for about two to four hours, then stopped – thought to reflect the time for the tight junctions to reform and BBB integrity to be

reestablished(72). In addition to the paracellular transport evidenced by the leakage into the brain parenchyma, studies have indicated that increased expression of caveolin-1 following FUS activation of MBs can enhance transcellular transport in brain endothelial cells via caveolae(73). Studies have also demonstrated direct sonoporation of the endothelial cell membrane, allowing for uptake of drugs or genes by the brain endothelium without active transport(74, 75).

Fluorescently-labeled dextrans are an attractive tool for studying the extent of endothelial sonoporation or BBB disruption following FUS with MBs. Larger dextrans require a greater peak FUS pressure in order to cross the BBB than smaller dextrans, suggesting that the degree of BBB disruption is correlated with the pulsing pressure(76, 77). The size of the vessel plays a role in the equation, as well. Smaller vessels, less than 25 microns in diameter, were more likely than larger vessels to be disrupted and leaky following FUS and MBs. These vessels, which correspond to capillaries and the smallest of arterioles and venules(78), were more likely to experience “fast leakage” (thought to be attributed to tight junction disruption and paracellular transport), compared to “slow leakage” (attributed to transcellular transport)(79). This is thought to be due to increased interactions between MBs and vessel walls in small vessels. As a 2 micron MB can expand up to 20 microns in a FUS field, the oscillating MB is likely to contact the vessel wall (and thus exert shear stress and microstreaming effects) more frequently in a smaller blood vessel(80).

2.4.3. Safety and Monitoring of FUS-Mediated MB Activation

While FUS in conjunction with MBs clearly holds immense promise for delivering therapeutics across the BBB, there are also a number of risks associated with the approach. In response to these risks, a number of safety mechanisms have been adopted.

MBs oscillate as they pass through the region where ultrasound has been focused. The applied amplitude of the FUS pressure dictates whether the MBs oscillate in a stable or inertial

manner. At lower pressures, MBs oscillate stably, with regular and reproducible expansion during rarefaction periods and shrinking during compression. Stable cavitation is more predictable, and thus, safer, for FUS-mediated BBB disruption. Safe and reproducible BBB opening in a stable cavitation regime is associated with transient tight junction disruption, vascular endothelial sonoporation, and enhanced transcytotic activity for a four-to-six hour period during which the BBB is permeabilized(72, 81, 82). In contrast, at higher acoustic pressures, MBs may undergo inertial cavitation. In this regime, the MBs demonstrate unstable oscillations, ultimately leading to rapid, violent bubble collapse which can produce elevated local temperatures, shock wave formation, and high pressure jet streams(83, 84). While inertial cavitation may prove useful in certain disease contexts, or for the delivery of very large payloads, it is typically avoided for most applications in healthy brain tissue.

It is well understood that driving MBs in the inertial cavitation regime can elicit neuroinflammation and petechiae(85), and is associated with tissue damage(86). However, a recent study has suggested that even low-pressure BBB disruption using FUS and MBs can induce a sterile inflammatory response in the brain parenchyma, as evidenced by the presence of damage-associated molecular patterns, activation of microglia and astrocytes, and tissue infiltration by $CD68^+$ macrophages (indicative of an innate immune response)(87). This finding was met with some resistance in the FUS community, which has for years touted the safety of the approach as a key selling point. Ensuing clarifying studies have indicated that the dose of MBs is an important variable to consider, as higher doses of MBs are associated with higher rates of edema and petechiae, and elevated expression of inflammatory genes. Animals treated with lower, clinically relevant doses of MBs did not display such responses, suggesting that the parameters of FUS-mediated BBB opening may be optimized to enhance drug and gene delivery without causing injury and inflammation(88). Another issue of concern within the field is variability in bioeffect response and treatment efficacy between different FUS-treated regions,

due in part to skull shape/thickness variability across and within animals. This variability is relevant to human clinical applications as well, and has motivated further study to better optimize BBB opening on a case-by-case basis.

In order to better address the risks raised by such preclinical studies, several groups have sought to develop systems for monitoring MB behavior within the brain, and to use these observations to inform treatments. These monitoring systems hinge on the principle of passive cavitation detection (PCD), which involves non-invasively recording the acoustic emissions generated by oscillating MBs within the skull upon exposure to FUS. These acoustic signatures correlate with the cavitation activity of the MBs, as well as the biological effects of the associated FUS exposures (89, 90). PCD can distinguish between stable and inertial cavitation signatures(91), and correlates well with the extent of BBB disruption(85, 92). MBs oscillating stably produce acoustic emissions at harmonic frequencies (integer multiples of the transducer driving frequency), subharmonic frequencies (half of the driving frequency), and ultraharmonic frequencies (midway between adjacent harmonics), while inertially collapsing MBs produce broadband acoustic signals(93). PCD is now often used to monitor FUS treatments and ensure safe experimental conditions in many pre-clinical studies. Previous work by the Hynynen group obviated adverse events by identifying the FUS pressure at which subharmonic signals begin to be detected, and then conducting all following sonications at a fixed percentage of this pressure. They identified that sonications conducted at 50% of the threshold pressure (where subharmonic activity was detected) resulted in safe BBB opening without gross tissue damage(94). Other groups have demonstrated safety control using the harmonic(95), ultraharmonic(96), or broadband signals(97) to inform and adjust treatments to maximize safety. Whatever the choice of frequency to monitor and cutoff to observe, intraoperative monitoring with PCD helps to reduce the chances of damage associated with FUS-mediated BBB opening.

2.5 Gene Delivery to the Brain with FUS

Many pathologies of the CNS are attractive targets for gene therapy. Extensive research has been conducted attempting to deliver genes to the brain for Alzheimer's(98), Parkinson's(99), glioma(100), ischemic stroke(101), and ALS(102). Gene therapy can provide either a transient or continuous effect depending on the vector delivered, and can be combined with cell-type-specific promoters or reporter genes to reduce off-target effects and improve treatment monitoring. However, gene therapy in the brain is limited by many of the same BBB features which inhibit drug delivery to the brain. For this reason, FUS-mediated BBB disruption has become an appealing method to facilitate delivery of gene products to the brain parenchyma. For the past decade, the field of FUS-mediated gene delivery to the brain has proliferated, with a wide variety of types of gene vectors explored.

2.5.1. Viral Vectors

Viral methods of gene delivery have the primary advantage of inducing lasting therapeutic effects. Viral vectors can permanently integrate the gene of choice into the host genome, allowing for continuous expression in that cell and all future progeny. While this may be an attractive feature for degenerative genetic conditions, there is considerable public and scientific hesitation surrounding the possible risk of mutation with chromosomal integration, which has somewhat limited this field of research. When viral delivery is utilized, the most popular vector for the gene of interest is adeno-associated virus (AAV). AAV is small, has a relatively high transduction efficiency, and has limited immunogenicity compared to other viral options. FUS and MBs have been used to deliver AAV vectors encoding reporter genes to a number of targets in the CNS, including the brain(103–106), retina(107), and spine(108). Use of a neuron-specific promoter enabled selective expression of the AAV-borne reporter gene by neurons(109). FUS in conjunction with AAV vectors has been used to deliver functional genes

as well, including glial derived neurotrophic factor (GDNF) to increase dopaminergic neuron activity in a mouse model of Parkinson's(110), light-sensitive Channelrhodopsin-2 (ChR2) to develop a tool for optogenetics(111), and shRNA plasmids targeted to α-synuclein to reduce α-synuclein levels in specific brain regions(112).

2.5.2. Liposomes

Liposomes are spherical vesicles with lipid shells, which can be used to encapsulate a wide variety of drug or gene payloads. They can provide the delivered materials with protection from proteases and nucleases while traversing the systemic vasculature, enhancing efficacy. FUS and MBs have been used to deliver liposomes loaded with a GDNF plasmid to the brain in mouse models of Parkinson's(113, 114) and Huntington's(115). Other studies have used FUS, MBs, and liposomes to deliver a variety of payloads to gliomas, including chemotherapeutic drugs to gliomas or shRNA targeting a regulator of apoptosis(116).

2.5.3. Naked Plasmid

Plasmid DNA is anionic (negatively-charged), and can be electrostatically bound to cationic (positively-charged) lipid-shelled MBs to create a compound agent. Such agents ensure that the plasmid DNA is available on site at the instant of FUS-mediated MB activation and BBB disruption, with the goal of increasing DNA extravasation and uptake. Studies in peripheral tissues demonstrate that the electrostatic coupling of plasmid DNA to MBs enhances transfection compared to freely circulating plasmid delivered concomitantly with FUS and MBs(117–119). In the brain, FUS has been used to activate DNA-bound MBs to deliver a range of plasmids, including genes for brain-derived neurotrophic factor (BDNF)(120), GDNF(121), GFP(122), and mCherry(123). While this approach provides less protection from nucleases than

liposomal or nanoparticle carriers, it also introduces fewer additional foreign materials into the bloodstream, and the brain.

2.5.4. Brain-Penetrating Nanoparticles

Polymer-based nanoparticles allow for the encapsulation of gene products with a high degree of customizability, can protect their payload against degradation or clearance, and may have improved loading capacity or drug-release profiles relative to other vectors. Previously, our group has helped to develop polymeric “brain-penetrating” nanoparticles (BPNs) to facilitate gene delivery(124–126). These BPNs feature a dense coat of polyethylene glycol, which enhances penetration into brain tissue relative to conventionally PEGylated nanoparticles. This enhanced vector distribution and transfection volume can be observed in both healthy brain(127) and brain tumor tissue(126). Further, the safety and efficacy of FUS-mediated BPN delivery has been demonstrated in normal brain tissue(124), and therapeutic efficacy has been demonstrated in a rat model of Parkinson’s using FUS and BPNs to deliver a GDNF transgene to restore dopaminergic neuron activity(125).

Chapter 3: Sonoselective Transfection of Cerebral Vasculature without Blood-Brain Barrier Disruption

Catherine M. Gorick, Alexander S. Mathew, William J. Garrison, E. Andrew Thim, Delaney G. Fisher, Caitleen A. Copeland, Ji Song, Alexander L. Klibanov, G. Wilson Miller, and Richard J. Price. *Proceedings of the National Academy of Sciences*, 2020, 117 (11): 5644-5654. DOI: 10.1073/pnas.1914595117

3.1 Abstract

Treatment of many pathologies of the brain could be improved markedly by the development of non-invasive therapeutic approaches that elicit robust, endothelial cell-selective, gene expression in specific brain regions that are targeted under MR image-guidance. While focused ultrasound (FUS) in conjunction with gas-filled microbubbles (MBs) has emerged as a non-invasive modality for MR image-guided gene delivery to the brain, it has been used exclusively to transiently disrupt the blood-brain barrier (BBB), which may induce a sterile inflammation response. Here, we introduce a new MR image-guided FUS method that elicits endothelial-selective transfection of the cerebral vasculature (i.e. “sonoselective” transfection), without opening the BBB. We first determined that activating circulating, cationic plasmid-bearing, MBs with pulsed low-pressure (0.1 MPa) 1.1 MHz FUS facilitates sonoselective gene delivery to the endothelium without MRI-detectable disruption of the BBB. The degree of endothelial selectivity varied inversely with the FUS pressure, with higher pressures (i.e. 0.3 MPa and 0.4 MPa FUS) consistently inducing BBB opening and extravascular transfection. Bulk RNA sequencing analyses revealed that the sonoselective low pressure regimen does not upregulate inflammatory or immune responses. Single cell RNA sequencing indicated that the transcriptome of sonoselectively transfected brain endothelium was unaffected by the treatment. The approach developed here permits targeted gene delivery to blood vessels and could be used to promote angiogenesis, release endothelial cell-secreted factors to stimulate nerve regrowth, or recruit neural stem cells.

3.2 Introduction

Pathologies of the brain, including neurodegenerative diseases, primary and metastatic brain tumors, cerebrovascular disease (stroke), and mental illnesses like depression and obsessive-compulsive disorder, are estimated to affect hundreds of millions of people worldwide(128–134). Gene therapy approaches for these diseases have shown promising preclinical results(135–140), but clinical treatment options for many of these conditions remain quite limited, due in large part to the difficulty of delivering therapeutics to the brain in a targeted manner. The blood-brain barrier (BBB), which includes a close network of tight junctions between endothelial cells to prevent paracellular diffusion, helps to isolate and protect the brain tissue from potentially harmful molecules in the systemic circulation, but also prevents the uptake of many therapeutics from the bloodstream(7, 14, 141, 142). Additionally, the skull presents a significant challenge for direct intracranial injections of therapeutics(27, 28), which are consequently very invasive and pose considerable surgical risks.

In light of these challenges to controlled delivery of therapeutics to the brain, focused ultrasound (FUS) has emerged as a promising approach to facilitate non-invasive, repeatable, and targeted drug and gene delivery to brain tissue across the BBB(46, 125, 143–145). Gas-filled microbubbles (MBs) can be introduced to the circulation intravenously. These MBs expand and contract in response to the acoustic pressure waves (which, at certain frequencies, can pass through bone without excessive attenuation(146)), pushing and pulling on endothelial cells to disrupt tight junctions and enhance transcellular transport(76, 81, 147, 148) and induce transport of different molecules across the BBB(74, 90, 149–153). This method of using FUS in conjunction with MBs to transiently open the BBB has been used to deliver a wide range of therapeutic agents, including antibodies(154–156), proteins(157, 158), nanoparticles(143, 145, 159), and even stem cells(160, 161), to specific sites within the brain. The FUS modality has led to major breakthroughs for gene therapy for central nervous system pathologies, as well(105,

109, 125, 162, 163). Therapeutic agents can be co-injected into the bloodstream along with MBs, or can be encapsulated within or linked to the MB shell to improve colocalization and enhance delivery(118, 164–168). Widespread BBB disruption has even been shown to promote a reduction in amyloid-beta plaques in a mouse model of Alzheimer's disease(169). The first clinical trials of FUS-mediated BBB disruption in human Alzheimer's disease and glioma patients were recently completed, with no overt adverse effects(170, 171). Without question, FUS-mediated BBB disruption has proved to be an extremely valuable tool for non-invasive therapy for a wide range of cerebral pathologies.

Recent studies have revealed that opening of the BBB by FUS and MBs can induce an acute sterile inflammatory response in brain tissue(172–174). The inflammation induced by FUS has been shown to promote a wide range of beneficial effects, including immune activation and recognition of CNS tumors(175, 176), stimulation of neurogenic pathways that could permit regenerative therapies(172, 177, 178), and improving uptake of therapeutics from the bloodstream by increasing endocytosis and reducing small molecule efflux(149, 179). However, disruption of the BBB may not be desirable in all cases where gene therapy has potential benefits. Following ischemic stroke, for example, the cerebral tissue is characterized by a high degree of instability and extensive acute and chronic inflammatory responses(180–183). In this scenario, further inflammation from BBB disruption, though transient and safe in many contexts, could pose a potential risk in the already-compromised microenvironment of the stroke ischemic penumbra. Other neurological conditions have also been associated with pathological inflammation(184), motivating the need for a gene therapy approach which avoids this potential FUS-induced sterile inflammatory response. Gene therapy targeted to endothelial cells could theoretically be utilized to permit modulation of the vasculature to promote angiogenesis, release endothelial cell-secreted factors to stimulate nerve regrowth, or recruit neural stem cells without affecting the BBB.

Endothelial cell sonoporation with FUS and MBs has been explored extensively *in vitro.* These studies have demonstrated the formation of membrane pores on endothelial cells following MB oscillation-induced shear stress as well as the initiation of intercellular gaps between adjacent cells and induction of endocytosis, all of which could facilitate the delivery of therapeutic agents(56, 74, 75, 185–190). The effects of acoustic sonoporation have been investigated *in vivo* as well(149, 150, 191), but to date no studies have utilized FUS to achieve targeted sonoporation of endothelial cells *in vivo* without disruption of tight junctions and/or enhancement of transcellular transport that would allow for therapeutic delivery beyond the vasculature.

In this study, we develop a method for endothelial-selective transfection of the cerebral vasculature without disruption of the BBB. We utilize low-pressure FUS to oscillate MBs such that we achieve endothelial cell membrane sonoporation without breaking tight junctions or enhancing transcellular transport and facilitating transport of the gene product beyond the blood vessels. This approach permits for spatially-targeted and cell-type-selective transfection in the brain without inducing inflammatory or immune responses.

3.3 Results

3.3.1 Peak-negative pressure of FUS pulsing can be modulated to yield sonoselective transfection cerebrovascular endothelium

To test the hypothesis that reduced FUS peak-negative pressure (PNP) results in increased endothelial selectivity of transfection, we performed FUS-mediated gene delivery across a range of PNPs. Briefly, mCherry plasmid was first conjugated to cationic MBs without affecting MB size or stability (Figure 3.S1). MB-plasmid conjugates were delivered intravenously and the right striatum was targeted with FUS at PNPs ranging from 0.1 to 0.4 MPa (measured in water by hydrophone). 24 hours later, the brains were harvested for staining to determine the overlap between mCherry expression and endothelial cells. The overlap between the endothelial markers (BS-I lectin or GLUT1) and mCherry expression was used to quantify the degrees of "endothelial-selective" transfection (mCherry signal that overlapped with one of the vascular markers) and "extravascular" transfection (mCherry signal which did not overlap with the vascular markers) (Figure 3.1A-B). In the area of the brain targeted with FUS, we observed robust mCherry expression in and around the vasculature, while in the contralateral region of the brain (FUS^-), little to no mCherry expression was detected (Figure 3.1, Figure 3.S2). The fraction of "endothelial-selective" transfection ranged from 85-93% at the 0.1 MPa PNP, and decreased with higher PNPs (Figure 3.1C). This trend was consistent when both BS-I lectin and GLUT1 were used as endothelial markers, as well as when FUS was targeted under MRI guidance or with a stereotactic frame independent of image guidance. We have termed this phenomenon "sonoselectivity" – the ability to selectively transfect particular cell types by altering the ultrasonic parameters.

3.3.2 Characterization of mCherry expression in FUS-transfected cerebral vasculature

After quantifying the endothelial selectivity of mCherry transgene delivery, we investigated additional metrics of mCherry transfection. In order to semi-quantitatively assess the extent of transfection within the vasculature, the mean grayscale value of the mCherry staining within mCherry-positive vessels was compared across PNPs. There was no significant difference in this metric across PNPs under any of the conditions tested - MRI guidance versus stereotactic guidance, and BS-I lectin versus GLUT1 staining for endothelium (Figure 3.1D). This indicates that there were no detectable changes in mCherry protein expression as a function of PNP. Additionally, there was no difference in the fraction of microvessels (as indicated by BS-I lectin or GLUT1 staining) positive for mCherry across PNPs (Figure 3.1E). This finding is important for potential therapeutic applications of the sonoselective approach, as it demonstrates that the area of transfection coverage is not sacrificed for increased endothelial selectivity. Further investigation of the brains treated at 0.1 MPa was conducted to identify what type of vessels were being transfected. After extensive confocal microscopic examination of tissue sections from the 0.1 MPa group, we determined that mCherry transfection was confined to capillaries, with little to no evidence of mCherry expression in arterioles and venules (Figure 3.S3). Finally, to assess whether transgene was expressed in off-target organs, we sonoselectively delivered a luciferase reporter plasmid with 0.1 MPa FUS to the cerebrovascular endothelium in a small cohort of mice (n=3). Bioluminescence measurements showed that luciferase was indeed robustly expressed in FUS-targeted brains, but undetectable in off-target organs (i.e. heart, lungs, liver, and kidney) (Figure 3.S4).

3.3.3 Sonoselective transfection of cerebrovascular endothelium is not accompanied by detectable blood-brain barrier opening

T1-weighted MR images were collected before and after FUS, using a 3D fast gradient echo pulse sequence, to guide FUS targeting (i.e. 4 spot sonication pattern in right striatum) and

visualize contrast agent extravasation into brain tissue due to BBB disruption (Figure 3.2A). At 0.1 MPa, there was no enhancement in signal intensity in the FUS-targeted regions, indicating a lack of BBB disruption. At increasing PNPs, we began to observe significant increases in the degree of signal enhancement and BBB opening (Figure 3.2B). These results demonstrate that the sonoselective endothelial transfection at 0.1 MPa can be achieved independent of detectable BBB disruption. To assess MB activation as a function of PNP, acoustic emissions were recorded and analyzed after each treatment. Acoustic emissions at the 2^{nd}, 3^{rd}, and 4^{th} harmonics increased significantly in concert with increasing PNP; however, no differences in broadband emissions were detected (Figure 3.2C). Within the "sonoselective" 0.1 MPa group, 2^{nd}, 3^{rd}, and 4^{th} harmonic emissions were remarkably consistent, showing little variability from treatment to treatment.

3.3.4 Sonoselective endothelial transfection is not associated with significant inflammatory or immune responses

To assess the impact of sonoselective transfection on brain tissue, we conducted a transcriptomic analysis of the FUS-treated brain tissue at 6 hours and 24 hours after FUS application. We investigated 3 PNP for this analysis: 0.1 MPa, where we never observe detectable BBB disruption, 0.2 MPa, where we often see very minor BBB disruption, and 0.4 MPa, where there is routinely robust opening of the BBB and extensive contrast agent extravasation into the brain (Figure 3.2). At either 6 or 24 hours following FUS activation of plasmid-bearing MBs, the front right quadrant of the brain was harvested and processed for bulk mRNA sequencing followed by bioinformatics analyses. At both timepoints, we observed hundreds of differentially expressed genes at the 0.4 MPa PNP relative to naïve control animals, and far fewer at 0.2 and 0.1 MPa (Figure 3.3A). We next investigated the differential regulation of key genes related to inflammatory and immune responses. Glial fibrillary acidic protein

(GFAP), a marker of astrogliosis, was upregulated at the 24 hour timepoint in the 0.4 MPa group, but no upregulation was observed in the 0.1 or 0.2 MPa groups (Figure 3.3B). This is consistent with a greater potential for astrogliosis at the higher FUS PNPs that elicit detectable BBB opening, but not at lower FUS PNPs. Ionized calcium binding adaptor molecule 1 (Iba1), a marker of microgliosis, was not differentially expressed at any PNPs or timepoints, although it appears to be trending higher in the 0.4 MPa group at 24 hours after FUS (Figure 3.3B). Examination of several cytokine transcripts commonly associated with immunosuppression showed that they were neither significantly upregulated nor downregulated at any of the tested PNPs (Table 3.S1). It should also be noted that some markers of inflammation, including NFκB pathway upregulation, are largely resolved by 24 hours, indicating that the sterile inflammation response is likely transient and reversible.

Gene set enrichment analysis of the bulk RNA seq data revealed significant enrichment of numerous pathways associated with sterile inflammatory responses at the 0.4 MPa PNP level, including the reactome adaptive and innate immune system pathways, the chemokine signaling pathway, and the NFκB pathway (Figure 3.3C). Importantly, none of these pathways were enriched at 0.1 or 0.2 MPa (Figure 3.3C). We then performed a leading-edge analysis of the chemokine signaling pathway gene set. Heat maps for the 5 most differentially expressed chemokines in this gene set at 6h and 24h for the 0.4 MPa group are shown in Figure 3.3D and compared to the lower PNP groups. Chemokine expression was clearly and consistently higher in the 0.4 MPa group, wherein BBB opening was always evident.

We next examined the bulk RNA seq data to ascertain whether, independent of FUS application, systemically circulating cationic MBs could affect the brain transcriptome. In comparison to naïve brain tissue, we observed only minimal changes in gene expression at both 6h and 24h after cationic MB injection without FUS (Figure 3.S5A). Furthermore, gene set enrichment analysis of the RNA seq data indicated that no pathways associated with

inflammation and/or immunological responses were significantly enriched or suppressed by cationic MBs alone (Figure 3.S5B).

3.3.5 Low-pressure FUS-mediated transfection is selective for endothelial cells

We then performed fluorescence activated cell sorting (FACS) and single cell RNA sequencing studies to both confirm that low PNP FUS markedly enriches the endothelial cell fraction of transfected cells and to determine whether sonoselective transfection alters the endothelial transcriptome. FACS was first used to isolate mRUBY$^+$ cells from brain tissue wherein mRUBY plasmid-bearing MBs were activated with FUS at 0.1, 0.2, and 0.4 MPa. Brain tissue from sham mice that received mRUBY plasmid-MB injection, but without FUS application, comprised a sham control and were used to generate the flow cytometry gating scheme (Figure 3.4A; left). The fraction of mRUBY$^+$ cells isolated from the total population increased with FUS PNP (Figure 3.4A), and the mean fluorescence intensity (MFI) of mRUBY was significantly enhanced at 0.4 MPa (Figure 3.4B). Single cell RNA sequencing was then performed on mRUBY$^+$ cell populations from 0.1, 0.2, and 0.4 MPa treated mice, as well as from sham mice (which received MBs but not FUS, and were not sorted for mRUBY$^+$). There were 2000 cells sequenced from each treatment group. T-distributed scholastic neighbor embedding (tSNE) followed by graph-based clustering was used to group transcriptomally similar cell populations (Figure 3.4C). Endothelial cell clusters were disaggregated based on treatment condition and reproduced in Figure 3.4D. The proportion of FUS-transfected cells that were endothelial was enhanced and inversely related to PNP when compared to the baseline proportion of endothelial cells in sham, non FUS-treated brains, confirming that the endothelial fraction of total transfected cells is enriched with low PNP FUS and diminished with high PNP FUS. At higher PNPs, the fraction of transfected cells which are endothelial is similar to the fraction of endothelial cells present in the brain at baseline, indicating no particular selectivity for endothelial cells. At lower PNPs, a greater fraction of the transfected cells was endothelial,

suggesting a greater degree of sonoselectivity at these PNPs. This result is quantified in Figure 3.4E, which illustrates that the relationship between FUS PNP and the enrichment of the endothelial fraction of transfected cells is independent of the expression marker (VE cadherin, Claudin 5, Flt-1, or VWF) used to identify any given cell as “endothelial”. This is consistent with the BSI-lectin and GLUT-1 immunohistochemistry results in Figure 3.1, which shows an increased proportion of endothelial cells transfected at lower PNPs.

Finally, we analyzed the transcriptomes of all mRUBY^{+} endothelial cells via single cell RNA sequencing and compared them to untreated brain endothelium. In general, the transfected endothelium was remarkably quiescent. In total, only 8 transcripts were differentially expressed amongst all 3 FUS PNPs (Figure 3.5A). Gene set enrichment analysis revealed that, for the 0.1 and 0.2 MPa groups, no gene sets were significantly enriched or repressed. For the 0.4 MPa group, MHC Class II Antigen Presentation was the only significantly enriched gene set (Figure 3.5B). The Toll Receptor Cascades and Adaptive Immune System gene sets were only significant at P=0.13, while the Innate Immune System gene set was only significant at P=0.19 (Figure 3.5B). Running enrichment score and leading edge analyses for the MHC Class II Antigen Presentation gene set at 0.4 MPa are shown in Figures 3.5C and 3.5D, respectively. In the leading edge analysis, each column corresponds to an individual endothelial cell. Enrichment of the MHC Class II Antigen Presentation gene set was driven by Ctsd, Lgmn, and Ctsb, which clearly exhibit enhanced expression at 0.4 MPa when compared to the other 3 groups. Due to the prohibitively high cost of single cell RNA sequencing, Figure 3.4 and Figure 3.5 represent the findings from a single trial in which 3 brains from each treatment conditions were pooled for each sample.

3.4 Discussion

Clinical outcomes for many brain pathologies could benefit appreciably by the introduction of new MR image-guided and non-invasive gene therapies that specifically modulate the function of the endothelial cell component of the blood brain barrier. In recent years, MB activation with FUS has been advanced as a mechanism for targeted gene delivery to the brain, albeit exclusively as a tool to disrupt the BBB and facilitate the transfection of brain cells that physically reside beyond the cerebral vasculature (e.g. neurons, astrocytes, and microglia). Here, we demonstrate, for the first time, that FUS PNP can be modulated to achieve so-called “sonoselective” (i.e. ~90% cell specificity) endothelial transfection without the use of a cell-specific promoter. Of note, FUS application in this regime was accompanied by clearly demarcated and remarkably consistent acoustic harmonic emissions signatures that we propose could be exploited to eventually control sonoselective endothelial treatments in future applications. Bulk RNA sequencing confirmed that sonoselective endothelial transfection was achieved without eliciting a sterile inflammation response, while single cell RNA sequencing indicated that the transcriptome of sonoselectively transfected endothelium was unaffected by treatment. Because BBB integrity is preserved, this non-invasive platform approach for cerebrovascular endothelial gene therapy may be especially powerful for conditions wherein even transient BBB disruption might pose a significant risk.

3.4.1 Sonoselective Transfection of Endothelium without Use of Endothelial-Specific Promoters

The sonoselective transfection regime demonstrated here facilitates increased transfection of endothelial cells at low FUS PNPs. This finding is evidenced by both the increased overlap between a fluorescent transgene and markers of endothelium in immunofluorescent staining, as well as the increased population of endothelial cells amongst

the transgene-positive population identified using FACS and single cell RNA sequencing. Importantly, this selective transfection is achieved without the use of a cell-type-specific promoter. For endothelium, this aspect is especially significant as endothelial cell-specific promoters can yield weak and variable transgene expression across different tissue beds, and particularly in the brain(192–195). The ability to target transfection to the endothelium without a cell-specific promoter allows for greater flexibility in gene therapy design. We can take advantage of the increased persistence or magnitude of transfection provided by some constitutive promoters to achieve a larger effect in the targeted cells for the same plasmid dose, opening the door to many future applications for non-invasive alterations of regions of the cerebral vasculature.

In this study, we made use of the constitutively-active CMV promoter, which has a relatively short “lifespan”, with expression peaking at 24-48 hours before diminishing. We envision this sonoselective approach as a short-term therapy to initiate recovery after injury or disease; however, the system could also be adapted to utilize a viral delivery vector for permanent transgene expression. Alternatively, a longer-acting promoter could be used in conjunction with the nonviral system to permit extended but transient gene expression. Prior study by our group has demonstrated that FUS-mediated transfection of the brain with a nonviral vector driven by the beta-actin promoter results in sustained gene expression for 4+ weeks(145).

3.4.2 In vivo Endothelial Cell Sonoporation without Tight Junction Disruption or Transcellular Transport

There are many mechanisms by which FUS and MBs stimulate cellular uptake of therapeutic agents(149, 196). The oscillation of MBs close to the plasma membrane of cells has been shown to push and pull on the membrane to cause membrane deformation and pore

formation(197). The efficacy of membrane permeabilization has been shown to positively correlate with the oscillation amplitude of the MBs, as well(186). Stable oscillation of the MBs results in local steady fluid flow around the bubbles, which is known as microstreaming. This microstreaming places shear stress on nearby cell membranes. This shear stress varies with the acoustic pressure driving the MB oscillation(198), and even MBs activated at low acoustic pressures (0.2 MPa) can generate enough stress to potentially damage vascular endothelium(199). We hypothesize that these physical mechanisms of membrane disruption are taking place across the range of FUS PNPs tested here (0.1 to 0.4 MPa). While previous studies have demonstrated that FUS and MBs can result in the disruption of endothelial tight junctions(147, 200) , as well as increased transcellular uptake via vesicular transport(73, 201), these effects appear to be minimal with our 0.1 MPa treatment. We do not observe any contrast agent enhancement on T1-weighted MRI after 0.1 MPa FUS and MBs, and the transgene expression at this PNP is nearly all confined to the endothelium, suggesting that at this low PNP, the microbubble oscillation is sufficient to sonoporate the endothelial cell membranes but not sufficient to disrupt tight junctions or promote additional transcellular transport.

3.4.3 Harmonic Emissions Can Be Used to Monitor and Control Microbubble Activity and Associated Bioeffects

As the field of FUS-mediated therapeutic delivery to the brain gains momentum and moves closer to regulatory approval in human patients, there remains an ongoing concern over the potential dangers of neuroinflammation and petechiae due to damage caused by oscillating microbubbles. Additionally, variability in skull shape and thickness can result in variability in the bioeffects and treatment efficacy of FUS with MBs across and within test subjects(202–204). The concern over inflammation and treatment variability led to the development of monitoring systems to assess MB activity within the brain, and to use these observations to inform

treatments. These systems utilize the principle of passive cavitation detection (PCD). PCD involves recording the acoustic emissions produced by the oscillating MBs within the skull. These emissions can then be correlated with the biological effects of different FUS exposures, and used to monitor and control treatments to avoid unwanted adverse events(85, 90, 205, 206). There have been many recent advancements in cavitation monitoring to facilitate features like real-time control and feedback systems and enhanced three-dimensional cavitation cloud mapping(207, 208), all with the intention of developing increasingly sensitive methods to ensure the safety of MB activity within the brain. In this study, we utilized PCD during FUS treatments and found that harmonic emissions increased significantly with increased FUS PNPs, with little to no broadband noise being detected (indicating that these treatments are occurring below the inertial cavitation threshold of the MBs). The large difference in harmonic emissions between 0.1 and 0.2 MPa, as well as the low degree of variability across animals at 0.1 MPa, suggests that emissions within this “sonoselective” regime are distinct and reproducible. This is ideal for ease of recognizing the “sonoselective” signature in future treatments and controlling FUS PNP to maintain bioeffects in this regime. Such control will be key for the long-term clinical applicability of FUS-activated MB technology in the brain.

3.4.4 Sonoselective FUS Regime Does Not Induce a Sterile Inflammatory Response

The finding that BBB opening by FUS and MBs can stimulate an acute sterile inflammatory response(172–174) has raised some concerns over the use of FUS and MBs for noninvasive therapeutic delivery in the brain in specific disease contexts. While the induction of a temporary inflammatory response can be justified for many disease applications, there are some contexts in which even a transient effect of this kind could induce more damage than the therapeutic delivery can justify. We wanted to design a treatment approach that could be used for these especially sensitive disease microenvironments, where any additional inflammation

could have serious consequences. FUS activation of MBs at PNPs resulting in sonoselective endothelial transfection did not show any enrichment of genes or pathways related to adaptive or innate immune responses, nor inflammatory signaling, demonstrating the potential of this approach for safe, noninvasive, targeted gene transfection in the cerebral vasculature in settings where BBB opening poses excessive risks.

3.4.5 Sonoporation with Low-Pressure FUS Does Not Significantly Alter the Endothelial Cell Transcriptome

In addition to avoiding systemic inflammation and immune activation, we wanted to ensure that our transfection approach would not cause significant damage to the transfected endothelium. After identifying the endothelial cell population from the transfected cells using scRNAseq, we looked at the differentially regulated transcripts across the different FUS PNPs. Only a small number of individual genes were differentially regulated, at any of the FUS PNPs. The only gene set that displayed a significant difference was the MHC Class II Antigen Presentation gene set, which was upregulated at 0.4 MPa, but not 0.2 or 0.1 MPa. A few other gene sets related to inflammation and immune response approached significant upregulation at 0.4 MPa, but at 0.1 MPa, the endothelium remained remarkably quiescent. This finding is promising for potential applications of this approach in pathologies which affect the cerebral vasculature. However, while the endothelium appears quiescent at 24 hours after FUS, an important area for future investigation would be to assess the transcriptome at more acute time points. This would allow us to determine whether there is a transient response by endothelial cells which resolves by one day after treatment, or if the transfection does not in fact induce significant changes in gene regulation at any point.

3.4.6 Potential Clinical Implications

Given our results, low-PNP FUS with MBs could represent a therapeutic strategy for gene delivery to the cerebral vasculature for the treatment of a number of pathologies of the brain. By taking advantage of the phenomenon demonstrated here that endothelial membrane sonoporation is possible without extensive enhancement of transcellular transport and disruption of tight junctions (and thus, the BBB), we can deliver therapeutic genes to the vasculature even in sensitive disease settings. We envision using this platform to deliver pro-angiogenic and pro-arteriogenic genes to the vasculature in the context of ischemic stroke, as well as genes to stimulate the recruitment and differentiation of neural stem cells. Another application would be to transfect the endothelium with a gene for a transporter of some kind, which could then be used to alter the local concentration of a particular molecule in a specific region of the brain without actually opening the BBB. The recent clinical trials utilizing FUS and MBs to open the BBB in Alzheimer's or glioma patients(170, 171) provide hope that other therapeutic applications of FUS and MBs, such as this one, could be introduced to the clinic in the near future. While these trials involve intentional disruption of the BBB and would thus permit large molecule drug delivery, which our current approach does not, we hope that the sonoselective method detailed here could be used as an alternative therapy in the specific contexts where BBB opening may be contraindicated.

3.5 Materials and Methods

3.5.1 Animals

Male C57BL/6 mice were purchased from Charles River and maintained on a 12/12 hour light/dark cycle. Mice used in the experiments weighed between 22 and 28 g and were given food and water *ad libitum*. All animal experiments were approved by the Animal Care and Use Committee at the University of Virginia and conformed to the National Institutes of Health regulations for the use of animals in research.

3.5.2 Cationic Lipid-Shelled Microbubble Fabrication

To synthesize the cationic lipid-shelled MBs, we made a mixure of 2 mg/ml 1,2-distearoyl-sn-glycero-3-phosphocholine (DSPC; Avanti Polar Lipids, Alabastar, Alabama), 2 mg/ml polyethylene glycol 6000 monostearate (PEG 6000 MS; Stepan Kessco, Northfield, Illinois), and 0.8 mg/ml 1,2-distearoyl-3-trimethylammonium-propane (DSTAP; Avanti Polar Lipids, Alabastar, Alabama) in 0.9% NaCl (Baxter, Deerfield, Illinois). The mixture was filtered through a 0.2 um Nylon sterile filter, sparged with decafluorobutane gas (F2 Chemicals Ltd; Preston, United Kingdom), and then sonicated at the highest power (20 kHz, 30 s) with an ultrasound disintegrator (XL2020; Misonix, Farmingdale, New York) to generate the MBs. MBs were aliquoted into 13 mm glass vials, which were stoppered for storage after filling the headspace with decafluorobutane gas. The MBs were cleaned by flotation centrifugation before each experiment to remove residual micelles. An aliquot of the MB solution was centrifuged at 1000 rpm for 10 minutes, and the infranatant was removed and the bubbles resuspended in degassed saline. This process was repeated three times before the final resuspension of the bubbles at a concentration between 1.5 and $2*10^9$ MBs/ml. MBs were sized and counted using a Coulter counter (Multisizer 3; Beckman Coulter, Fullerton, California).

3.5.3 Plasmid Preparation and Conjugation to Microbubbles

The mCherry2-C1 and mRuby2-N1 plasmids were a gift from Michael Davidson (Addgene plasmids #54563 and #54614; http://n2t.net/addgene:54563 and http://n2t.net/addgene:54614; RRID:Addgene_54563 and RRID:Addgene_54614). The luciferase plasmid was a gift from William Kaelin (Addgene plasmid #18964; http://n2t.net/addgene:18964). The plasmids feature either an mCherry2, mRuby2, or luciferase gene under the control of a CMV enhancer and promoter for constitutive expression. Our studies demonstrate that peak expression is achieved by these plasmids by 24 hours after transfection and is maintained for about 1 day before beginning to decline. The plasmids were provided from Addgene (Watertown, Massachusetts) in the form of agar stabs of DH5α *E. coli* transformed with the plasmids. The bacteria were expanded in LB media (Sigma-Aldrich, St. Louis, Missouri) containing kanamycin (Sigma-Aldrich), and then the plasmids were collected and purified using an Endo-Free Maxiprep Kit (Qiagen, Germantown, Maryland). Plasmid was resuspended in Tris-EDTA buffer at a concentration between 400 and 500 ng/ul and stored at -20 degrees Celsius. Plasmid concentration was determined using a NanoDrop ND-1000 spectrophotometer (NanoDrop Technologies, Wilmington, Delaware).

On the morning of experiments, the appropriate purified plasmid was thawed and added to the cleaned MB solution at a ratio of 1.5 ug plasmid per 10^7 microbubbles. This ratio is consistent with prior studies of DNA binding to cationic MBs(209, 210). This mixture was allowed to incubate at room temperature for 10 min to permit the electrostatic coupling of the positively-charged bubbles and negatively-charged DNA, and was then stored on ice until use. Roughly 20-25% of the plasmid added to the MBs bound, for a total of 0.03 to 0.035 pg per MB. We did not observe significant changes to the size distributions of the MBs after conjugation to plasmid (Figure 3.S1).

3.5.4 MRI-Guided FUS-Mediated Plasmid Delivery

Male C57BL/6 mice were anesthetized with an intraperitoneal injection of 120 mg/kg ketamine, 12 mg/kg xylazine, and 0.08 mg/kg atropine in sterilized 0.9% saline. A tail vein catheter was inserted to permit intravenous injections of MBs, plasmid, and the MRI contrast agent. The heads of the mice were shaved and depilated, and the animals were then placed in a supine position over a degassed water bath coupled to an MR-compatible small animal FUS system (RK-100; FUS Instruments, Toronto, Canada). The entire system was then placed in a 3T MR scanner (Magnetom Trio; Siemens Medical Solutions, Malvern, Pennsylvania). A 2-inch cylindrical transmit-receive RF coil, designed and built in-house, was placed around the mouse's head to maximize imaging SNR. Baseline T1-weighted MR images were acquired and used to select 4 FUS target locations in and around the right striatum.

Mice received an injection of the conjugated MBs and mCherry (for fluorescence microscopy and bulk RNAseq assays), mRuby (for FACS sorting and scRNAseq assays), or luciferase (for assessing off-target transfection) plasmid (2×10^5 MBs/g body weight), followed by injection of additional free plasmid to reach a total plasmid dose of 40 ug, followed by 0.1 mL of 2% heparinized saline to clear the catheter. The total plasmid dosage of 40 ug is consistent with prior studies of cationic MB-mediated gene delivery(209, 211, 212). However, since we utilize a bolus injection of MBs here (as opposed to a slow infusion), we reduced the dosage of MBs to 2×10^5, which only allowed for a fraction of the plasmid to be delivered in MB-bound form. Thus, the injection of free plasmid immediately following the MBs was used to achieve the remainder of the 40 ug dose.

Sonication began immediately after clearance of the catheter. Sonications were performed at 0.1, 0.2, 0.3, or 0.4 MPa PNP using a 1.1 MHz single element focused transducer (FUS Instruments, Toronto, Canada) operating in 10 ms bursts, 0.5 Hz pulse repetition

frequency and 2 minutes total duration. These PNPs are free-field, nonderated measurements with a hydrophone in a water tank at a target distance equivalent to the treatment distance. Immediately following the FUS treatment, mice received an intravenous injection of Gd-DPTA contrast agent (0.5 ul/g body weight; Magnevist; Bayer Health Care, Indianola, Pennsylvania), and T1-weighted contrast-enhanced images were acquired to assess BBB opening. Animals were removed from the MRI and placed on a warm pad for 30 minutes prior to reversal of the anesthetic with antisedan (1 mg/ml). Passive cavitation analysis was performed.

3.5.5 Passive Cavitation Detection

Acoustic emissions were detected with a 2.5 mm wideband unfocused hydrophone mounted in the center of the transducer. Acoustic signal was captured using a scope card (ATS460, Alazar, Pointe-Claire, Canada) and processed using an in-house built MATLAB algorithm. Acoustic emissions at the fundamental frequency, harmonics (2f, 3f, 4f), sub harmonic (0.5f), and ultra-harmonics (1.5f, 2.5f, 3.5f) were assessed by first taking the root mean square of the peak spectral amplitude (V_{rms}) in each frequency band after applying a 200 Hz bandwidth filter, and then summing the product of V_{rms} and individual sonication duration over the entire treatment period. Broadband emissions were assessed by summing the product of V_{rms} and individual sonication duration for all remaining emissions over the entire treatment period.

3.5.6 Stereotactic FUS-Mediated Plasmid Delivery

Sonications using the stereotactic frame were performed using a 1 MHz spherical-face single element FUS transducer with a diameter of 4.5 cm (Olympus; Center Valley, New Jersey). FUS (0.1, 0.2, 0.3, or 0.4 MPa; 120 seconds, 10 ms bursts, 0.5 Hz burst rate) was

targeted to the right striatum. The 6-dB acoustic beamwidth along the axial and transverse directions are 15 mm and 4 mm, respectively. The waveform pulsing was driven by a waveform generator (AFG310; Tektronix, Bracknell, United Kingdom) and amplified using a 55 dB RF power amplifier (ENI 3100LA; Electronic Navigation Industries, Richardson, Texas).

Male C57BL/6 mice were anesthetized with an intraperitoneal injection of 120 mg/kg ketamine, 12 mg/kg xylazine, and 0.08 mg/kg atropine in sterilized 0.9% saline. A tail vein catheter was inserted to permit intravenous injections of MBs and plasmid. The heads of the mice were shaved and depilated, and the animals were then positioned prone in a stereotactic frame (Stoelting, Wood Dale, Illinois). The mouse heads were ultrasonically coupled to the FUS transducer with ultrasound gel and degassed water, and positioned such that the ultrasound focus was localized to the right striatum. Mice received an intravenous injection of the conjugated MBs and mCherry plasmid (2×10^5 MBs/g body weight), followed by injection of additional free plasmid to reach a total plasmid dose of 40 ug, followed by 0.1 mL of 2% heparinized saline to clear the catheter. Sonication began immediately after clearance of the catheter. In contrast to the MR-guided experiments, which targeted 3 or 4 spots, only one location was targeted in these studies due to the increased focal region of the transducer (4 mm in the transverse direction, relative to 1 mm for the transducer in the MR-compatible system).

3.5.7 Histological Processing

Immediately following euthanasia via an overdose of pentobarbital sodium and phenytoin sodium, animals were perfused via the carotid arteries with 10 ml of 2% heparinized 0.9% saline followed by 5 ml of 4% paraformaldehyde. The brains were suffusion-fixed in 4% paraformaldehyde for 24 hours at 4 degrees Celsius, followed by desiccation in 30% sucrose for 24 hours at 4 degrees Celsius. The desiccated brains were then equilibrated in OCT compound for 1 hour prior to flash freezing and storage at -80 degrees Celsius. The brains were then

mounted with OCT and sectioned using a cryostat (Leica, Buffalo Grove, Illinois) into 5 um thick sections.

3.5.8 Immunofluorescence – GLUT1 Staining of Endothelium

To assess endothelial selectivity of transfection using GLUT1 as an endothelial marker, mounted sections were washed 3× for 10 min in PBS with 0.1% Tween 20 and incubated with blocking solution (1% normal goat serum, 2% bovine serum albumin in 0.1% Tween 20 in PBS) for one hour. Sections were next incubated overnight with rabbit anti-mCherry (1:400; Abcam, Cambridge, Massachusetts) and mouse anti-GLUT1 (1:200; Abcam). After washing 3× for 10 min in PBS with 0.1% Tween 20, sections were incubated for 1.25 hours at room temp with Alexa Fluor 555-conjugated goat anti-rabbit IgG (1:500; Thermo Scientific, Waltham, Massachusetts), Alexa Fluor 488-conjugated goat anti-mouse IgG (1:200; Thermo Scientific), and Draq5 (1:1000; Thermo Scientific). After washing 3× for 10 min in PBS, sections were mounted using Prolong Diamond (Thermo Scientific).

Sections were imaged on a Nikon Eclipse TE2000 confocal microscope equipped with a 20× oil objective. Endothelial selectivity was assessed using ImageJ by manually comparing co-localization of mCherry expression with GLUT1 expression. At least three representative fields of view were counted from the FUS-treated region of the brain, as well as three fields of view from the contralateral side of the brain.

3.5.9 Fluorescent Histochemistry – BS-I Lectin Staining of Endothelium

To assess endothelial selectivity of transfection using BS-I lectin as an endothelial marker, mounted sections were washed 3× for 10 min in PBS with 0.1% Tween 20 and incubated with blocking solution (1% normal goat serum, 2% bovine serum albumin in 0.1%

Tween 20 in PBS). Sections were next incubated overnight with rabbit anti-mCherry (1:400; Abcam). After washing 3× for 10 min in PBS with 0.1% Tween 20, sections were incubated for 1 hr at room temp with Alexa Fluor 555-conjugated goat anti-rabbit IgG (1:500; Thermo Scientific), Alexa Fluor 488-conjugated BS-I lectin (1:300; Thermo Scientific), and Draq5 (1:1000; Thermo Scientific). After washing 3× for 10 min in PBS, sections were mounted using Prolong Diamond (Thermo Scientific).

Sections were imaged on a Nikon Eclipse TE2000 confocal microscope equipped with a 20× oil objective. Endothelial selectivity was assessed using ImageJ by manually comparing co-localization of mCherry expression with GLUT1 expression. At least three representative fields of view were counted from the FUS-treated region of the brain, as well as three fields of view from the contralateral side of the brain.

3.5.10 Bioluminescence Measurements

To assess biodistribution of the transgene and off-target transfection, mice received MBs conjugated to a luciferase plasmid and were treated with FUS in the right hemisphere of the brain. One day later, the mice were sacrificed and their organs (brain, lungs, heart, kidneys, and liver) were harvested and placed in a solution of D-Luciferin (150 ug/ml; Gold Biotechnology, St. Louis, MO) in PBS for 5 minutes. The organs were then imaged using an IVIS100 imaging system (Xenogen, Alameda, CA). Photons were collected and integrated for a period of 1 minute. Images were then processed using Xenogen's Living Image software.

3.5.11 Bulk RNA Sequencing and Analysis

Immediately following euthanasia, the mouse brains were harvested and the front right quadrants (FUS-treated region) were excised, placed in RNAlater (Qiagen), and stored at -80 °C. RNA extraction was performed using the RNeasy Mini Kit (Qiagen). mRNA was isolated

using the NEBNext Poly(A) mRNA Magnetic Isolation Module (New England Biolabs, Ipswich, Massachusetts) followed by library preparation using the NEBNext Ultra II Directional RNA Library Prep Kit for Illumina (New England Biolabs). Sequencing was performed using a NextSeq 500 (Illumina, San Diego, California) at a target depth of 25 million 2 x 75 bp paired end reads per sample. Reads were quasi-mapped to the mouse genome (mm10 assembly) and quantified at the transcript level using Salmon v0.11.2(213) followed by summary to the gene level using tximport v1.10.1(214). Differential gene expression was performed with DESeq2 v1.22.2(215). Gene set enrichment analysis was performed with the MSigDB canonical pathways gene sets(216) using FGSEA v1.8.0(217) run with 10,000 permutations.

3.5.12 Fluorescence Activated Cell Sorting (FACS)

Immediately following euthanasia, the mouse brains treated with 0 MPa, 0.1 MPa, 0.2 MPa, or 0.4 MPa (n = 3 per group) were harvested. The front right quadrants of each brain were excised and made into single cell suspensions using the Adult Brain Dissociation Kit (Miltenyi Biotec, Bergisch Gladbach, Germany). Suspensions were pooled by treatment group and incubated briefly with SYTOX Green Nucleic Acid Stain (1:500,000; Thermo Scientific) to identify live and dead cells. mRuby$^+$ cells were isolated from 0.1 MPa, 0.2 MPa, and 0.4 MPa cell suspensions using a BD Influx Cell Sorter (BD Biosciences, San Jose, California) with the 100 µm nozzle at 20 psi. The sort gate was established using the 0 MPa cells as a reference. Live singlet mRuby$^+$ cells were collected for single cell RNA-sequencing. FACS data were analyzed using FCS Express 6 software.

3.5.13 Single Cell RNA Sequencing and Analysis

After FACS, 0 MPa (unsorted), 0.1 MPa (mRuby$^+$), 0.2 MPa (mRuby$^+$), and 0.4 MPa (mRuby$^+$) single cell libraries were generated using the Chromium Controller (10X Genomics,

Pleasanton, CA) with the Chromium Single Cell 3' GEM, Library & Gel Bead Kit v3 (10X Genomics) and Chromium Single Cell B Chip Kit (10X Genomics). An average of 1531 cells per condition were sequenced on a NextSeq 500 (Illumina) at an average depth of 87,184 reads per cell. The CellRanger v3.0.2 pipeline was implemented to first convert bcl2 reads to FASTQ files followed by alignment to the mm10 (Ensembl 84) mouse reference genome and filtering. All further single cell analysis was performed in R using Seurat v3.0.2(218) with default parameters unless otherwise specified. Cell clusters were computed by graph-based clustering and subsequently identified by comparing the top 20 globally distinguishing markers with those having high cell-type specificity scores in the PanglaoDB webserver(219). Differential gene expression between endothelial subsets was performed using the MAST framework(220). Gene set enrichment analysis was performed with the MSigDB canonical pathways gene sets(216) using FGSEA v1.8.0(217) run with 100,000 permutations and sign(log2 fold change)*-log10(adjusted p value) as the ranking metric.

3.5.14 Statistical Analysis

All results are reported as mean±SEM. “n” values per group are evident in all figures as all individual data points are shown. Details of statistical testing are provided in the figure legends (GraphPad Prism 7). Significance was assessed at $p < 0.05$.

3.6 Chapter 3 Figures

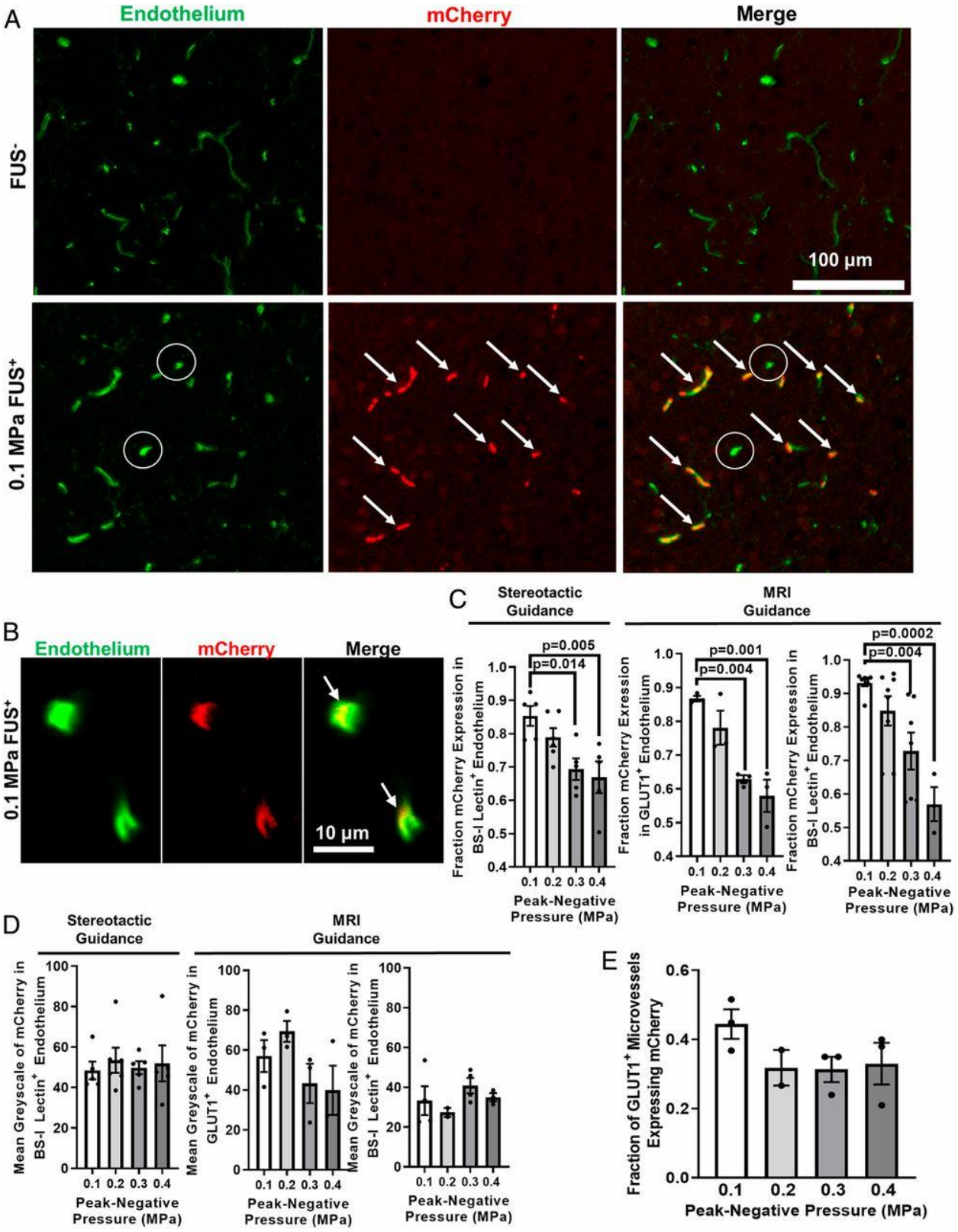

Figure 3.1. Focused ultrasound peak-negative acoustic pressure (PNP) may be tuned to yield sonoselective cerebrovascular endothelial transfection. A,B) Confocal images of FUS+ (0.1 MPa) and contralateral FUS- brain tissue showing expression of mCherry reporter gene (red) with respect to endothelial cells (BS-I lectin, green). Arrows denote mCherry colocalization with endothelium. Circles denote untransfected capillaries. C) Bar graphs of fraction of mCherry expression in cerebrovascular endothelium as a function of PNP. Highly selective endothelial transfection is observed at low PNPs (i.e., 0.1 MPa and 0.2 MPa). Similar relationships were observed when using both stereotactic and MR image guidance and both GLUT1 and BS-I lectin as endothelial markers. One-way ANOVAs followed by Dunnett's multiple comparison tests. D) Bar graphs of mean grayscale intensity of mCherry transgene expression in endothelium. Increasing PNP did not enhance endothelial mCherry fluorescence intensity. One-way ANOVAs followed by Dunnett's multiple comparison tests. E) Bar graph of fraction of GLUT1+ microvessels expressing mCherry. Increasing PNP did not increase the fraction of transfected microvessels. One-way ANOVA followed by Dunnett's multiple comparison tests.

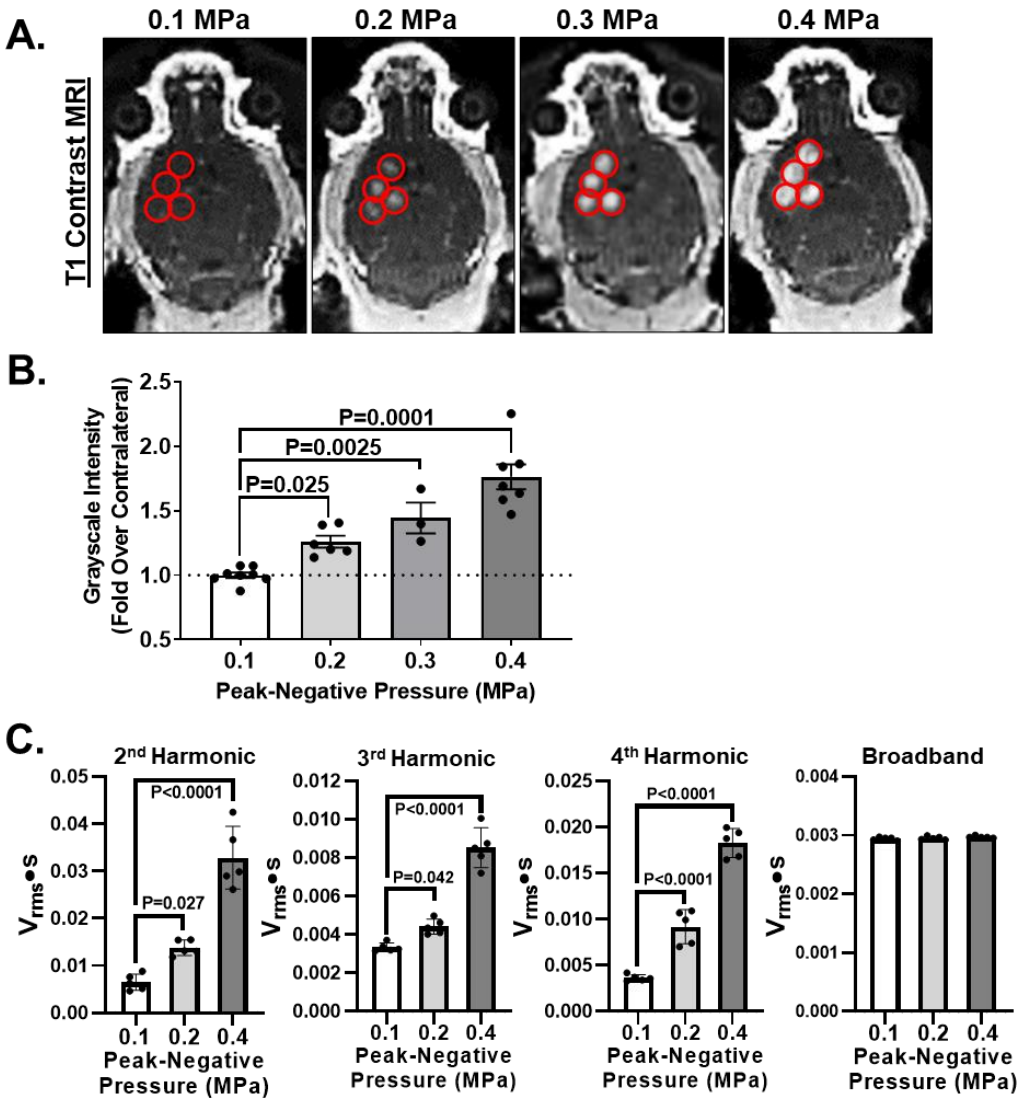

Figure 3.2. Sonoselective transfection of cerebrovascular endothelium is achieved without detectable BBB opening. A) T1 contrast MR images of mouse brains after application of pulsed FUS in the presence of systemically administered MBs. FUS was applied at peak-negative PNPs ranging from 0.1 to 0.4 MPa in a 4-spot sonication pattern. Sonication sites are denoted with red circles. Contrast is not detectable in FUS^+ sites at 0.1 MPa, but becomes visible at higher PNPs, indicating blood-brain barrier opening. B) Bar graph of contrast enhancement over contralateral FUS^- control hemisphere as a function of PNP. One-way ANOVA followed by Dunnett's multiple comparison tests. **C**) Passive cavitation analyses for 2^{nd}, 3^{rd}, and 4^{th} harmonics, as well as broadband emissions. One-way ANOVAs followed by Dunnett's multiple comparison tests.

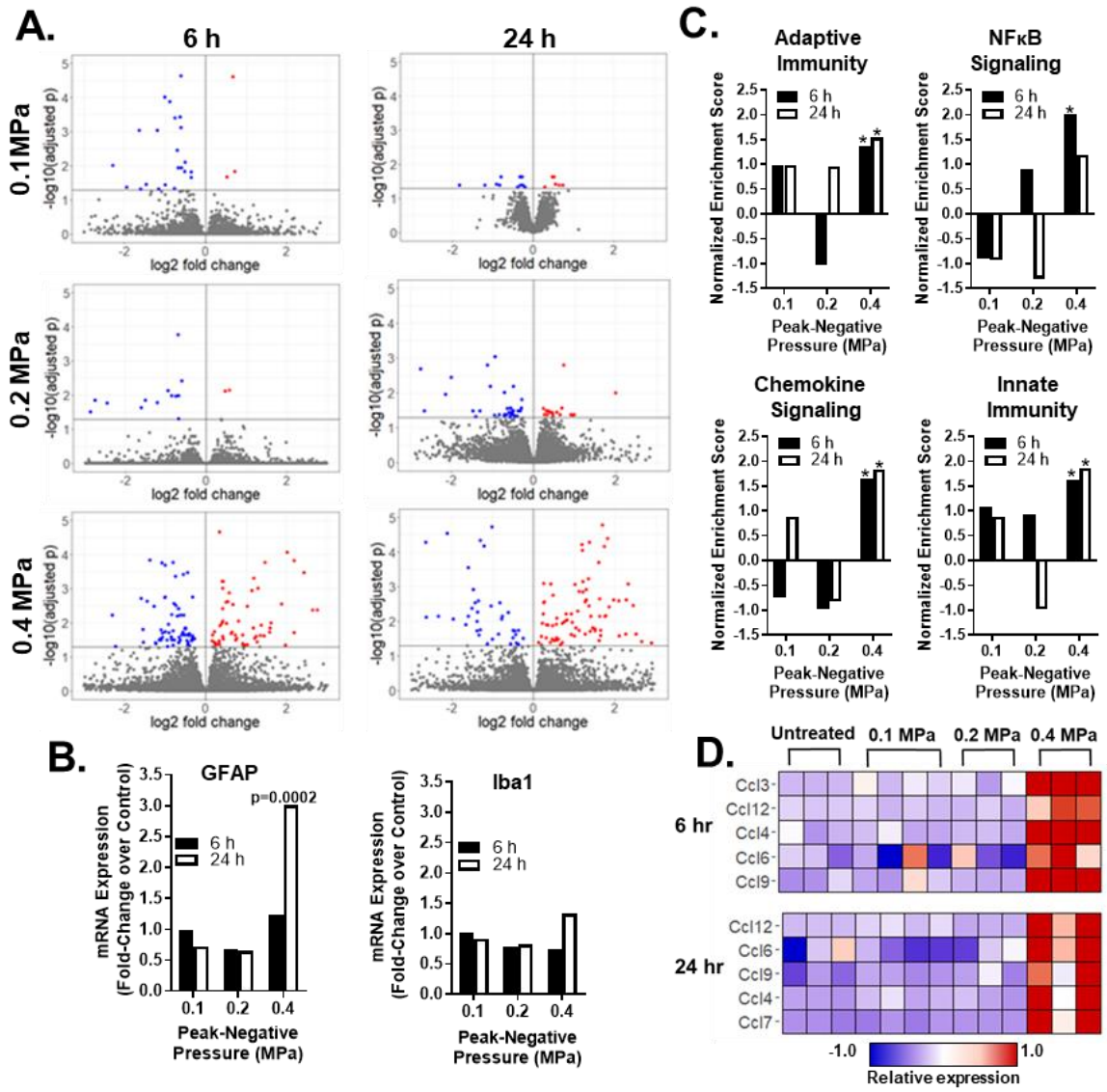

Figure 3.3. Sonoselective transfection of cerebrovascular endothelium at low peak-negative pressure is achieved without eliciting a sterile inflammation response. A) Volcano plots of differentially regulated transcripts at 6 and 24h after pulsed FUS application to the brain [0.1 MPa (blue), 0.2 MPa (green), and 0.4 MPa (red)] in the presence of systemically administered microbubbles. Note the increase in differentially regulated transcripts with increasing PNP. B) Bar graphs of transcripts used to assess astrogliosis (GFAP) and microgliosis (Iba1). Expression is shown as a fold-change over normal brain tissue. No changes were observed in Iba1 expression, while GFAP expression was only increased at 24h in response to 0.4 MPa FUS. C) Gene set enrichment analyses for selected pathways associated with inflammation and immunity. All pathways were significantly enriched at 0.4 MPa; however, none were enriched at 0.1 MPa or 0.2 MPa. *P<0.05 vs. untreated brain tissue. D) Expression levels of selected chemokines identified via leading edge analysis of the “Chemokine Signaling” pathway. Each column corresponds to a single mouse.

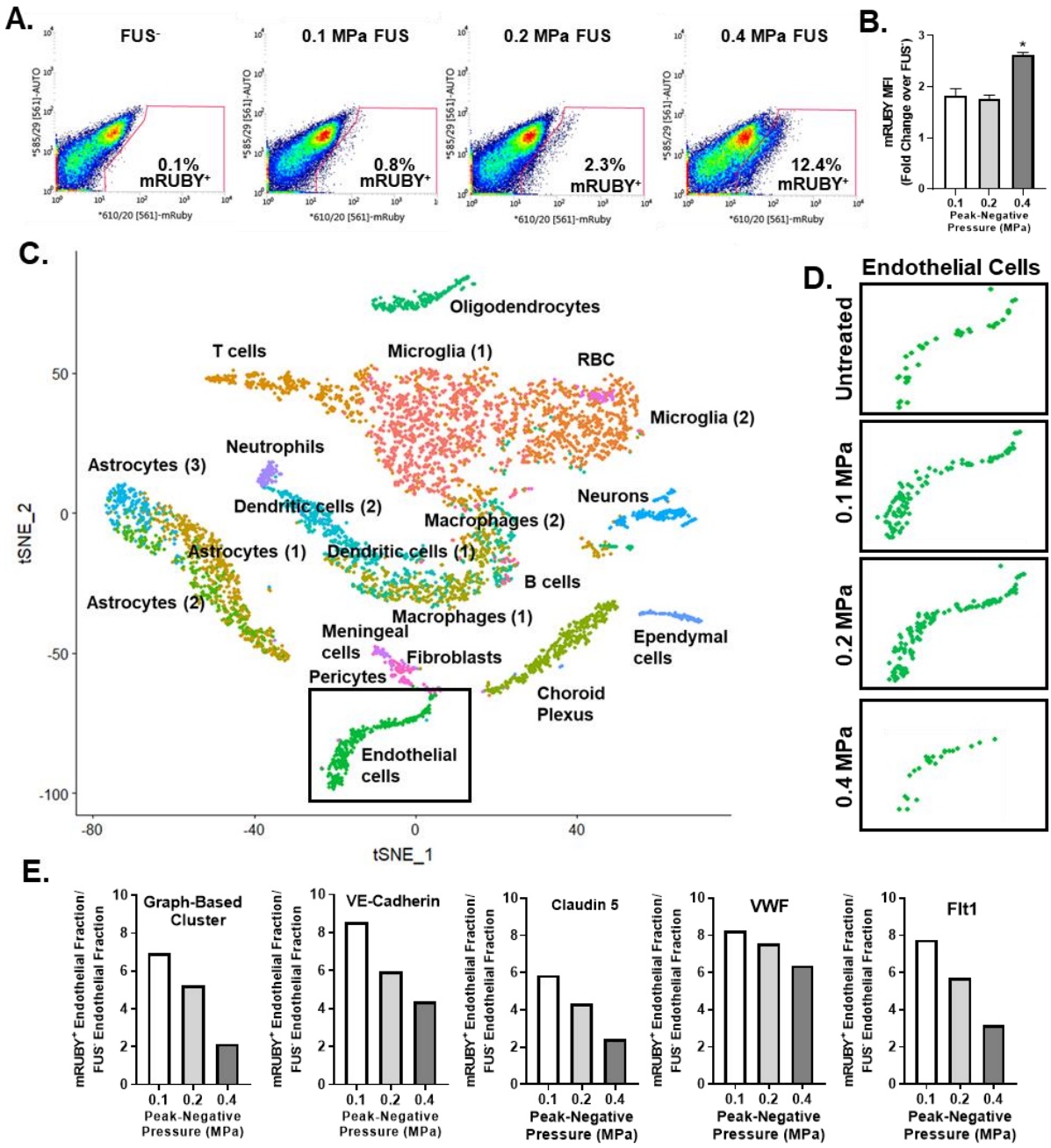
A.
FUS-
0.1 MPa FUS
0.2 MPa FUS
0.4 MPa FUS
0.1% mRUBY+
0.8% mRUBY+
2.3% mRUBY+
12.4% mRUBY+
*610/20 [561]-mRuby
*585/29 [561]-AUTO
B.
mRUBY MFI (Fold Change over FUS-)
Peak-Negative Pressure (MPa)
C.
Oligodendrocytes
T cells
Microglia (1)
RBC
Microglia (2)
Neutrophils
Astrocytes (3)
Dendritic cells (2)
Macrophages (2)
Neurons
Astrocytes (1)
Dendritic cells (1)
B cells
Astrocytes (2)
Macrophages (1)
Meningeal cells
Fibroblasts
Ependymal cells
Pericytes
Choroid Plexus
Endothelial cells
tSNE_1
tSNE_2
D.
Endothelial Cells
Untreated
0.1 MPa
0.2 MPa
0.4 MPa
E.
Graph-Based Cluster
VE-Cadherin
Claudin 5
VWF
Flt1
mRUBY+ Endothelial Fraction/ FUS- Endothelial Fraction
Peak-Negative Pressure (MPa)

Figure 3.4. Cell identification and enrichment using flow cytometry and single cell RNA sequencing. A) Flow cytometry gating used to sort mRUBY^{+} transfected cells from whole brain tissue samples. The mRUBY^{+} fraction increased with peak-negative acoustic pressure. B) mRUBY mean fluorescence intensity (MFI) for each peak-negative acoustic pressure. *P<0.0001 vs. 0.1 and 0.2 MPa. One Way ANOVA followed by Dunnett's multiple comparison tests. C) tSNE dimensionality reduction of aggregate sample containing cells from Untreated, 0.1 MPa FUS, 0.2 MPa FUS, and 0.4 MPa FUS treatment groups. Labels on graph identify corresponding cell clusters. Endothelial cells (green) are boxed. D) Endothelial cell clusters from tSNE analyses of Untreated and FUS-treated samples. Endothelial cell cluster size comparisons between FUS-treated groups reflect the relative proportion of transfected cells that are endothelial at each peak-negative pressure. E) Bar graphs showing that low peak-negative pressures markedly enrich the endothelial fraction of transfected cells. The method used to identify endothelial cells [i.e. Graph-Based Clustering or expression of individual markers of brain endothelium, such as VE-Cadherin; Claudin 5; Von Willebrand Factor (VWF); or Vascular Endothelial Growth Factor Receptor-1 (Flt1)] did not significantly affect the relationships between peak-negative acoustic pressure and endothelial enrichment.

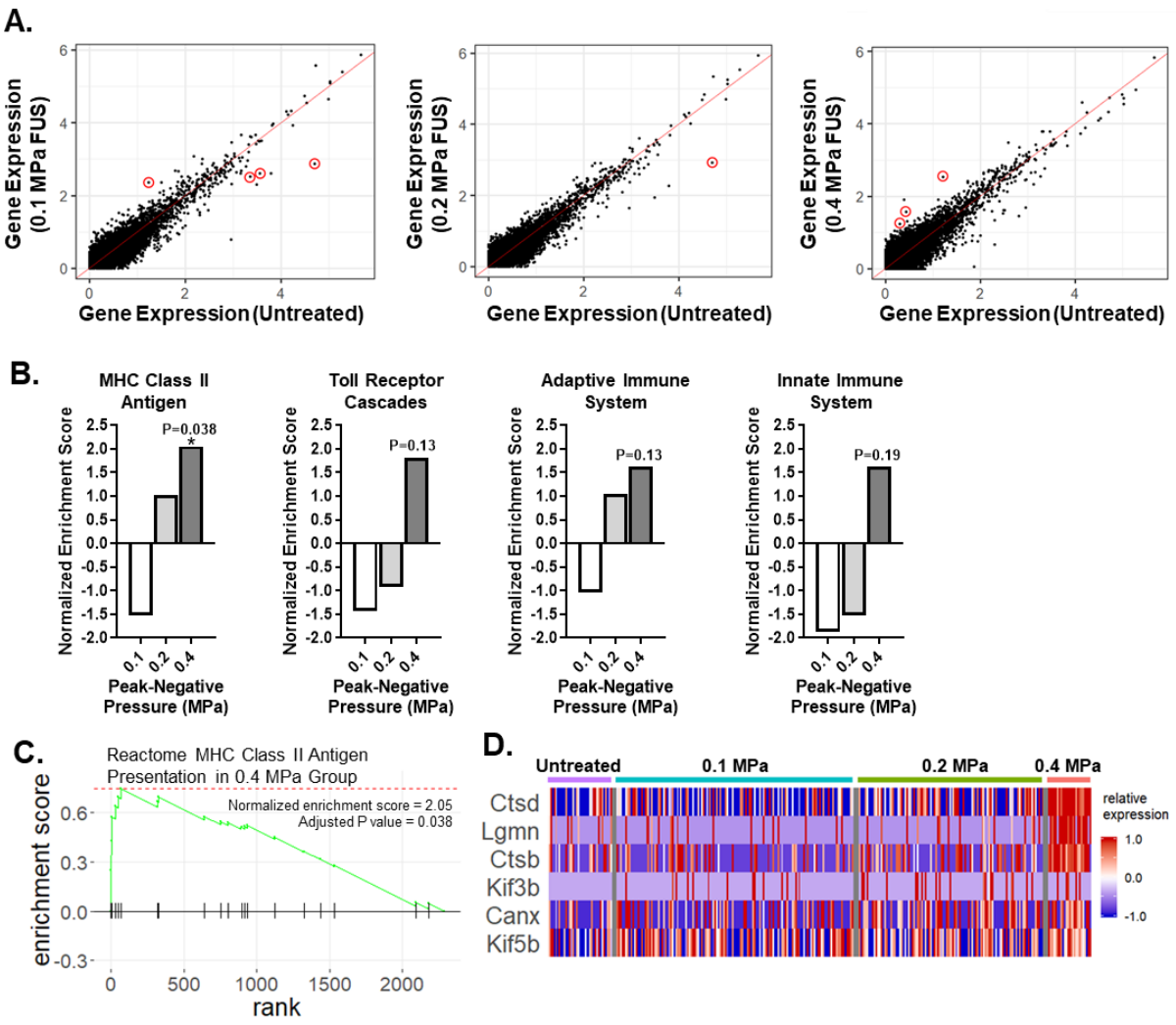

Figure 3.5. Single cell RNA sequencing analyses indicate that sonoselective transfection with low pressure FUS does not significantly affect the transcriptome of brain capillary endothelial cells in-vivo. A) Expression of individual genes in mRUBY^{+} endothelial cells transfected with 0.1, 0.2, and 0.4 MPa FUS in comparison to the expression of the same genes in untreated endothelial cells. Only 8 total transcripts were differentially expressed (P<0.05; red circles). B) Selected gene set enrichment analyses for mRUBY^{+} endothelial cells. While some gene sets associated with inflammation approached significance in the 0.4 MPa group, only the MHC Class II Antigen Presentation gene set was significantly enriched compared to untreated endothelium. C) Enrichment plot for the MHC Class II Antigen Presentation gene set. D) Leading edge analysis of the MHC Class II Antigen Presentation gene set, showing that the Ctsd, Lgmn, and Ctsb transcripts predominantly drive enrichment of this gene set at 0.4 MPa.

3.7 Chapter 3 Supplemental Figures

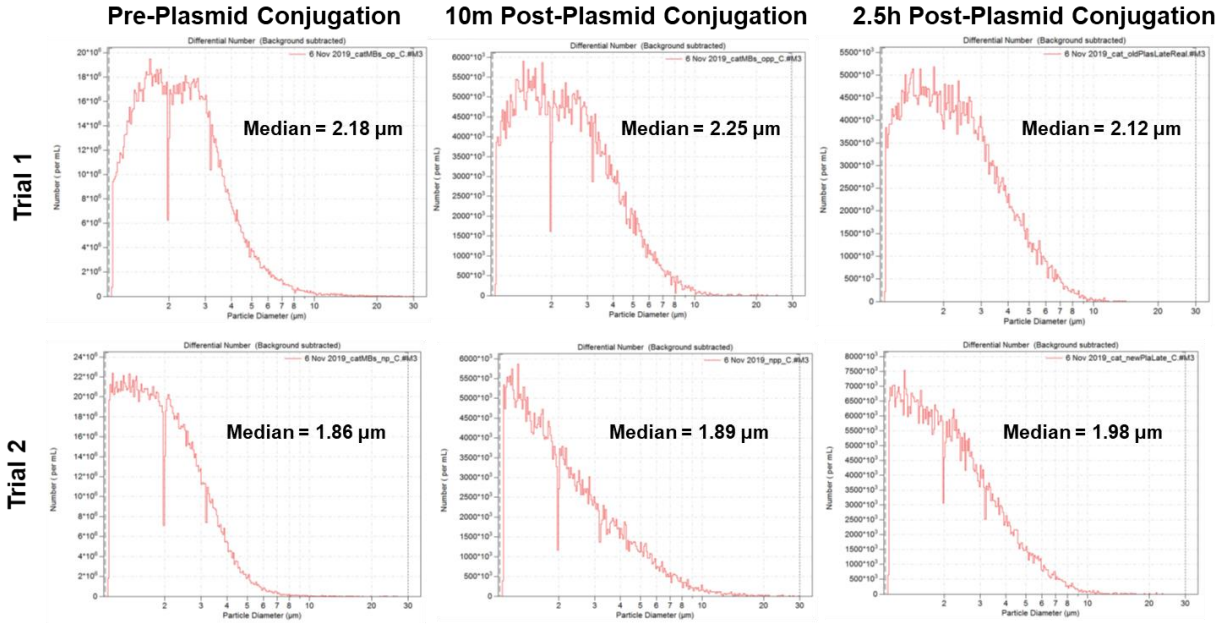

Figure 3.S1. Size distributions of cationic MBs, pre- and post-plasmid conjugation. Data from 2 independent trials show that plasmid conjugation does not affect MB size. MB-plasmid conjugates remain stable for at least 2.5 hours.

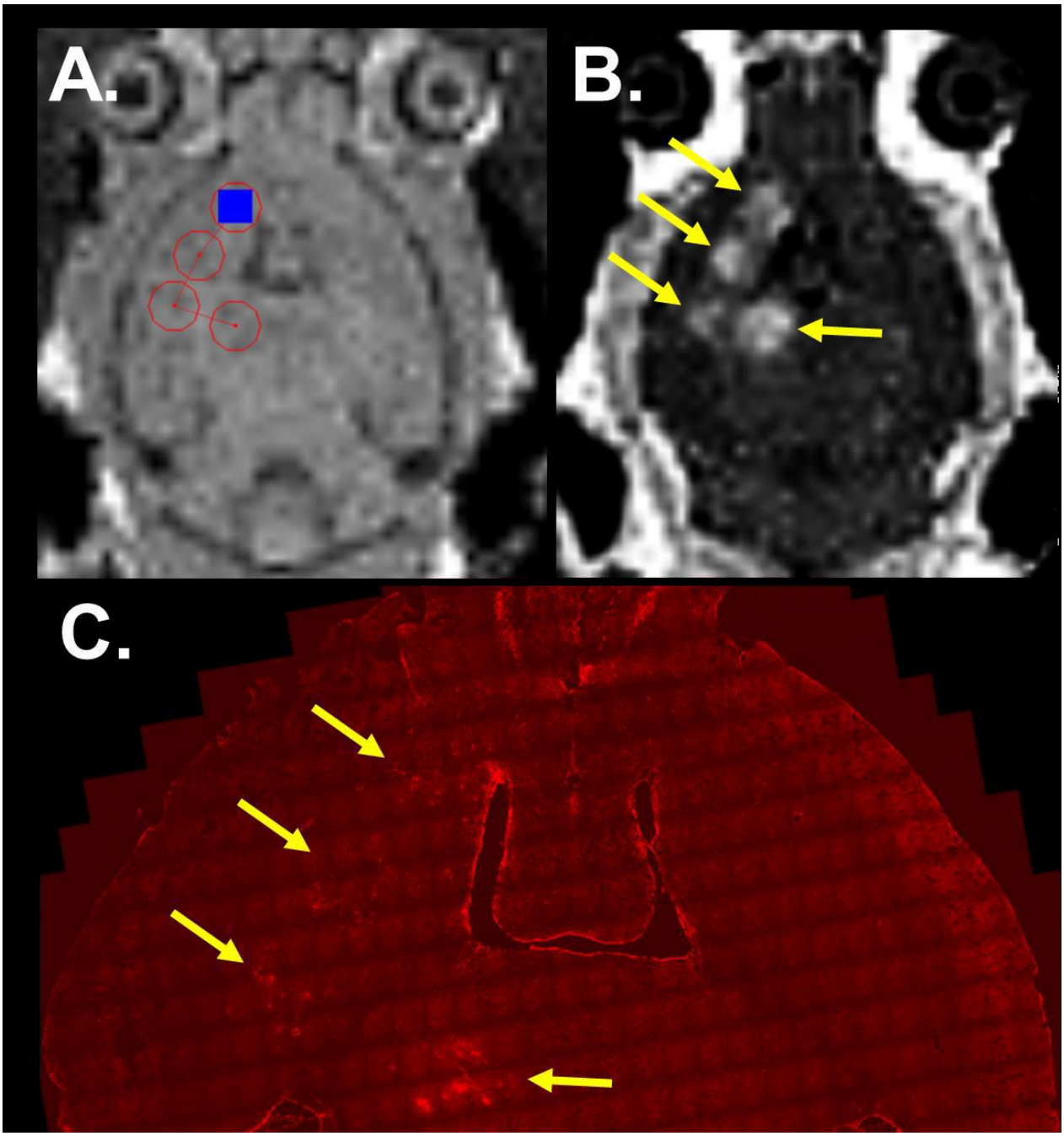

Figure 3.S2. mCherry expression colocalizes with FUS treated brain regions. A) Pre-FUS MRI with overlaid 4-spot treatment plan (red circles). B) Post-FUS (0.4 MPa) BBB opening is evident using T1 contrast MRI, with a spatial distribution corresponding to the treatment plan. C) mCherry expression in the same brain is detectable in the FUS-treated regions (arrows).

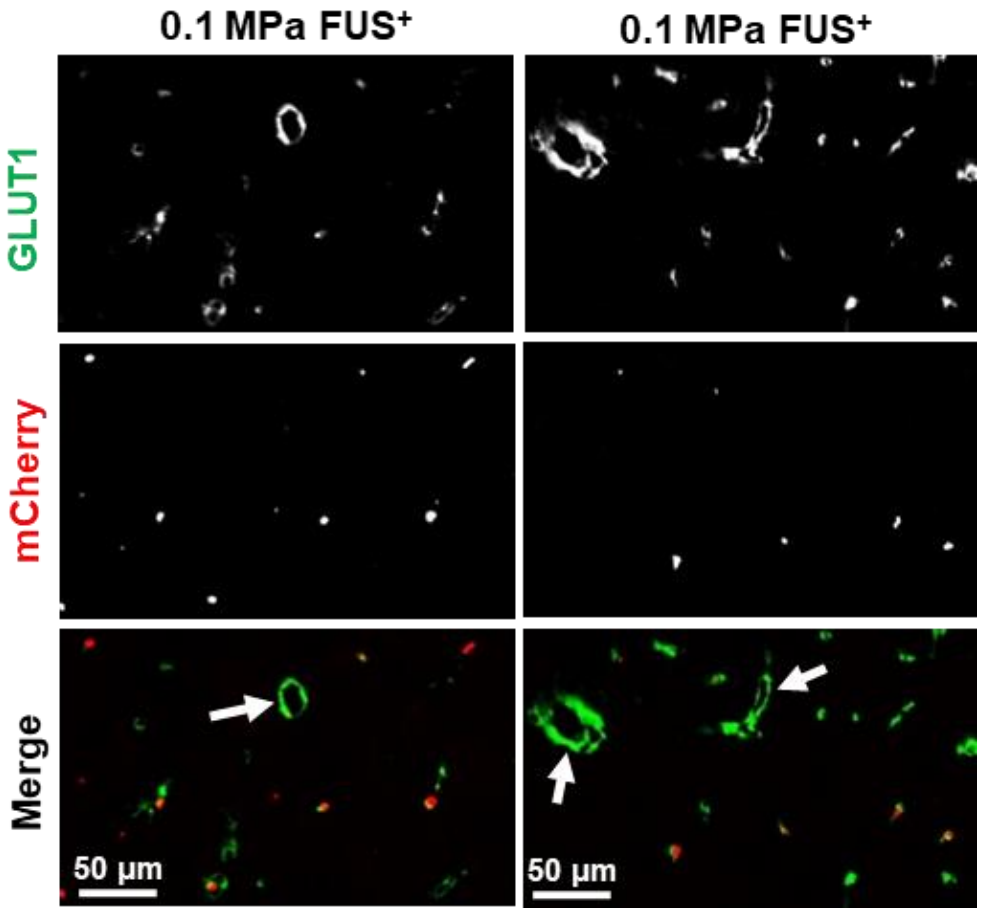

Figure 3.S3. Sonoselective transfection of cerebrovascular endothelium using 0.1 MPa FUS is restricted to small (i.e. < 5 µm) microvessels. Representative confocal images of FUS^{+} (0.1 MPa) brain tissue sections showing expression of mCherry reporter gene (red) with respect to endothelial cells (GLUT1; green). Yellow arrowheads denote co-localization of mCherry with endothelium in capillary-sized microvessels. White arrows denote larger microvessels, all of which are devoid of mCherry expression.

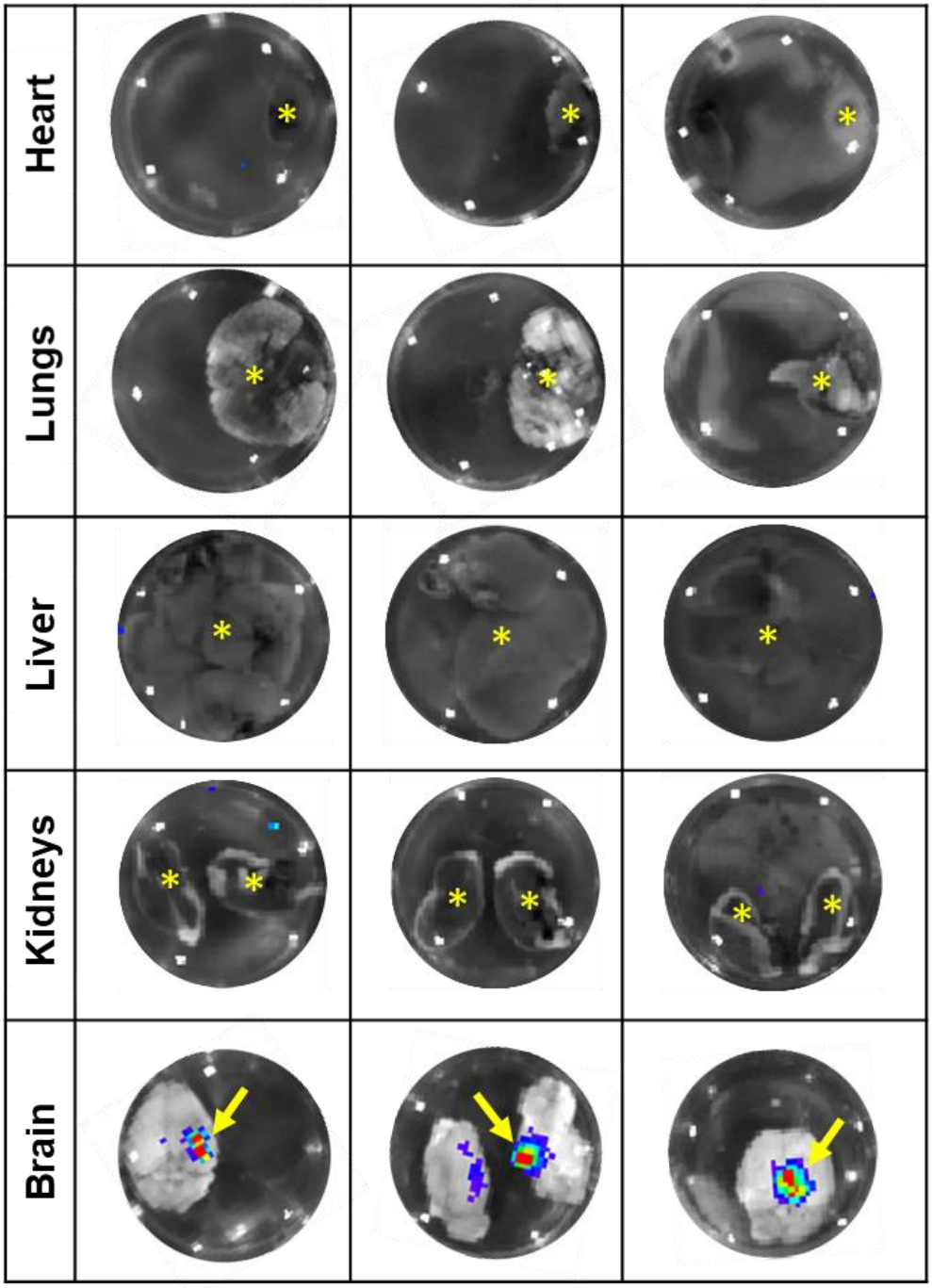

Figure 3.S4. Luciferase transgene was detected in 0.1 MPa FUS-treated brains, but not in off-target organs. Bioluminescence images of heart, lungs, liver, kidneys, and brains from mice (n=3) taken 24h after luciferase plasmid was coupled to cationic microbubbles, injected I.V., and delivered to cerebrovascular endothelium under stereotactic guidance using 1 MHz FUS with a PNP of 0.1 MPa. Luciferase was robustly expressed in FUS-treated brains (arrows), but was undetectable in off-target organs (asterisks). The brain in the middle row was inadvertently bisected during processing.

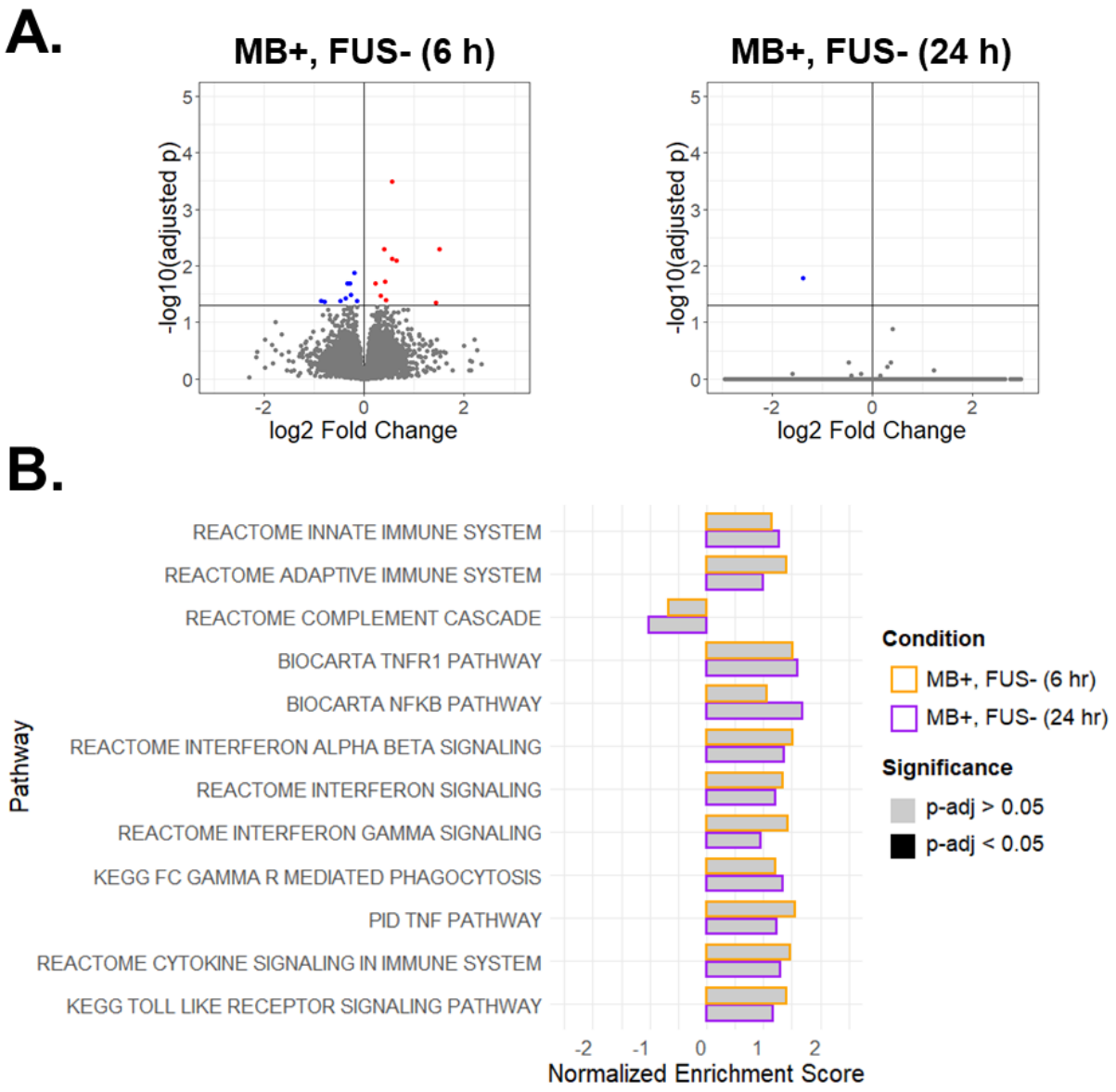

Figure 3.S5. Systemic injection of MBs without FUS application elicits minimal transcriptomic effects in the brain. A) Volcano plots showing that, in the complete absence of FUS, systemic administration of plasmid-conjugated MBs elicits almost no differential gene expression at both 6 h and 24 h. B) Gene set enrichment analysis of several pathways associated with inflammation and/or other immunological responses. None of these pathways were enriched or suppressed with MB injection alone. Bar borders correspond to time post-injection and bar fills correspond to the significance of the pathway's Normalized Enrichment Score.

3.8 Chapter 3 Supplemental Tables

	0.1 MPa		0.2 MPa		0.4 MPa	
	6 h	24 h	6 h	24 h	6 h	24 h
IL-10	1.0000	1.0000	1.0000	1.0000	1.0000	1.0000
IL-11	0.8320	1.0000	0.9998	1.0000	0.8024	0.9286
IL-13	1.0000	1.0000	0.9998	1.0000	1.0000	1.0000
IL-1RA	0.9894	1.0000	0.9998	0.9302	0.1045	0.5680
IL-4	0.9962	1.0000	0.9998	0.8803	0.9733	0.9765
IL-6	1.0000	1.0000	0.9998	1.0000	0.9551	0.9037

Table 3.S1. FDR adjusted p-values for relative expression levels of "anti-inflammatory" transcripts. Transcript expression significance levels are shown for FUS+MB groups at all 3 tested peak-negative pressures in comparison to the "MB only" control group. No significant differences were observed.

Chapter 4: Single-Cell Mapping of Focused Ultrasound-Transfected Brain

Alexander S. Mathew, Catherine M. Gorick, and Richard J. Price. *Gene Therapy*, 2021.
DOI: 10.1038/s41434-021-00226-0

4.1 Abstract

Gene delivery via focused ultrasound (FUS) mediated blood-brain barrier (BBB) opening is a disruptive therapeutic modality. Unlocking its full potential will require an understanding of how FUS parameters [e.g. peak-negative pressure (PNP)] affect transfected cell populations. Following plasmid (mRuby) delivery across the BBB with 1 MHz FUS, we used single cell RNA-sequencing to ascertain that distributions of transfected cell types were highly dependent on PNP. Cells of the BBB (i.e. endothelial cells, pericytes, and astrocytes) were enriched at 0.1 and 0.2 MPa PNP, while transfection of cells distal to the BBB (i.e. neurons, oligodendrocytes, and microglia) was augmented at 0.4 MPa PNP. PNP-dependent differential gene expression was observed for multiple cell types. Cell stress genes were upregulated proportional to PNP, independent of cell type. Our results underscore how FUS may be tuned to bias transfection toward specific brain cell types in-vivo and predict how those cells will respond to transfection.

4.2 Introduction

Despite increasing knowledge of the underlying mechanisms of many neurological diseases, safe and effective treatments are often lacking. Anatomical, physiological, and cellular obstacles make therapeutic intervention in the central nervous system (CNS) extremely challenging. High vascularity and limited regenerative capacity of the CNS, along with the thickness and nonuniformity of the skull, significantly enhance the risk profile of any surgical approach. The blood-brain barrier (BBB), an arrangement of endothelial cells, tight junctions, basement membrane, astrocytic endfeet, and transport proteins common to most CNS vasculature, limits the vast majority of systemically injected therapies from accessing the brain (7). Furthermore, current therapies for major neurological pathologies such as Alzheimer's Disease, Parkinson's Disease, and multiple sclerosis (MS), are transiently effective and/or only palliative. Thus, there exists a pressing need for the development of non-invasive, spatially-targeted, and durable treatment approaches across the spectrum of neurological disorders.

Focused ultrasound (FUS) mediated BBB disruption (BBBD) holds significant promise toward overcoming the aforementioned obstacles (46, 54, 221). In this modality, gas-filled microbubbles (MB) and therapeutic agents are injected intravenously. Under image guidance, an extracorporeal transducer then directs conforming acoustic waves toward a pathologic region of the brain. These waves pass harmlessly through the skull and converge on the targeted region, causing the circulating MB to oscillate. These oscillations impart mechanical forces on cerebrovascular endothelium, temporarily disrupting BBB integrity and allowing therapeutics into the brain parenchyma. FUS mediated BBBD is targeted, non-invasive, and repeatable and has facilitated successful delivery of chemotherapies (222–224), antibodies (225–227), and even neural stem cells (160, 161).

Importantly, FUS BBBD also enables the delivery of systemically circulating gene therapies to the CNS (109, 125, 228–231). Indeed, non-invasive gene delivery to the brain by

FUS under precise image-guidance offers the prospect of curative therapies. However, translational hurdles still remain. First, knowledge of which brain-resident cell populations are most likely to be transfected after FUS-mediated BBBD and how transfection specificity depends on FUS parameters (e.g. PNP) are still unknown. Second, because the biophysical mechanisms through which gene delivery to the brain is achieved with FUS are complex, it is difficult to predict how FUS parameters like PNP will affect which cells are transfected and to what extent. Indeed, different brain cell types may exhibit markedly discrepant responses to FUS application and subsequent transfection. Recently, we used immunofluorescence analyses and single cell RNA sequencing (scRNA seq) to determine that the specificity of transfection of endothelial cells of the BBB is inversely proportional to peak-negative pressure (PNP), a phenomenon we term “sonoselective” transfection (123). Herein, we extend these previous scRNAseq studies considerably to investigate how the distribution of transfected brain-resident cell populations and their transcriptomes are affected by FUS PNP.

4.3 Results

4.3.1 Focused ultrasound BBBD and brain cell transfection

Our experimental pipeline is shown in Figure 4.1. Briefly, we intravenously injected cationic MBs and mRuby plasmid followed by MRI-guided FUS (1.1 MHz) targeted to the right striatum at either 0 MPa, 0.2 MPa, or 0.4 MPa PNP (estimated to be effectively 0 MPa, 0.164 MPa, and 0.328 MPa after skull attenuation). As expected, both MRI contrast enhancement in the targeted region and harmonic acoustic emissions were significantly greater at 0.4 MPa compared to 0.2 MPa (Figure 4.S1). After allowing 48 hours for sufficient expression of mRuby by transfected cells, mouse brains were harvested and dissociated into single cell suspensions. We then isolated live mRuby-expressing cells by fluorescence activated cell sorting (FACS) and performed scRNA-seq. 12.4% of dissociated cells treated at 0.4 MPa were $mRuby^+$, compared to 2.3% treated at 0.2 MPa (Figure 4.1). However, it is important to emphasize that we harvested the entire quadrant of the brain to ensure maximum cellular yield. Thus, these percentages are not representative of overall transfection efficiency. Given the weight of the harvested brains, the average density of the murine brain, and the volume of the -6 dB focal region for our transducer (i.e. 10.7 mm^3), we estimate the true transfection efficiencies to be 28.5% and 5.4% at 0.4 MPa and 0.2 MPa, respectively. To establish the baseline proportions of brain-resident cell types and account for biases introduced in our dissociation protocol, cells from the 0 MPa treatment group were sequenced without mRuby FACS.

4.3.2 Focused ultrasound-transfected cell-type distributions depend on peak-negative pressure

To assign cell identities to our dataset, we performed graph-based clustering followed by comparison of globally distinguishing genes within each cluster against scRNA-seq databases. After filtering ambiguous clusters and pooling those of the same class, we identified 6 distinct

cell types, namely astrocytes, endothelial cells, microglia, neurons, oligodendrocytes, and pericytes (Figure 4.2A). The proportions of these mRuby+ cell types were dependent on PNP (Figure 4.2B). Specifically, 0.2 MPa FUS transfection led to marked enrichment of cells comprising and in contact with the BBB (i.e. endothelial cells, pericytes, and astrocytes) compared to control, while 0.4 MPa FUS led to a transfection distribution in between that of 0.2 MPa transfection and 0 MPa controls (Figure 4.2C). Thus, cells of the BBB (i.e. endothelial cells, pericytes, and astrocytes) are relatively enriched at lower FUS PNP while those farther from the BBB (neurons, oligodendrocytes, and microglia) are more efficiently transfected at higher FUS PNP.

4.3.3 Transcriptional responses of individual focused ultrasound-transfected cells

To assess cell-type specific transcriptional responses to FUS-mediated BBBD and transfection, we performed differential expression testing, comparing 0.2 MPa and 0.4 MPa transfected cells to matching populations from the 0 MPa control group across multiple cell types (Figure 4.3A-D). Transfected microglia exhibited massive differential gene expression (1630 significantly regulated transcripts) when compared to 0 MPa control cells, with 0.4 MPa PNP FUS exerting a much stronger effect than 0.2 MPa PNP FUS (Figure 4.3A and 4.3E). While neurons exhibited the same PNP-dependent response, far fewer differentially regulated transcripts were identified overall (Figure 4.3B and 4.3E). In contrast, neither oligodendrocytes (Figure 4.3C and 4.3E) nor astrocytes (Figure 4.3D and 4.3E) differentially expressed more transcripts at the higher PNP (i.e. 0.4 MPa). Overall, our results indicate that the absolute numbers and identities of significantly differentially expressed genes depended on cell type and FUS PNP (Figure 4.3E, Table 4.S1). Finally, despite the robust cell type-specific responses shown in Figure 4.3, we questioned whether there might exist sets of genes that are affected by FUS regardless of the cell type. Interestingly, a careful curation of our data set revealed that

several genes associated with cellular stress and inflammation, including *CTSD, CTSB, LY86, CD68, LYZ2,* and *TYROBP,* are indeed significantly upregulated in multiple cell types as a function of increasing PNP (Figure 4.4). A complementary analysis revealed *CKB, DNAJA1, HBB-BS, HSPA8, JUN, JUND, and RPS27* were downregulated across multiple cell types with increasing PNP (Figure 4.S2).

4.4 Discussion

Conventional approaches for gene delivery to the CNS can be limited by their invasiveness, poor localization, systemic toxicity, or inefficient transit across the BBB. FUS activation of systemically administered MB surmounts all of these, as it is noninvasive, targeted, safe, and transiently disrupts the BBB (232). While we and others have established the potential of this technology for gene therapy (109, 125, 228–231), considerable knowledge gaps still exist. Indeed, we reason that acquiring a more comprehensive understanding of (i) how FUS parameters affect which cell types are transfected and (ii) how these cells respond to transfection at the transcriptional level will permit fine tuning of FUS-mediated transfection approaches for selected applications. Toward this end, we used scRNA-seq to quantify proportions of brain-resident cell types transfected by FUS, their transcriptional responses 48 h post treatment, and the relationship of these metrics to PNP. Both 0.2 MPa and 0.4 MPa FUS application elicited successful transfection of endothelial cells, astrocytes, pericytes, neurons, oligodendrocytes, and microglia. While 0.2 MPa PNP preferentially transfected BBB-associated cells (i.e. endothelial cells, astrocytes, and pericytes), 0.4 MPa PNP shifted transfected cell-type distributions to include more microglia, neurons, and oligodendrocytes. These data, in conjunction with prior histological studies demonstrating that 0.1 MPa PNP is highly selective for endothelial cell transfection (123), are consistent with the hypothesis that the probability of a cell being transfected by FUS is directly proportional to PNP and inversely proportional to distance from the microcirculation. Moreover, at least in the context of focused ultrasound transfection, our results suggest that any cell-type differences in transfection potential that may exist appear to be overridden by physical factors. While the extent and nature of significant differential gene expression were cell- and PNP-dependent, we identified several cellular stress-associated genes that were consistently upregulated independent of cell type and proportional to PNP. Together, these results provide high-resolution insight into the cellular implications of FUS

mediated transfection that will ultimately refine preclinical design and accelerate clinical translation.

4.4.1 Distance from Vasculature Predicts Cell Types Transfected by FUS

Our experimental and computational pipeline enabled unbiased identification of 6 brain-resident cell types in the neurovascular unit (NVU). We noted a bias toward transfection of cells closer to the microcirculation, such as endothelial cells, astrocytes, and pericytes, especially at lower FUS PNP. Neurons, oligodendrocytes, and microglia were enriched with higher PNP, presumably because of enhanced plasmid availability beyond the BBB. Microglial activation in the context of PNP-dependent sterile inflammation may also lead to chemotaxis to the BBB, thereby increasing microglial propensity for transfection. Overall, our results are in agreement with previous work from our group, wherein gene-bearing nanoparticles were delivered instead of plasmid (145). In that study, we observed higher transfection of astrocytes compared to neurons by immunofluorescence. Our model is also consistent with work in which FUS mediated delivery of recombinant adeno-associated virus (rAAV) elicited transduction of significantly more astrocytes than neurons (233). However we note disagreement with another rAAV study, which transduced primarily neurons (228). This discrepancy could be attributed to differences in cellular uptake, expression stability for FUS-enhanced delivery of bacterial vs viral vectors, or FUS experimental parameters. Other studies of FUS-mediated viral gene delivery that demonstrate highly selective neuronal transgene expression utilize neuron-specific promoters (109). Indeed, the overall approach and results presented here may be especially useful for choosing FUS parameters that best synergize with gene therapy approaches that utilize cell-specific promoters by biasing plasmid delivery to the cell type(s) of interest. Furthermore, independent of the specific gene delivery vehicle that is chosen for focused

ultrasound transfection, our study provides a framework for how scRNA seq can be used to inform and optimize the transfection of selected cell types in the brain.

4.4.2 FUS Activation of MBs Induces a Sterile Inflammatory Response

Several genes associated with cellular stress and inflammation were upregulated across multiple cell types in proportion to PNP. While many studies have demonstrated that FUS-mediated BBBD results in minimal damage at the tissue level (54, 200, 234), impacts at the cellular and molecular levels are actively under investigation. Transcriptomic and proteomic profiling by multiple groups have found that, under certain FUS and MB conditions, FUS mediated BBBD may elicit a sterile inflammatory response in the brain parenchyma (123, 174, 235, 236). The precise mechanistic relationship between FUS-mediated BBBD and sterile inflammation remains unclear. Possible causes include direct acoustic damage to BBB, NVU injury caused by cavitation-induced shockwaves, ischemia reperfusion injury caused by transient vasospasm, and exposure of the brain parenchyma to blood products. Sonoporation, one of the mechanisms by which FUS is proposed to enhance gene delivery, has been shown to generate large irreversible pores, increase reactive oxygen species, reduce endoplasmic reticulum mass, increase apoptosis, and delay the cell cycle (188, 237, 238). It is probable that multiple interactions contribute to sterile inflammatory response induced by FUS. Given that we harvested tissue 48 h post-FUS to allow time for sufficient transgene expression, the differential gene expression profile we report is consistent with a landscape of resolving inflammation. We noted pressure dependent upregulation of *CTSD*, *CTSB, LY86*, *LYZ2, CD68,* and *TYROBP* across multiple cell types. Cathepsin D, the protein product of *CTSD*, is a protease expressed in the lysosome involved in antigen processing, apoptosis, and biomolecule degradation (239, 240). Studies of its role in Alzheimer's disease suggest it is upregulated during neuronal repair (241). Cathepsin B, another lysosomal protease, is activated in response to diverse

inflammatory stimuli in multiple brain cell types and contributes to programmed cell death (242, 243). The function of LY86 is not well understood, though it is thought to play a role in regulating inflammation and toll-like receptor (TLR) signaling (244, 245). CD68 is a lysosomal protein that is upregulated in actively phagocytosing microglia (246). While its expression was clearly the highest in microglia, we observed PNP dependent upregulation in all cell types. Non-myeloid expression of CD68 has been reported before as evidence of increased lysosomal activity (247). Further evidence of microglial activation is supported by the PNP-dependent upregulation of *LYZ2* (Lysozome 2), a powerful antimicrobial hydrolase. Increases in *LYZ2* across multiple cell types were also observed in a scRNA-study of Niemann-Pick disease, a neurodegenerative pathology characterized by inappropriate activation of innate immunity (248). Similarly, TYRO protein tyrosine kinase-binding protein (TYROBP, the protein product of *TYROBP*) is also primarily expressed in microglia. TYROBP has complex functions in microglia, having roles in increasing phagocytic activity and decreasing cytokine production (249). Non-myeloid expression of TYROBP has also been linked to neuroinflammation(250). Interestingly, many of the genes highlighted by our analysis exactly match those found in a gene cluster specific to resolution of neuroinflammation(251). Notably, we did not detect significant upregulation of classical markers of sterile neuroinflammation such *AIF1* in microglia, *GFAP* in astrocytes, and *ICAM1* in endothelial cells. Thus, our differential expression analysis is consistent with a resolving PNP-dependent inflammatory response 48 h post-FUS.

4.4.3 Limitations

There are some limitations of this investigation. The requirement for dissociation of treated tissue to viable single cell suspensions and myelin removal prior to scRNA-seq likely limited the yield of large complex cells such as neurons or oligodendrocytes. We corrected for this methodological limitation by making comparisons to sequences from non-transfected cells

that were subject to the same isolation methods. Nonetheless, while this approach does allow us to make relative comparisons, we are not able to accurately report the absolute extent of transfection on a per-cell-type basis without making significant assumptions. Further, the process of mechanical and enzymatic dissociation itself may have imparted transcriptional effects on the sequenced cells. Finally, due to the high processing complexity and cost of scRNA-seq, replicates were not sequenced separately. Instead, we pooled multiple biological replicates from each condition prior to FACS and scRNA-seq library preparation and subsequently ran all samples in the same sequencing run. This approach is common (252, 253) and has been shown to mitigate batch effects and improve statistical power (254, 255).

4.4.4 Conclusions

To summarize, we used single cell RNA-sequencing to study the effects of 0.2 MPa and 0.4 MPa FUS-mediated transfection on the brain. At 48 h post-treatment, we observed lower overall transfection at 0.2 MPa compared to 0.4 MPa, but higher selectivity for cells comprising the BBB, namely endothelial cells, astrocytes, and pericytes. Differential gene expression analysis highlighted PNP dependent, cell-type independent upregulation of genes associated with cellular stress. This work has significant implications for the design of future investigations leveraging FUS-mediated transfection. For applications where higher cell-type specificity and/or lower cellular stress are required, lower PNPs should be used. Inversely, for applications where higher general transfection is desired, and when a sterile inflammatory response is tolerable (or even desirable), higher PNPs may be recommended. Other FUS experimental parameters (such as frequency, pulsing interval, duty cycle, burst length, and MB dose) are also likely to affect transfection selectivity and efficiency and could be tested in future investigations.

4.5 Materials and Methods

4.5.1 Animals

Male C57BL/6 mice were purchased from Charles River and maintained on a 12/12 hour light/dark cycle. Mice used in the experiments weighed between 22 and 28 g and were given food and water *ad libitum*. All animal experiments were approved by the Animal Care and Use Committee at the University of Virginia and conformed to the National Institutes of Health regulations for the use of animals in research.

4.5.2 Cationic Lipid-Shelled Microbubble Fabrication

To synthesize the cationic lipid-shelled MBs, we made a mixure of 2 mg/ml 1,2-distearoyl-sn-glycero-3-phosphocholine (DSPC; Avanti Polar Lipids, Alabastar, Alabama), 2 mg/ml polyethylene glycol 6000 monostearate (PEG 6000 MS; Stepan Kessco, Northfield, Illinois), and 0.8 mg/ml 1,2-distearoyl-3-trimethylammonium-propane (DSTAP; Avanti Polar Lipids, Alabastar, Alabama) in 0.9% NaCl (Baxter, Deerfield, Illinois). The mixture was filtered through a 0.2 um Nylon sterile filter, sparged with decafluorobutane gas (F2 Chemicals Ltd; Preston, United Kingdom), and then sonicated at the highest power (20 kHz, 30 s) with an ultrasound disintegrator (XL2020; Misonix, Farmingdale, New York) to generate the MBs. MBs were aliquoted into 13 mm glass vials, which were stoppered for storage after filling the headspace with decafluorobutane gas. The MBs were cleaned by flotation centrifugation before each experiment to remove residual micelles. An aliquot of the MB solution was centrifuged at 1000 rpm for 10 minutes, and the infranatant was removed and the bubbles resuspended in degassed saline. This process was repeated three times before the final resuspension of the bubbles at a concentration between 1.5 and $2*10^9$ MBs/ml. MBs were sized and counted using a Coulter counter (Multisizer 3; Beckman Coulter, Fullerton, California).

4.5.3 Plasmid Preparation and Conjugation to Microbubbles

The mRuby2-N1 plasmid was a gift from Michael Davidson (Addgene plasmid #54614; http://n2t.net/addgene:54614; RRID:Addgene_54614). The plasmid features an mRuby2 gene under the control of a CMV enhancer and promoter for constitutive expression. Our studies demonstrate that peak expression is achieved by this plasmid by 24 hours after transfection and is maintained for about 1 day before beginning to decline. The plasmid was provided from Addgene (Watertown, Massachusetts) in the form of agar stabs of DH5α *E. coli* transformed with the plasmid. The bacteria were expanded in LB media (Sigma-Aldrich, St. Louis, Missouri) containing kanamycin (Sigma-Aldrich), and then the plasmid was collected and purified using an Endo-Free Maxiprep Kit (Qiagen, Germantown, Maryland). Plasmid was resuspended in Tris-EDTA buffer at a concentration between 400 and 500 ng/ul and stored at -20 degrees Celsius. Plasmid concentration was determined using a NanoDrop ND-1000 spectrophotometer (NanoDrop Technologies, Wilmington, Delaware).

On the morning of experiments, the purified plasmid was thawed and added to the cleaned MB solution at a ratio of 1.5 ug plasmid per 10^7 microbubbles. This ratio is consistent with prior studies of DNA binding to cationic MBs(209, 210). This mixture was allowed to incubate at room temperature for 10 min to permit the electrostatic coupling of the positively-charged bubbles and negatively-charged DNA, and was then stored on ice until use. Roughly 20-25% of the plasmid added to the MBs bound, for a total of 0.03 to 0.035 pg per MB.

4.5.4 MRI-Guided FUS-Mediated Plasmid Delivery

Male C57BL/6 mice were anesthetized with an intraperitoneal injection of 120 mg/kg ketamine, 12 mg/kg xylazine, and 0.08 mg/kg atropine in sterilized 0.9% saline. A tail vein

catheter was inserted to permit intravenous injections of MBs, plasmid, and the MRI contrast agent. The heads of the mice were shaved and depilated, and the animals were then placed in a supine position over a degassed water bath coupled to an MR-compatible small animal FUS system (RK-100; FUS Instruments, Toronto, Canada). The entire system was then placed in a 3T MR scanner (Magnetom Trio; Siemens Medical Solutions, Malvern, Pennsylvania). A 2-inch cylindrical transmit-receive RF coil, designed and built in-house, was placed around the mouse's head to maximize imaging SNR. Baseline T1-weighted MR images were acquired and used to select 4 FUS target locations in and around the right striatum.

Mice received an injection of the conjugated MBs and mRuby plasmid (2×10^5 MBs/g body weight), followed by injection of additional free plasmid to reach a total plasmid dose of 40 ug, followed by 0.1 mL of 2% heparinized saline to clear the catheter. The total plasmid dosage of 40 ug is consistent with prior studies of cationic MB-mediated gene delivery(209, 211, 212). However, since we utilize a bolus injection of MBs here (as opposed to a slow infusion), we reduced the dosage of MBs to 2×10^5, which only allowed for a fraction of the plasmid to be delivered in MB-bound form. Thus, the injection of free plasmid immediately following the MBs was used to achieve the remainder of the 40 ug dose.

Sonication began immediately after clearance of the catheter. Sonications were performed at 0, 0.2, or 0.4 MPa PNP using a 1.1 MHz single element focused transducer (FUS Instruments, Toronto, Canada) operating in 10 ms bursts, 0.5 Hz pulse repetition frequency and 2 minutes total duration. These PNPs are free-field, nonderated measurements with a hydrophone in a water tank at a target distance equivalent to the treatment distance. Immediately following the FUS treatment, mice received an intravenous injection of Gd-DPTA contrast agent (0.5 ul/g body weight; Magnevist; Bayer Health Care, Indianola, Pennsylvania), and T1-weighted contrast-enhanced images were acquired to assess BBB opening. Animals

were removed from the MRI and placed on a warm pad for 30 minutes prior to reversal of the anesthetic with antisedan (1 mg/ml).

4.5.5 Passive Cavitation Detection

Acoustic emissions were detected with a 2.5 mm wideband unfocused hydrophone mounted in the center of the transducer. Acoustic signal was captured using a scope card (ATS460, Alazar, Pointe-Claire, Canada) and processed using an in-house built MATLAB algorithm. Acoustic emissions at the fundamental frequency, harmonics (2f, 3f, 4f), sub harmonic (0.5f), and ultra-harmonics (1.5f, 2.5f, 3.5f) were assessed by first taking the root mean square of the peak spectral amplitude (Vrms) in each frequency band after applying a 200 Hz bandwidth filter, and then summing the product of Vrms and individual sonication duration over the entire treatment period. Broadband emissions were assessed by summing the product of Vrms and individual sonication duration for all remaining emissions over the entire treatment period.

4.5.6 Fluorescence Activated Cell Sorting (FACS)

48 hours after FUS-treatment, mice were euthanized via CO_2 overdose. Immediately afterward, mouse brains treated with 0 MPa, 0.2 MPa, or 0.4 MPa (n = 3 per group) were harvested. The front right quadrants of each brain were excised and made into single cell suspensions using the Adult Brain Dissociation Kit (Miltenyi Biotech, Bergisch Gladbach, Germany). Suspensions were pooled by treatment group and incubated briefly with SYTOX Green Nucleic Acid Stain (1:500,000; Thermo Scientific) to identify live and dead cells. mRuby+ cells were isolated from 0.2 MPa, and 0.4 MPa cell suspensions using a BD Influx Cell Sorter (BD Biosciences, San Jose, California) with the 100 µm nozzle at 20 psi. The sort gate was

established using the 0 MPa cells as a reference. Live singlet mRuby+ cells were collected for single cell RNA-sequencing. FACS data were analyzed using FCS Express 6 software.

4.5.7 Single Cell RNA Sequencing and Analysis

After FACS, 0 MPa (unsorted), 0.2 MPa ($mRuby^+$), and 0.4 MPa ($mRuby^+$) single cell libraries were generated using the Chromium Controller (10X Genomics, Pleasanton, CA) with the Chromium Single Cell 3' GEM, Library & Gel Bead Kit v3 (10X Genomics) and Chromium Single Cell B Chip Kit (10X Genomics). An average of 1482 cells per condition were sequenced on a NextSeq 500 (Illumina) at an average depth of 92,409 reads per cell. The CellRanger v3.0.2 pipeline was implemented to first convert bcl2 reads to FASTQ files followed by alignment to the mm10 (Ensembl 84) mouse reference genome and filtering. All further single cell analysis was performed in R using Seurat v3.1.5(218) with default parameters unless otherwise specified. Cells with low read depth, low expression diversity, or high mitochondrial content were filtered out of the analysis. Cell clusters were computed by graph-based clustering and subsequently identified by comparing the top 20 globally distinguishing markers (i.e. those with p adjusted < 1E-240, average natural log fold change above all other cell types > 0.25, and expressed in at least 25% of that cell type) with those having high cell-type specificity scores in the PanglaoDB webserver(219). Clusters of the same cell type were merged. Cells of unclear significance in the context of FUS mediated transfection including, ependymal cells, choroid plexus cells, and peripheral leukocytes were removed from the analysis. Differential gene expression between endothelial subsets was performed using the MAST framework(220). PNP-dependent, cell-type independent genes were defined as those differentially regulated in at least 5/6 cell types at 0.4 MPa vs control with a p-value < 0.15.

4.6 Chapter 4 Figures

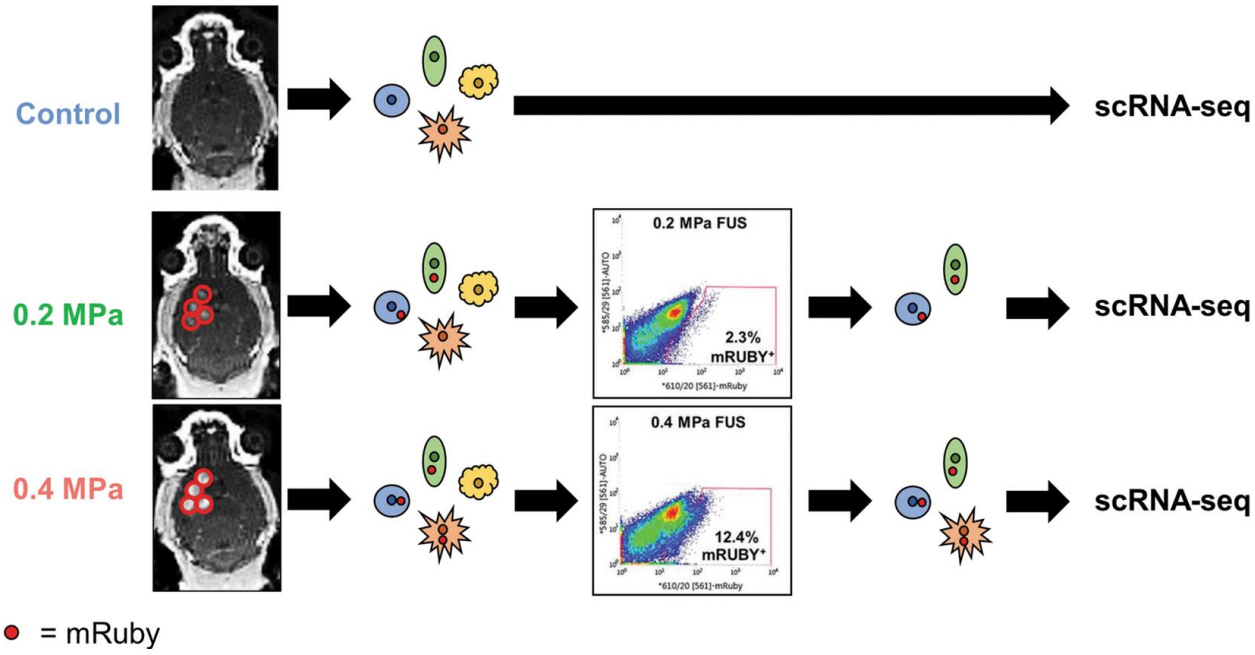

Figure 4.1. Overview of experimental methods. MR guided FUS was applied at either 0.2 MPa or 0.4 MPa to mouse striata following IV injection of mRuby plasmid conjugated to cationic MB. Brains were excised and dissociated, producing single cell suspensions containing both untransfected and transfected cells. Using cells from the control condition to define the mRuby gating strategy, mRuby+ cells were sorted from FUS-treated brains by FACS. Single cell RNA-sequencing was performed on untransfected, untreated cells from the control condition, mRuby+ cells from the 0.2 MPa condition, and mRuby+ cells from the 0.4 MPa condition.

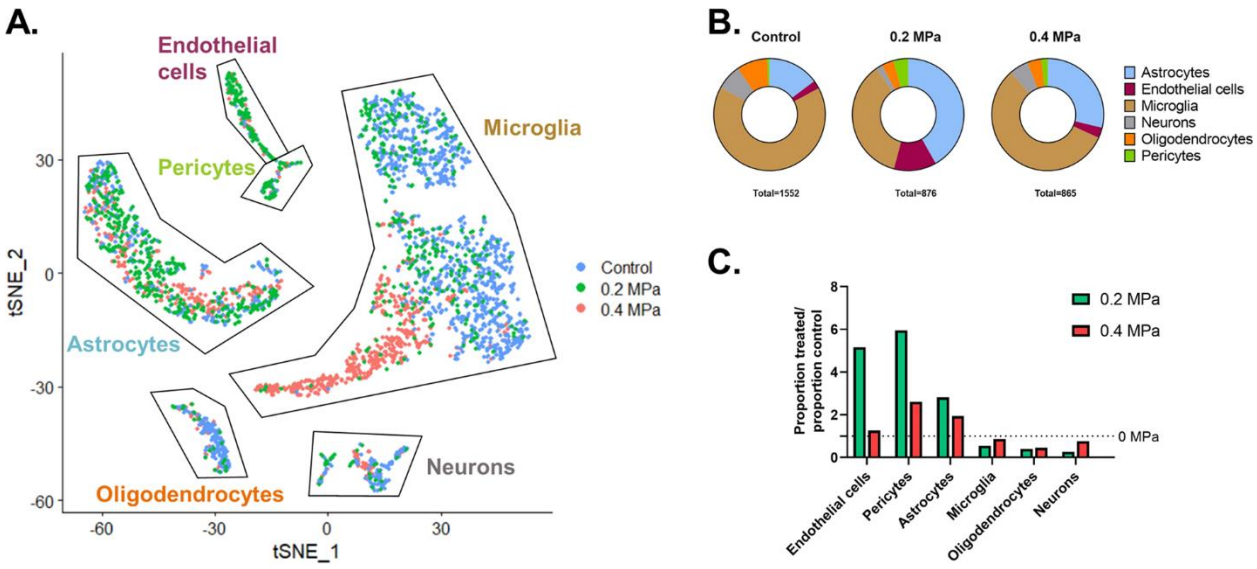

Figure 4.2. Identification of FUS-transfected cell types as a function of PNP. A) t-SNE plot showing all sequenced cells, colored according to their treatment condition. Labels on graph indicate cell populations identified by graph-based clustering followed by analysis of globally distinguishing transcripts within each cluster. B) Proportions of each of the 6 identified cell types for each condition. Total numbers of cells analyzed are shown below each chart. C) Bar graph illustrating the influence of FUS PNP on the distribution of transfected cells.

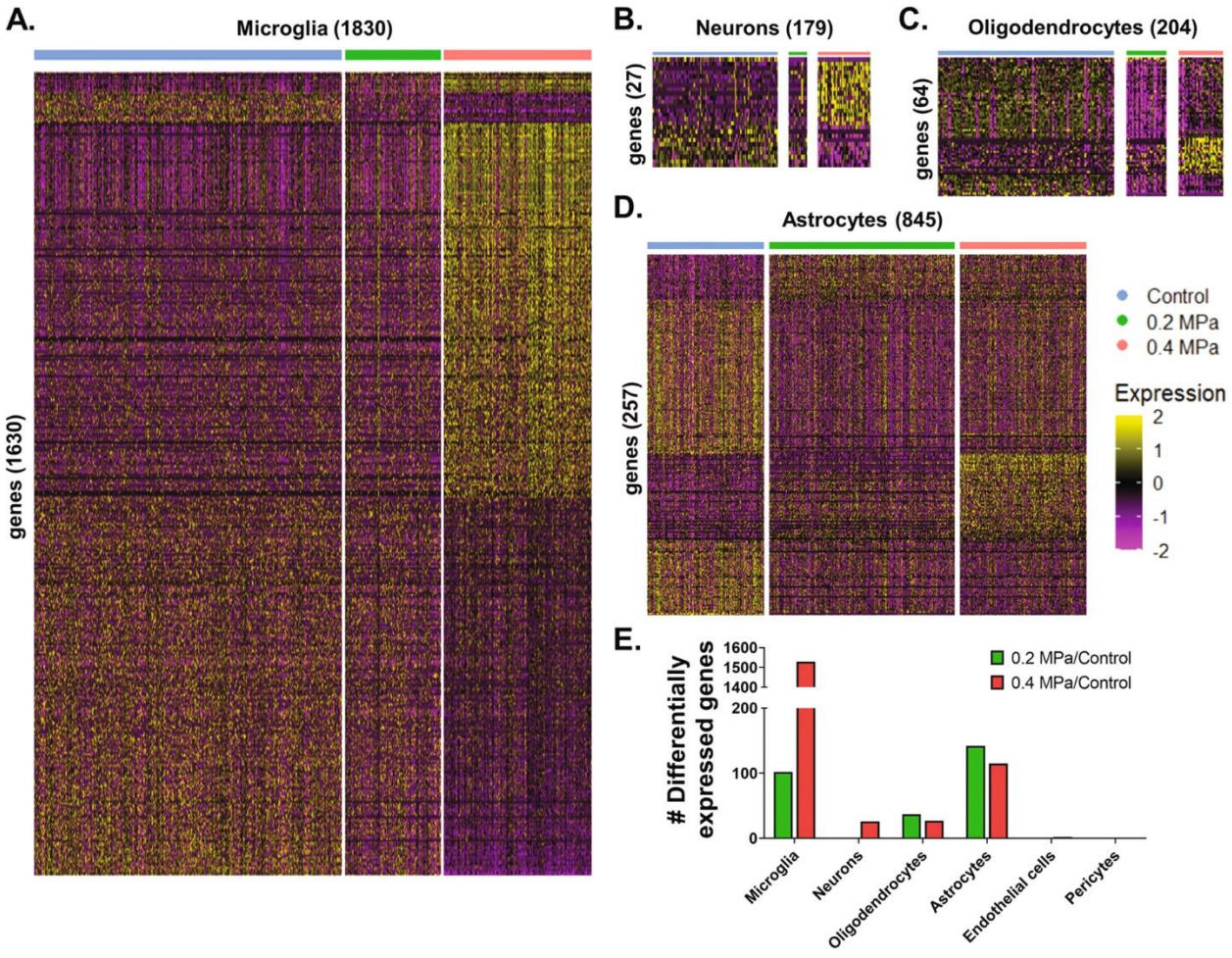

Figure 4.3. Transcriptional responses of individual focused ultrasound-transfected cells. A-D) Gene expression heatmaps for (A) microglia, (B) neurons, (C) oligodendrocytes, and (D) astrocytes. Each column represents a single cell and each row represents a gene of interest. Selected genes for each cell type are significantly (p-adjusted < 0.05) upregulated or downregulated at 0.2 MPa or 0.4 MPa compared to control. Expression levels are presented as row-normalized z-scores according to the key. Numbers in parenthesis indicate total number of cells (columns) or genes (rows) presented. E) Magnitude of significant (p adjusted < 0.05) differential gene expression (upregulated + downregulated) for each cell type at each pressure vs control cells.

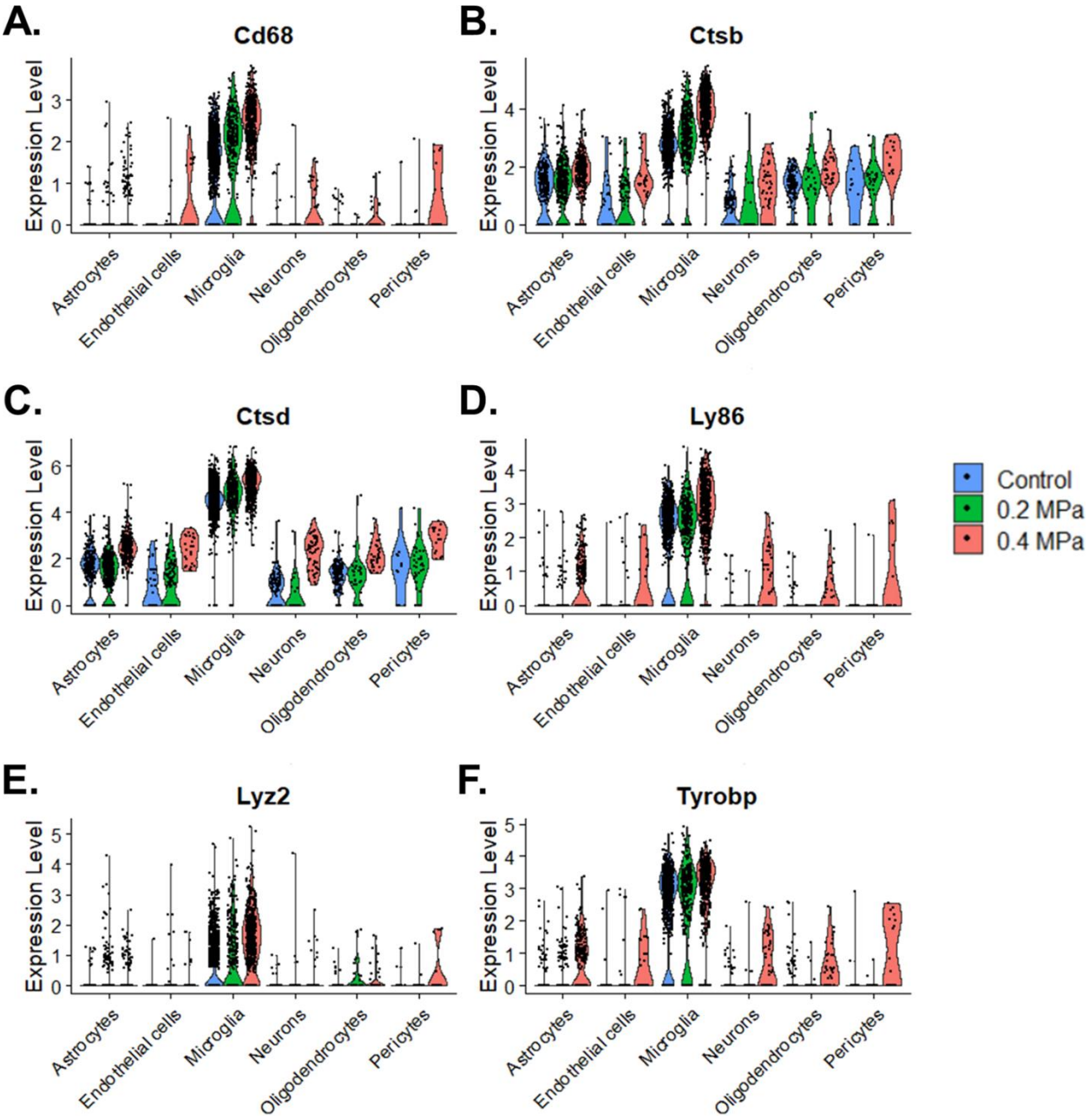

Figure 4.4. Genes associated with cell stress are upregulated across multiple cell types as a function of FUS PNP. A-F) Violin plots of normalized expression levels for selected transcripts. Each dot represents a single cell, grouped by cell type and treatment condition.

4.7 Chapter 4 Supplemental Figures

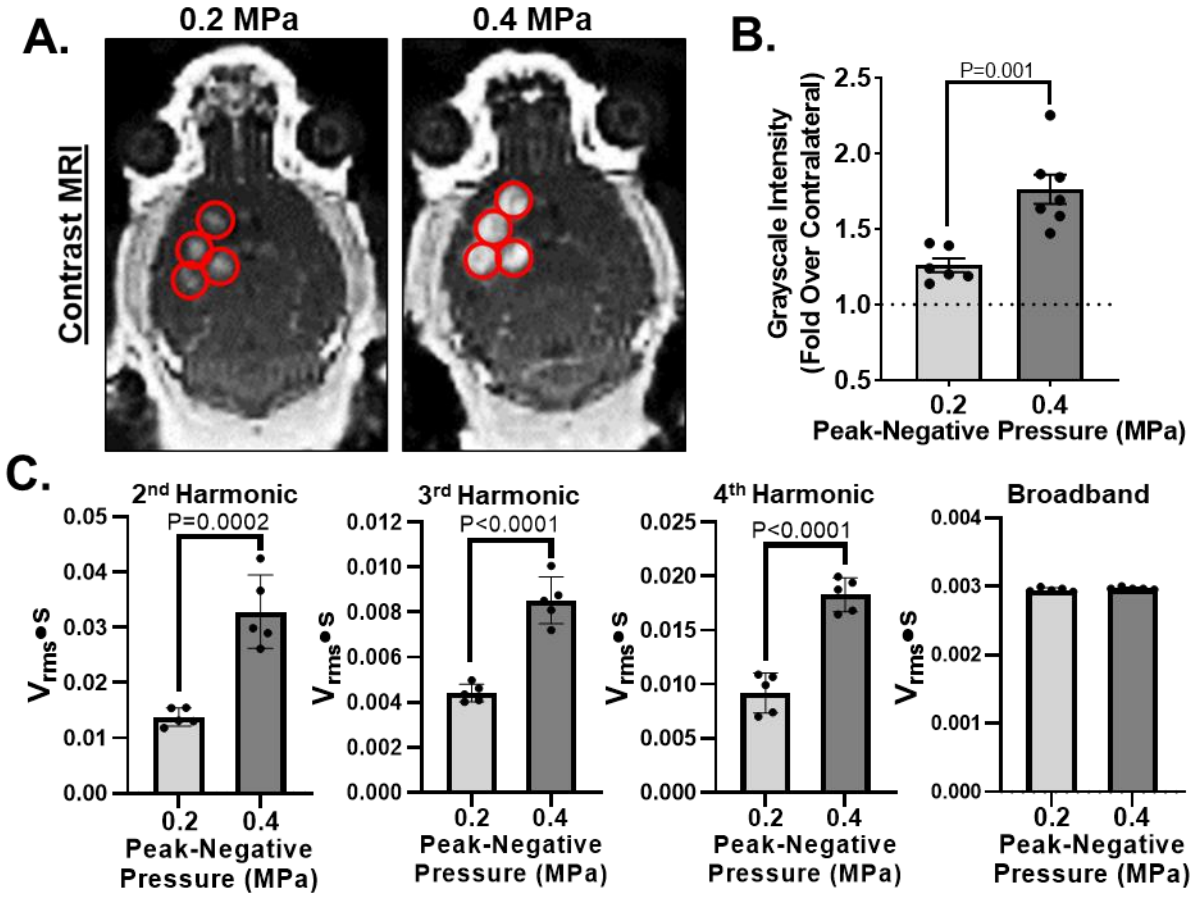

Figure 4.S1. Characterization of blood-brain barrier opening with focused ultrasound. A) Contrast MR images of mouse brains after application of pulsed FUS in the presence of systemically administered MBs. FUS was applied at peak-negative pressures of 0.2 and 0.4 MPa, with a 4-spot sonication pattern. Sonication sights are denoted with red circles. B) Bar graph of contrast enhancement over contralateral FUS^- control hemisphere as a function of pressure. C) Passive cavitation analyses for 2^{nd}, 3^{rd}, and 4^{th} harmonics, as well as broadband emissions. All statistical comparisons by unpaired t-tests.

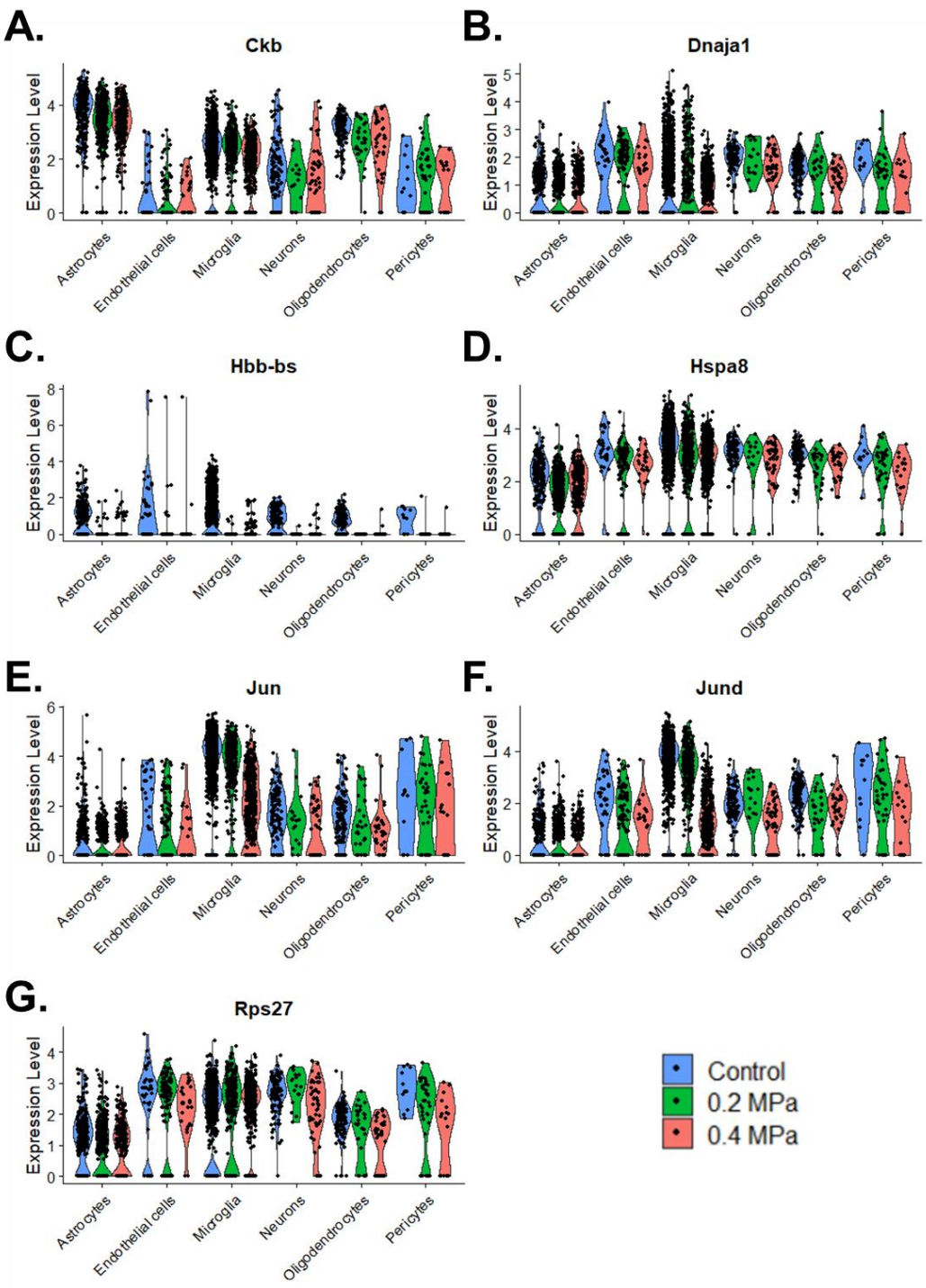

Figure 4.S2. Genes downregulated across multiple cell types as a function of FUS PNP. A-G) Violin plots of normalized expression levels for selected transcripts. Each dot represents a single cell, grouped by cell type and treatment condition.

A.

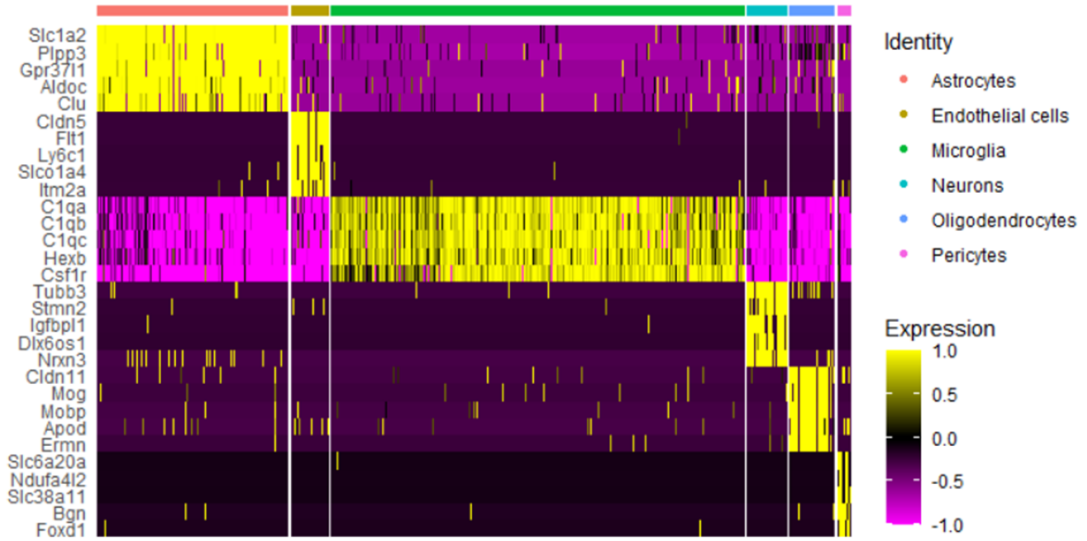

B.

Rank	Astrocytes	Endothelial cells	Microglia	Neurons	Oligodendrocytes	Pericytes
1	Slc1a2	Cldn5	C1qa	Tubb3	Cldn11	Slc6a20a
2	Plpp3	Flt1	C1qb	Stmn2	Mog	Ndufa4l2
3	Gpr37l1	Ly6c1	C1qc	Igfbpl1	Mobp	Slc38a11
4	Aldoc	Slco1a4	Hexb	Dlx6os1	Apod	Bgn
5	Clu	Itm2a	Csf1r	Nrxn3	Ermn	Foxd1
6	Atp1a2	Pltp	Ctss	Dcx	Enpp2	Mir143hg
7	Gja1	Ly6a	Ctsd	Dpysl3	Tspan2	Tbx18
8	Bcan	Spock2	Atf3	Stmn3	Stmn4	Ogn
9	Slc4a4	Cxcl12	Selplg	Dlx1	Opalin	Vtn
10	Mt3	Ptprb	Cx3cr1	Celf4	Ppp1r14a	Enpep
11	Htra1	Egfl7	Tmem119	Cd24a	Tubb4a	Pcolce
12	Cspg5	Abcb1a	Fcrls	Gad2	Ugt8a	Col3a1
13	Ttyh1	Igfbp7	Lgmn	6330403K07Rik	Pllp	Gpc3
14	Nrxn1	9430020K01Rik	Trem2	Bcl11a	Grb14	S1pr3
15	Sparcl1	Pglyrp1	P2ry12	Nsg1	Aspa	Ace2
16	Fjx1	Adgrf5	Tyrobp	Gad1	Sez6l2	Kcnj8
17	Ptprz1	Fn1	Junb	Sp9	Tmem151a	Higd1b
18	Slc6a11	Pcp4l1	Fcer1g	Bex2	Tmeff2	Twist1
19	Ndrg2	Adgrl4	Mafb	Dlx2	Edil3	Abcc9
20	Ntsr2	Sema3c	Laptm5	Nsg2	Efnb3	Aspn

Figure 4.S3. Globally distinguishing transcripts used to assign cell-types to clusters. A) Gene expression heatmap showing the top 5 globally distinguishing genes from each cluster. Each row represents a single gene and each column represents a single cell, with each element of the heatmap representing a row-normalized expression value. Cluster membership is represented by the bars above the heatmap. B) The top 20 globally distinguishing transcripts from each cell cluster were compared against the PangloDB webserver[4] to assign cell type. Globally distinguishing transcripts were defined as very significantly (p adjusted < 1E-240), upregulated (average natural log fold change above all other cell types > 0.25), and expressed in at least 25% of that cell type.

4.8 Chapter 4 Supplemental Tables

Microglia						**Astrocytes**					
0.2 MPa			**0.4 MPa**			**0.2 MPa**			**0.4 MPa**		
symbol	**avg_logFC**	**p_val_adj**	**symbol**	**avg_logFC**	**p_val_adj**	**symbol**	**avg_logFC**	**p_val_adj**	**symbol**	**avg_logFC**	**p_val_adj**
Hbb-bs	-1.7106704	1.10E-115	Jund	-2.12966211	3.26E-294	Hbb-bs	-1.29153602	1.15E-66	Hbb-bs	-1.16972319	9.85E-41
Hba-a1	-0.89951604	2.79E-36	Ctsb	1.27546198	1.80E-206	Hba-a2	-0.46252228	9.26E-23	Tmsb4x	0.76890122	1.05E-33
Cd81	-0.47836238	3.75E-33	Selplg	-1.1130985	1.27E-204	Hba-a1	-0.62888017	4.37E-22	Ctsd	0.85006323	1.70E-33
Hba-a2	-0.74332008	1.59E-27	Ier5	-1.49685688	1.07E-203	Hbb-bt	-0.52542572	1.14E-15	Ly86	0.76467565	1.68E-24
Hbb-bt	-0.5925249	2.30E-21	Jun	-1.56760745	7.30E-189	PISD	0.49188835	3.20E-13	Tyrobp	0.81617834	5.14E-23
Tmem176b	-0.6174352	2.40E-20	Junb	-1.58459307	3.85E-187	Dbi	-0.68587095	2.21E-12	C1qb	0.70061823	1.80E-22
Cd83	-0.66123733	1.44E-19	Ubc	-1.36825621	2.34E-180	H3f3b	-0.61372328	9.65E-12	Ank2	0.4715101	5.25E-13
Tmem119	-0.4634066	1.48E-18	Rpsa	1.11805242	1.39E-158	Ubb	-0.60309423	1.08E-11	Fcrls	0.5707902	1.59E-12
Ctsb	0.57018413	4.58E-18	Csf1r	-0.95354205	4.43E-157	Eif1	-0.54712225	1.09E-10	Gria2	0.48559285	1.67E-12
Atf3	-0.5666306	4.15E-17	Rps2	1.14592479	9.34E-153	Fabp7	-1.40576028	2.92E-10	Lgmn	0.58716787	1.75E-12
C1qa	-0.28208189	6.83E-17	Rhob	-1.11435431	3.50E-151	Nkain4	-0.62169416	3.63E-08	Hexb	0.52641333	2.04E-12
C1qc	-0.26199382	1.29E-14	Atf3	-1.55530981	4.11E-144	Grin2c	0.56944976	5.96E-08	Ubb	-0.6287844	1.83E-11
Selplg	-0.28300175	6.99E-13	Rps19	1.15345191	8.22E-143	Mpc1	-0.54014168	8.81E-08	Mt3	-0.69684725	2.00E-11
Ier5	-0.42126815	3.13E-12	Prdx1	1.25606692	1.23E-141	Hspa8	-0.46400036	9.88E-08	C1qa	0.54858542	2.31E-11
Ier2	-0.63172618	5.31E-12	Unc93b1	-0.94088107	4.16E-140	Cd9	-0.6097746	1.33E-07	Macf1	0.28370792	1.03E-09
Ubc	-0.38702291	5.32E-12	Btg2	-1.50503967	6.74E-139	Ppia	-0.48094134	2.13E-07	mt-Nd4l	0.4583164	1.24E-09
Rpl35	0.41977276	8.88E-12	Tmem119	-1.06037989	1.03E-138	Mertk	0.51127802	2.37E-07	Ctsb	0.45341917	1.47E-09
Tmem176a	-0.5731051	1.01E-11	Rpl32	1.17058763	4.38E-137	Vcl	0.463661	2.44E-07	Hba-a1	-0.55144011	1.55E-09
Cd68	0.35321071	4.34E-11	Rps20	1.10234054	2.25E-136	Prdx1	-0.52152968	5.63E-07	Grin2c	0.57839114	1.62E-09
Junb	-0.39761693	1.12E-10	Cd83	-1.65294619	5.76E-136	Prodh	0.46056433	5.69E-07	Mt2	-0.64971016	1.98E-09
C1qb	-0.26205448	1.14E-10	Mif	1.3893888	9.98E-135	Nrxn1	0.28030098	7.73E-07	C1qc	0.5328327	2.69E-09
Jund	-0.34436837	1.53E-10	H3f3b	-1.21914785	1.89E-134	Fez1	-0.49848005	9.95E-07	Hbb-bt	-0.49419105	1.11E-08
Rps28	0.37702417	2.47E-10	Hbb-bs	-1.60912711	2.07E-128	Acsl3	0.33944266	1.12E-06	Ldhb	-0.57952084	1.36E-08
Rps26	0.37806447	4.25E-10	Lgals1	1.65736327	9.25E-127	Rpl8	-0.47429529	1.16E-06	Nrxn1	0.34905109	2.05E-08
Actg1	-0.45536277	4.39E-10	Rpl14	1.00307058	1.68E-121	Chchd2	-0.45919547	1.16E-06	Nkain4	-0.69984864	6.45E-08
Oligodendrocytes						**Neurons**					
0.2 MPa			**0.4 MPa**			**0.2 MPa**			**0.4 MPa**		
symbol	**avg_logFC**	**p_val_adj**	**symbol**	**avg_logFC**	**p_val_adj**	**symbol**	**avg_logFC**	**p_val_adj**	**symbol**	**avg_logFC**	**p_val_adj**
Hbb-bs	-0.88213465	1.38E-13	Hbb-bs	-0.78490253	8.36E-11	Hbb-bs	-0.97678324	3.80E-03	Ctsd	1.49075697	3.44E-19
Trf	-0.91572771	7.59E-08	Ctsd	0.86076288	4.60E-09				Hbb-bs	-0.81298249	7.19E-08
PISD	1.89894975	5.33E-07	C4b	1.72161692	7.53E-09				Ly86	1.01968072	8.03E-08
Ubb	-0.54504629	2.68E-05	Serpina3n	1.39453378	8.68E-09				Cst3	0.66972402	3.81E-07
Fth1	-0.76783415	4.18E-05	Endod1	0.66454782	6.14E-08				Gm42418	0.89058893	2.18E-06
Slc48a1	-0.78395	5.90E-05	Plekha1	0.99470796	1.42E-06				C1qa	0.82210151	3.12E-05
Stmn4	-0.79281369	1.39E-04	Ubb	-0.41770552	1.81E-05				Actg1	-0.82547073	7.40E-05
Car2	-0.96981599	5.52E-04	Gstm5	-0.7261072	9.19E-05				C1qb	0.87732951	9.95E-05
Qdpr	-0.85502048	6.70E-04	Fabp5	1.21698285	3.40E-04				Lgmn	0.75816036	6.95E-04
Ptma	-0.60691154	9.50E-04	Mat2a	0.60974994	3.95E-04				Gnb1	-0.36605323	1.17E-03
Gatm	-0.72128819	9.75E-04	Ank3	0.77488641	4.36E-04				Tyrobp	0.82393792	2.51E-03
Sec11c	-0.73059016	1.31E-03	Stmn4	-0.59369992	4.53E-04				Ptms	-0.56245225	4.96E-03
Csrp1	-0.92714479	1.41E-03	Egr1	-1.06425312	2.16E-03				Ube3c	0.61336503	5.61E-03
Cryab	-0.80488817	2.47E-03	Csrp1	-0.60759123	3.53E-03				Fcrls	0.77190779	7.48E-03
Hsp90aa1	-0.54641709	3.64E-03	Dlk2	0.3323742	3.57E-03				Hbb-bt	-0.3427697	7.90E-03
Sez6l2	-0.66418779	4.20E-03	Tubb3	0.90953719	5.58E-03				mt-Co1	0.65613358	8.02E-03
Itm2b	-0.40977639	4.88E-03	Tulp4	0.58597021	6.78E-03				Jund	-0.66011931	9.10E-03
Cox4i1	-0.50577426	5.67E-03	Slc9a3r2	0.6952904	9.37E-03				Trpm7	0.97176787	1.01E-02
Igsf8	0.4524799	8.36E-03	Fez1	-0.50518529	1.27E-02				Ctsb	0.7690223	1.54E-02
Psmb7	-0.55280556	9.88E-03	Rps27	-0.53595975	1.55E-02				2610524H06R	-0.38794939	1.97E-02
Jund	-0.64035694	1.05E-02	Fcrls	0.58202078	2.30E-02				Dynll1	-0.54678969	2.53E-02
Efhd1	-0.57352124	1.18E-02	Cd63	0.97580669	2.30E-02				Cct8	-0.29753548	2.58E-02
Rabac1	-0.48352384	1.26E-02	Gadd45b	1.35715649	3.15E-02				6330403K07R	-0.46821657	3.01E-02
Eif1	-0.49575777	1.31E-02	Clock	0.53064675	3.30E-02				Gnai2	-0.70361002	3.04E-02
H3f3b	-0.50576516	1.66E-02	Actb	-0.42862232	3.98E-02				Cep350	0.47164902	3.44E-02
Endothelial cells						**Pericytes**					
0.2 MPa			**0.4 MPa**			**0.2 MPa**			**0.4 MPa**		
symbol	**avg_logFC**	**p_val_adj**	**symbol**	**avg_logFC**	**p_val_adj**	**symbol**	**avg_logFC**	**p_val_adj**	**symbol**	**avg_logFC**	**p_val_adj**
Hbb-bs	-1.78511506	6.41E-05	Ctsd	1.3041957	1.56E-04	N/A	N/A	N/A	N/A	N/A	N/A
			Fcrls	0.90358352	1.60E-02						

Table 4.S1: Top 25 most significantly differentially expressed genes at 0.2 MPa and 0.4 MPa compared to control for each cell type.

Chapter 5: Computational Model of Brain Endothelial Cell Signaling Predicts Drug Targets for Cerebral Pathologies

Catherine M. Gorick, Jeffrey J. Saucerman, and Richard J. Price

5.1 Abstract

The endothelial cells of the brain serve many important functions, including comprising the blood-brain barrier (BBB) and regulating blood flow, nutrient exchange, drug efflux, and maintaining cerebral homeostasis. Although many signaling pathways in brain endothelial cells have been implicated in disease, optimal molecular targets for endothelial cell-based drug or gene therapy can be difficult to determine. To address this need, we developed a large-scale computational model of brain endothelial cell signaling, capable of identifying the most influential molecules for pharmaceutical targeting to promote therapeutic changes in the endothelial cell phenotype. Briefly, brain endothelial cell signaling pathways were reconstructed from the literature and converted into a network of logic-based differential equations. The model integrates 63 nodes (including proteins, mRNA, small molecules, and cell phenotypes) and 82 reactions connecting these nodes. To validate the model, independently established relationships between selected inputs and outputs were simulated, with the model yielding correct predictions 73% of the time. Using the model, we identified influential and sensitive nodes under different physiological or pathological contexts. These included altered brain endothelial cell conditions during glioma, Alzheimer's disease, and ischemic stroke. We can then identify nodes with the greatest influence over combinations of desired model outputs as potential druggable targets for these disease conditions. For example, the model predicts therapeutic benefits from inhibiting AKT, Hif-1α, or cathepsin D in the context of glioma – each of which are currently being studied in clinical and pre-clinical trials. The model also permits testing multiple combinations of node alterations for their effects on the network and the desired outputs (such as inhibiting AKT and overexpressing the P75 neurotrophin receptor simultaneously in the context of glioma), allowing for the prediction of optimal combination therapies.

5.2 Introduction

Many pathologies of the brain are characterized by both devastating daily effects for patients and daunting challenges and limitations to treatment for physicians(256). These conditions, which include brain tumors, neurodegenerative diseases, and stroke, vary widely in their incidence, molecular mechanisms, and progression, and yet all remain inherently difficult to treat. At least some of the challenge of treatment rests in the nature of the brain structure itself, and more specifically, the blood-brain barrier (BBB). For many years, delivery of therapeutics to the brain required risky and invasive surgery to facilitate direct injections(18, 25, 29, 30), or brain-wide disruption of the BBB to allow passage of drugs(37, 38). More recently, focused ultrasound (FUS) in conjunction with intravenously-injected gas-filled microbubbles has been used to transiently disrupt the BBB in a targeted manner. This approach can be used to deliver genes or other therapeutics to a specific structure or region of the brain non-invasively(123, 145, 257, 258).

The primary physiological basis of the BBB is the continuous, non-fenestrated layer of brain capillary endothelial cells which line the cerebral microvasculature. Brain endothelial cells are held together by tight junctions, which serve as a barrier to paracellular passive diffusion of materials from the systemic circulation into the surrounding brain tissue(13). The brain endothelium also expresses drug efflux pumps, such as p-glycoprotein, to continuously remove potentially harmful materials from the CNS(15). Thus, in essence, brain endothelial cells are the gatekeepers to the brain – the only mechanisms by which molecules can reach the brain are through the endothelial cells themselves. As the gatekeepers, cerebral endothelial cells play a tremendous role in the state of the brain in both physiological and pathological conditions, by dictating the blood flow, oxygenation, nutrient transport, and drug concentrations in the brain parenchyma. Identifying the key drivers and regulators of the expression of certain junctional

proteins or transporters in these cells could be extremely useful in selecting drug targets for diseases of the central nervous system.

Brain endothelial cells experience competing cues from growth factors, neurotrophic factors, and other cytokines and paracrine signaling molecules, and integrate these diverse signals to regulate behaviors such as angiogenesis, immune cell recruitment, and apoptosis. Therefore, appropriate therapeutic strategies to modulate cerebral endothelial cell signaling must function within this complex environment of diverse signaling cues present in the healthy or diseased brain. Designing such therapies relies on understanding how cells integrate these signals, yet to date no large-scale computational models of brain endothelial cell signaling exist.

In this study we develop the first large-scale computational model of the brain endothelial cell signaling network in order to identify disease context-dependent drivers of therapeutic patterns of molecule expression or phenotypes. The model incorporates the VEGF-A signaling pathway, the BDNF and NGF neurotrophin signaling pathways, and the Wnt signaling pathway. BDNF and NGF can act through either their unprocessed, pro-neurotrophin forms, which preferentially bind sortilin and the $p75^{NTR}$ receptor to activate a number of pro-apoptotic pathways, or can be processed by protein convertases such as furin or plasmin into their mature neurotrophin forms, which preferentially bind the Trk receptors and induce more pro-survival signaling(259). VEGF-A signaling drives many pro-angiogenic processes(260), and Wnt signaling in the brain endothelium has been implicated in promoting survival and BBB integrity(261). Additionally, our model features a FUS input node, based upon prior in vivo transcriptomic studies which demonstrated that FUS-mediated BBB opening results in upregulation of cathepsin D in cerebral endothelial cells(262). The model's outputs were selected for their relevance to brain pathologies of interest. These include the proteins which constitute tight junctions, claudin-5 and occludin, and adherens junctions, VE cadherin, between endothelial cells. Outputs also include expression of the glucose transporter GLUT1 and the

efflux transporter p-glycoprotein, as well as nitric oxide production (which helps regulate vasodilation and blood flow), and apoptosis or cell death.

After validating the model at baseline (“normal” physiological conditions) against the existing literature, we simulate the altered signaling network under three disease states (glioma, Alzheimer’s disease, and ischemic stroke) and predict the most influential nodes in regulating potential therapeutic responses to those specific pathologies. This analysis reveals novel potential targets (or combinations of targets) for pharmaceutical intervention using FUS as a delivery mechanism. We submit that this model represents a valuable tool to develop strategic therapeutic approaches for FUS-mediated drug and gene delivery in a range of different disease contexts in the brain.

5.3 Results

5.3.1 A predictive computational model of brain endothelial cell signaling

A predictive computational model of brain endothelial cell signaling was manually reconstructed from previous experimental studies from the literature. Literature papers on endothelial cell signaling were placed into “model development” or “model validation” groups, based on whether the paper described direct molecular interactions or network input-output relationships. The structure of the endothelial cell signaling network came from the “model development” literature, which identified 101 reactions or interactions in the network. The 26 papers in the “model validation” literature group were used to validate the model predictions of network-wide function. The detailed procedure for literature review and network reconstruction is provided in the Materials and Methods section.

This brain endothelial cell signaling network (Figure 5.1) integrates a number of signaling pathways previously shown to impact key brain endothelial cell phenotypes and undergo alterations in one or more brain pathologies of interest. The signaling pathways include VEGF-A signaling, BDNF and NGF signaling, Wnt signaling, and FUS-mediated signaling. In order to represent the effects of focused ultrasound-mediated microbubble activation and blood-brain barrier disruption, we included a FUS input node. In prior in vivo studies, single cell transcriptomic analyses of brain tissue following FUS treatment revealed that cathepsin D was significantly upregulated in brain endothelial cells after FUS(262). Therefore, a FUS node was added as an input to the model, which would directly activate cathepsin D, to simulate the effects of FUS treatment. In total, the network includes 63 nodes (mRNA, proteins, small molecules, cell processes, and FUS) connected by 82 reactions. The species list is provided in Table 5.1 and full documentation of each reaction and the experimental evidence supporting that reaction is provided in Table 5.2.

The network reconstruction was then converted into a predictive computational model using a logic-based ordinary differential equation approach (263, 264). Briefly, the normalized activity of each node is modeled using ordinary differential equations, with reactions modeled using saturating Hill functions and continuous OR/AND logic gates to represent pathway crosstalk. In general, OR gating is used when each input to a node is sufficient but not necessary for activation, whereas AND gating is used when each input is necessary. As in previous network models of this style, uniform default values were used for all network parameters. The baseline condition was defined as 40% signaling activity for all inputs with the exception of the FUS input node, which was kept at 0% activity at baseline (and increased to 40% activity when “on” in the disease therapy contexts described later). The 40% value, which is within the range of prior studies using this computational approach(263–266), was selected to maximize network activation while maintaining a low baseline rate of cell death/apoptosis (below 20% under “normal” physiological conditions). Based on the network structure in Table 5.2, the system of ODEs was automatically generated in Netflux and implemented in MATLAB, as detailed in the Materials and Methods section.

Next, we predicted responses of the endothelial cell signaling network to specific stimuli, and validated these predictions against experimental studies performed in endothelial cells that were independent from those studies used to reconstruct the signaling network. For example, the effect of different concentrations of Wnt or a Wnt agonist on the activity of P-glycoprotein was simulated and compared to experimental data from Lim et al.(267) (Figure 5.2). The model predicts a dose-dependent increase in P-glycoprotein activity as Wnt inputs are increased, qualitatively consistent with published data from human brain endothelial cells showing that Wnt/β catenin signaling positively regulates P-glycoprotein expression and activity.

Overall, the model was validated against 26 input-output relationships for which experimental data is available, and accurately predicts 19 of those 26 (73%). Of the

relationships for which there is disagreement, 3 of these are partial disagreements (either the model or literature claims no change in activity, and the other predicts a change) and 4 are complete disagreements (the model and literature predict activity changes in opposite directions). Figure 5.3 summarizes the predicted relationship of the different individual input stimuli to each of the outputs, and the agreement between model predictions and experimental data where available (26 relationships). The literature sources of the experimental data used to validate the model can be found in Table 5.3.

5.3.2 Identification of key network regulators

After validating the model's predictive capability, we performed a network-wide sensitivity analysis in order to determine quantitative functional relationships across the network. Knockdown of individual nodes was simulated by reducing the Y_{max} value for that node. The resulting change in activity of each other node was then measured, predicting the response of the network to inhibition of specific receptors, kinases, or genes. "Influential" nodes were defined as those whose knockdown causes the greatest activity changes across the network, as measured by the number of nodes whose activity was altered by at least 20% in response to the knockdown. Based on the network-wide sensitivity analysis (Figure 5.4), we identified the 4 nodes with the greatest influence over the rest of the network (Figure 5.5A). These most influential nodes were AKT, cathepsin D, VEGF-A, and VEGFR2. As the VEGF-A signaling pathway activates a number of different complex pathways, the presence of VEGF-A and VEGFR2 are perhaps not surprising here. AKT is a well-connected central hub in the network activating a number of downstream cascades, and cathepsin D directly activates both AKT and ERK. "Sensitive" nodes were defined as those with significant activity changes (at least 20%) in response to the most different knockdowns. The top 4 sensitive nodes (Figure 5.5B) were occludin, IP3, DAG, and GLUT1. IP3 and DAG are both involved in calcium signaling

downstream of VEGF-A, NGF, and BDNF pathways, while occludin and GLUT1 are terminal outputs controlled by the activation of these pathways as well. We also identified the impact of each node knockout on each of the outputs of interest: VE cadherin, claudin-5, occludin, cell death, GLUT1, P-glycoprotein, and nitric oxide activity. The sensitivity of these outputs to systematic node knockout under baseline conditions can be seen in Figure 5.S1.

5.3.3 Identification of therapeutic targets within signaling network

In order to utilize the brain endothelial cell signaling network model to identify druggable targets for pathologies of the brain, we first reviewed the literature to determine the relative expression levels of a number of our model inputs (VEGF-A, NGF, BDNF, Wnt, and cathepsin D) in each of three disease states: glioma, Alzheimer's disease, and ischemic stroke (see Table 5.4 for references). In the context of glioma, all five of these inputs have been demonstrated to be present at a higher level than healthy brain tissue. In Alzheimer's disease, NGF and BDNF activity is characterized by a shift towards the pro-neurotrophin forms of each protein (which binds sortilin and $p75^{NTR}$), as opposed to the mature forms (which are cleaved by pro-convertases like plasmin or MMP and bind the TrkA or TrkB receptors). The brains of Alzheimer's disease patients also display reduced levels of VEGF-A, Wnt, and cathepsin D. Finally, in the infarcted regions of brains affected by ischemic stroke, reductions in the levels of BDNF and cathepsin D have been observed, as have increases in the concentrations of VEGF-A and Wnt. The differential expression of these inputs can be used to create a disease context in which to identify and test potential therapies. Briefly, any input which is elevated in the disease state relative to control was increased by 25% (from 0.4 to 0.65), and any input which is reduced was decreased by 25% (from 0.4 to 0.15). While the range of changes in concentrations of these molecules varied widely in the literature, the 25% change in either direction was selected to avoid under- or over-saturating any input nodes while still producing a

significant range of possible values for each input. In each of the disease contexts, we added the FUS input to simulate the delivery mechanism of therapeutics (at the standard input weight of 0.4).

We also reviewed the literature to identify therapeutic goals for each of these pathologies that are currently being investigated. We discovered general treatment aims that aligned with increased or decreased activity of a number of our model outputs (Table 5.5). Glioma, for example, is characterized by poorly controlled cell division and excessive efflux of chemotherapeutics through the P-glycoprotein efflux pump. For these reasons, we identified the therapeutic goals for glioma of increasing cell death, reducing GLUT1 activity (and subsequent glucose supply to the tumor), and reducing P-glycoprotein activity. In Alzheimer's disease, a leaky BBB is often associated with worse symptom progression, and there is often insufficient nutrient transport and efflux along the affected endothelium. For this pathology, the therapeutic goals were to increase VE cadherin, claudin-5, occludin, GLUT1, and P-glycoprotein. The BBB is also disrupted following ischemic stroke, which is also characterized by increased apoptosis. For stroke, we sought to increase VE cadherin, claudin-5, and occludin, while decreasing cell death. Additionally, we found that nitric oxide upregulation is being investigated to promote increased blood flow in infarcted brain tissue, so we included nitric oxide increase as a treatment goal.

After simulating a given disease state through the altered input values, we repeated our systematic sensitivity analysis by knocking out or over-activating each node by changing the value of Y_{max} (to 0 or 2, respectively) and measuring the impact on each other node in the system (Figures 5.S2, 5.S3, 5.S4). We then evaluated the impact of each of these knockdowns or over-expressions on the treatment score for the disease state of interest. For example, the glioma therapeutic score was computed by taking a node alteration's effect on cell death (a positive increase being beneficial in this case, as we want to increase cell death in the context

of glioma), and subtracting the alteration's effect on GLUT1 expression and P-glycoprotein expression (both of which we want to decrease in this pathology). We identified the top 3-5 nodes from both the knockdown and overexpression cases in terms of their therapeutic index for that disease state. These nodes were further investigated for their specific impacts on each of the individual outputs contributing to the therapeutic index. This workflow was repeated for the glioma (Figure 5.6), Alzheimer's (Figure 5.7), and stroke (Figure 5.8) disease states. Lastly, one of the top nodes from the knockdown case and one from the overexpression case were considered together for a "combinatorial" drug approach to identify potentially synergistic pairings (Figure 5.S5).

Among the top targets for knockdown in the context of glioma were GLUT1 and P-glycoprotein, which was unsurprising given that they were two of the three metrics for the glioma therapeutic score. Additional top targets included AKT, Hif-1α, and cathepsin D, all of which are currently under investigation as therapeutic targets for glioma in pre-clinical studies(268–270). The top targets for upregulation or overexpression were all related pro-apoptotic signaling, as a result of the inclusion of increased cell death as a treatment goal. In the Alzheimer's disease context, many of the top targets for over-expression were the individual outputs included in the therapeutic goals, so this was not a particularly novel finding. The most influential nodes for knockdown included MMP, which is involved in the breakdown of three of the therapeutic outputs (VE cadherin, claudin-5, and occludin), as well as NFκB and GSK3β. Lastly, in the context of ischemic stroke, prime targets for knockdown included MMP and components of the VEGF signaling pathway (which decreases BBB integrity). Overexpression candidates included some of the treatment goal outputs themselves, as well as ERK and KLF4, both of which increase VE-cadherin expression and reduce apoptosis.

5.4 Discussion

Here we manually reconstructed a literature-based network of brain endothelial cell signaling that identifies the nodes regulating the expression of BBB tight junctional and adherens junctional proteins, GLUT1, and the P-glycoprotein efflux receptor, as well as nitric oxide release and apoptosis. This network was used to develop a logic-based predictive model of endothelial cell signaling (with or without FUS treatment), which validated at a rate of 73% in comparison to independent, published studies in endothelial cells. This agreement rate is similar to other published models utilizing this logic-based differential equation approach(263, 264). This is, to our knowledge, the first large-scale computational model of brain endothelial cell signaling. A comprehensive sensitivity analysis identified the network's most sensitive and influential nodes. Three unique disease states (glioma, Alzheimer's disease, and ischemic stroke) were simulated based on characteristic patterns of model inputs, and the model was then used to predict the most therapeutically beneficial nodes to inhibit or over-express for each pathology. Additionally, the model can predict the combinatorial effect of testing multiple drug targets at once. Our approach integrates results from over 100 past studies into a coherent model, revealing network interactions unapparent from studying any one pathway in isolation.

5.4.1 Model Validation

While the model correctly validates 73% of the input-output relationships for which there is independent data, 7 input-output relationships were incorrectly predicted by the model. Three of these were related to the Wnt input. The model predicted no change in cell death or GLUT1 expression, while the literature reports responses of these outputs to Wnt delivery. This suggests that the Wnt pathway as it currently stands in the model is incomplete. In future studies, we will attempt to better characterize this pathway and its cross-talk with the rest of the model, as well as expand upon its downstream branches to better capture some of these

behaviors. Additionally, 2 of the 6 relationships related to the FUS input node were in contradiction with the literature. The model predicted increases in P-glycoprotein and GLUT1 expression following FUS treatment, while the literature reported decreases. This is likely a function of our over-simplification of FUS as a node which activates only cathepsin D, when in reality FUS is likely to have many complex effects on endothelial cells and their environment. The transcriptomic data from which we determined the FUS activation of cathepsin D was collected at 48 hours after FUS treatment. Data from a more acute timepoint could provide a more detailed summary of the varied effects of FUS on brain endothelial cell activity. This, too, is an area for future improvement, likely through additional in vivo and in vitro studies (both identified in the literature and conducted in-house) to better characterize protein-level changes in network components following FUS-mediated BBB disruption at both acute and chronic timepoints.

5.4.2 Novel Computational Simulation of Brain Endothelial Cell Signaling and the Role of Focused Ultrasound

The model developed here is, to our knowledge, the first large-scale computational model of brain endothelial cell signaling. While there are numerous models investigating how mechanical and chemical cues regulate the dynamics of vascular endothelial cell sprouting and angiogenesis(271–274), signaling network models were less common. We were able to identify a computational model of angiopoietin and Tie signaling in systemic vascular endothelial cells(275), as well as a Boolean network model of endothelial-to-mesenchymal transition(276). However, no studies could be identified at this point which specifically model signaling activity in the endothelial cells of the brain. As these cells play a unique role among endothelial cells due to their function as the basis of the BBB and the gatekeepers to the central nervous system,

modeling these cells specifically is critically important for understanding how different CNS interventions will affect BBB integrity, nutrient transport, and other aspects of brain homeostasis.

Additionally, we are not aware of any other studies to date which incorporate FUS into a signaling network model. While FUS has now been used extensively to deliver therapeutics to the brain, and its systemic effects are under ongoing investigation, the specific impacts of FUS on endothelial cell signaling pathways remain insufficiently understood. While there have been some investigations into the impact of FUS on vascular gene expression(235) and protein activation(73, 277), there are currently no available models to simulate the combinatorial effects on the brain endothelium of FUS-mediated BBB disruption and simultaneous delivery of a therapeutic drug or gene. Our model is uniquely designed to incorporate the effects of FUS on brain endothelial cell signaling, so that unexpected impacts of FUS-mediated therapeutic delivery to the brain can be more accurately predicted and accounted for. This will improve the strategic design of FUS-mediated therapies moving forward.

5.4.3 Simulation of Disease States Allows Prediction of Druggable Targets

Upon simulation of brain disease states (glioma, Alzheimer's disease, or ischemic stroke) based on modulating the network inputs to reflect differential levels of those signaling molecules, we were able to compute the potential effects of node alterations (knockdown or overexpression) on the model outputs. In particular, we studied specific combinations of outputs for each disease state based on literature evidence for that output as a therapeutic goal for the pathology. In the context of glioma, where we sought to increase cell death while minimizing GLUT1 and p-glycoprotein activity, the model revealed that the best targets for inhibition were cathepsin D, Hif-1α, GLUT1, p-glycoprotein, and AKT. A review of the literature demonstrated that inhibition of each of these species is currently being studied to reduce glioma growth, in either clinical or pre-clinical trials(268–270, 278, 279). Our confidence in the model's ability to

identify therapeutically beneficial targets was strengthened by this finding. The fact that cathepsin D inhibition is indicated as a therapeutic target, while FUS-mediated BBB disruption increases cathepsin D activity, is also an important factor for consideration. It would be worth investigating whether a cathepsin D inhibitor is sufficient to overcome the activation induced by FUS, or whether an alternative delivery strategy (including a different modality of FUS, such as sonoselective transfection(123)) would be more appropriate in this context.

The model predicted a therapeutic benefit to inhibiting NFκB in the context of both Alzheimer's disease and ischemic stroke. Interestingly, endothelial-specific NFκB inhibition is currently being investigated as a treatment for a number of vascular pathologies outside of the brain, including atherosclerosis(280) and hypertension(281). While these conditions bear an obvious connection with ischemic stroke in terms of changes in blood flow, vascular stiffness, and inflammation, their similarities to Alzheimer's disease are perhaps less clear. However, as a critical regulator of immune and inflammatory responses(282), NFκB appears to represent an attractive target for inhibition wherever reducing inflammation is a therapeutic goal.

Importantly, the model allows for the predictive testing of not just a single potential node alteration, but combinatorial therapies as well. While such combination therapies were only briefly examined in the context of this study (Figure 5.S5), this approach allows for the high-throughput screening of many potential combinations of node inhibitions or overexpressions, representing protein antagonists or agonists/gene delivery. As evidenced by the disease simulations presented here, it is often difficult if not impossible to identify a single target which achieves all therapeutic goals. In the case of Alzheimer's and stroke, not even combinations of two node alterations could result in the desired alterations to all five treatment goals. This speaks to the tremendous complexity and widespread changes induced by these diseases, and accounts for the longstanding challenges in their treatment. It is clear that in the complex diseases that plague the brain and central nervous system, combination therapies will likely be

necessary to achieve multi-faceted symptom improvement or disease remission. These combination therapies may have a variety of unforeseen synergistic or destructive effects, reinforcing the need for large-scale signaling network models like the one presented here to predict outcomes in advance and logically design treatment combinations.

5.4.4 Limitations

As with all modeling approaches, there are inherent limitations to our computational approach. While the model uses all default parameters, refinement of the parameter weighting (with regard to reaction weighting as well as rate) as more quantitative proteomic data becomes available would increase model accuracy and predictive power. The model structure is not fully comprehensive, focusing instead on signaling pathways related to the cerebral pathologies of interest and with in vitro data that meets the specified inclusion criteria. To further enrich the model, future curation could incorporate additional paracrine signaling molecules released by astrocytes and pericytes, as well as pathways involved in the recruitment of immune cells and neural stem cells, which also play a major role in the altered signaling activity in various disease states. Our work also highlights gaps in the current understanding of brain endothelial cell signaling, particularly with regard to neurotrophin signaling (NGF, BDNF, etc) in BBB endothelial cells. In future studies, we plan to culture human and mouse brain endothelial cells in vitro and quantify transcript- and protein-level responses to pro-form and mature neurotrophin signaling.

5.5 Materials and Methods

5.5.1 Model Construction

A brain endothelial cell signaling network was manually reconstructed from previous in vitro and in vivo experimental studies from the published literature. The network integrates four key inputs of interest as potential gene/protein therapy targets for pathologies of the brain, primarily due to their role in angiogenesis, cell survival, or neural stem cell recruitment. These include NGF (nerve growth factor), BDNF (brain-derived neurotrophic factor), VEGF-A (vascular endothelial growth factor-A), and Wnt. Of these, NGF and BDNF can act in either or both of two forms – an immature, pro-neurotrophin (pro-NGF or pro-BDNF), or a mature, fully cleaved neurotrophin (mNGF and mBDNF). We also include an input to represent the effects of focused ultrasound-mediated microbubble activation and blood-brain barrier disruption, which we identified in prior in vivo studies. Briefly, single cell transcriptomic analyses of brain tissue following FUS treatment at different peak-negative pressures revealed a number of differentially regulated transcripts across cell types. One of these, cathepsin D, was significantly upregulated in brain endothelial cells following FUS treatment. In order to better predict the combinatorial effects of the FUS delivery mechanism and the gene or protein therapeutic of interest, a FUS node was added as an input to the model, which would directly activate cathepsin D, to simulate the effects of FUS treatment. Outputs were selected for their role in blood-brain barrier integrity (VE cadherin, claudin 5, and occludin), which has potential implications for sterile inflammatory responses, or for their relevance to the cerebral pathologies of interest (P-glycoprotein, glucose transporter 1, nitric oxide production, and cell death / apoptosis phenotype).

A review of existing literature on endothelial cell signaling was conducted, focusing primarily on the pathways impacted by the inputs described above. During the literature review, studies that investigated direct signaling mechanisms were used to identify and justify interactions that would make up the structure of the signaling network. The majority of

interactions were added based on studies providing direct experimental evidence in mammalian endothelial cells (93 interactions). We then performed gap filling of each pathway with intermediate reactions (8 interactions) between those supported in endothelial cells if they were well characterized in the literature for other cell types, especially endothelial-related cell types or other cells of the brain, as a number of reactions were specific to the brain but as of yet poorly characterized in the cerebral endothelium. The network consists of 63 nodes (including mRNA, small molecules, proteins, and cell phenotypes/processes) connected by 82 reactions.

The network reconstruction was then converted into a predictive computational model using a previously described logic-based differential equation modeling approach, in which the activation of one node by another is modeled using a normalized Hill function. Logical AND or OR operations were used to represent pathway crosstalk, using the equation $f(x)f(y)$ for AND gating, and $f(x) + f(y) – f(x)f(y)$ for OR gating. Generally, the OR gating was used when either input for a node is sufficient but not necessary for activation, while AND gating is used when each input is necessary. The default reaction parameters include Hill coefficient (1.4) and EC50 (0.5), and the default species parameters include initial activation y_{init} (0), maximal activation y_{max} (1), and time constant τ (1). Logic decisions were primarily made using known biochemical mechanisms, but sometimes inferred from comparing experiments in the literature. The system of logic-based differential equations was generated using Netflux (available at https://github.com/saucermanlab/Netflux) and implemented in MATLAB. The input values of 0.4 weight and the weight w = 0.9 for other nodes was chosen to maximize the node activation throughout the network while maintaining a baseline cell death rate below 20%.

5.5.2 Model Validation

Literature for validating network input-output relationships were identified by searching for each network input and output together with the phrase “endothelial cell” in the Pubmed

database. Other validation literature was identified while reviewing literature for the development of the network. Validation was performed by comparing the qualitative increase, decrease, or no change in output activity of the model simulation to the experimental results in the literature. Changes of less than 1% were categorized as “no change”.

5.5.3 Sensitivity Analysis

A systematic functional sensitivity analysis was performed by simulating full knockdown or overexpression of each node and then predicting the change in activity of every node in the network. First, the steady-state activity of all nodes was computed under baseline conditions (all inputs = 0.4 with the exception of the FUS node, which was left at 0), serving as a control. We then knocked down the activity of each node (or doubled the maximum value of each node), one at a time, and subtracted the basal activity levels from the activity in the knocked down case to calculate “Change in Activity”. Influence was measured as the number of nodes with 20% change or greater in activity following knockdown of the perturbed node, while sensitivity was the number of nodes that will affect a particular target by a 20% change or greater when knocked out. The tight junction sensitivity is defined as the change in claudin 5 activity + the change in occludin activity when the target node is knocked out.

5.5.4 Disease Modeling and Target Prediction

Three different pathologies of the brain (glioma, Alzheimer’s disease, and ischemic stroke) were simulated using different combinations of values for the model inputs. These were based on literature evidence for elevated or reduced levels of the different model inputs in the brain in the context of that disease. All elevated inputs were raised by 25% (to w = 0.65) and all reduced inputs were decreased by 25% (to w = 0.15). Additionally, we assumed FUS as a

delivery mechanism for potential therapeutics, and activated the FUS input node with a weight of w = 0.4. The altered inputs for each disease condition can be found in Table 5.4. After setting the model inputs to recapitulate a pathology state, the full systemic sensitivity analysis was performed for knockdown or overexpression of each node.

The literature was consulted to determine some of the consensus therapeutic goals for each pathology as they relate to our model outputs. A summary of these treatment goals can be found in Table 5.5. A disease score metric was created for each condition by summing the combined effects in the desired direction for each altered output. For example: in the context of glioma, our therapeutic goals are to increase cell death, decrease P-glycoprotein expression, and decrease GLUT1 expression. Therefore, the "glioma score" for any given node knockdown or upregulation is (differential cell death activity – differential P-glycoprotein activity – differential GLUT1 activity). A therapeutic score was computed for each node knockdown and upregulation, all in the context of that disease's input settings. The top 3-5 scoring nodes for either direction of altered expression were further investigated for their impacts on each of the contributing factors to the therapeutic goals (eg. Cell death activity vs. P-glycoprotein activity vs. GLUT1 activity). Finally, we tested the effects of combinations of two high-scoring node alterations (one upregulation and one knockdown) for each disease setting to determine optimal synergistic pairings for therapy.

5.6 Chapter 5 Figures

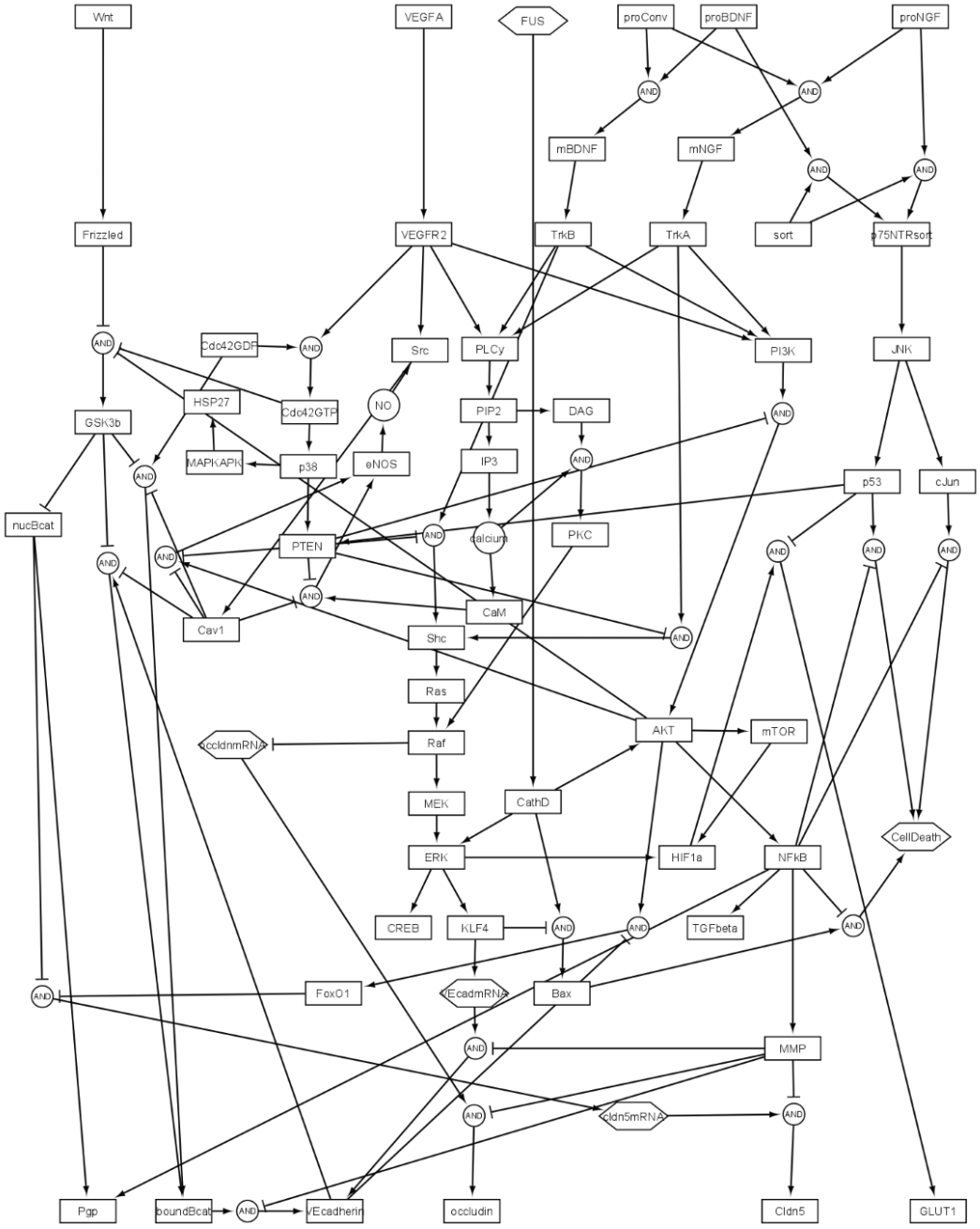

Figure 5.1 Reconstruction of the brain endothelial cell signaling network. Each of the 63 nodes represents a protein, mRNA, small molecule, cell process, or external stimulus in the model. Each arrow indicates a reaction based on experimental data of activation or inhibition from endothelial cells or a an endothelial-cell-related cell line. Where shown, some reactions combine the influence of multiple reactants via AND gate logic. Multiple reactions affecting the same product are combined using OR gate logic.

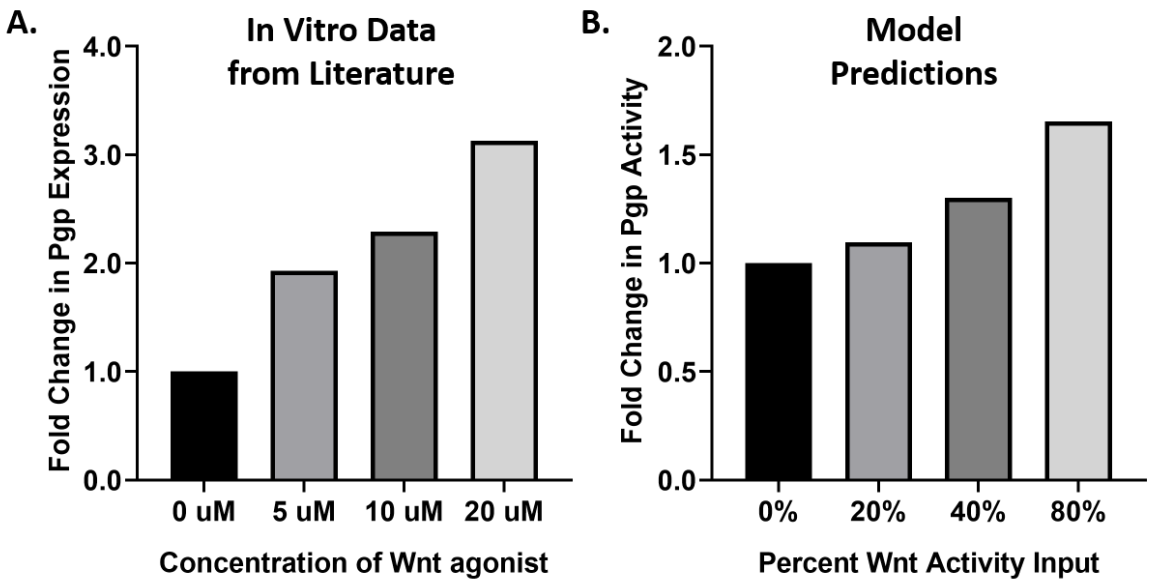

Figure 5.2 Example of model validation with a single stimulus. A) Independent experimental data from Lim et al 2008 (267) showing the dose-dependent increase in p-glycoprotein expression in response to treatment with a Wnt agonist. B) Predicted response of p-glycoprotein activity in response to increasing levels of Wnt input in the model. The model prediction is expressed as a percent of maximal protein level.

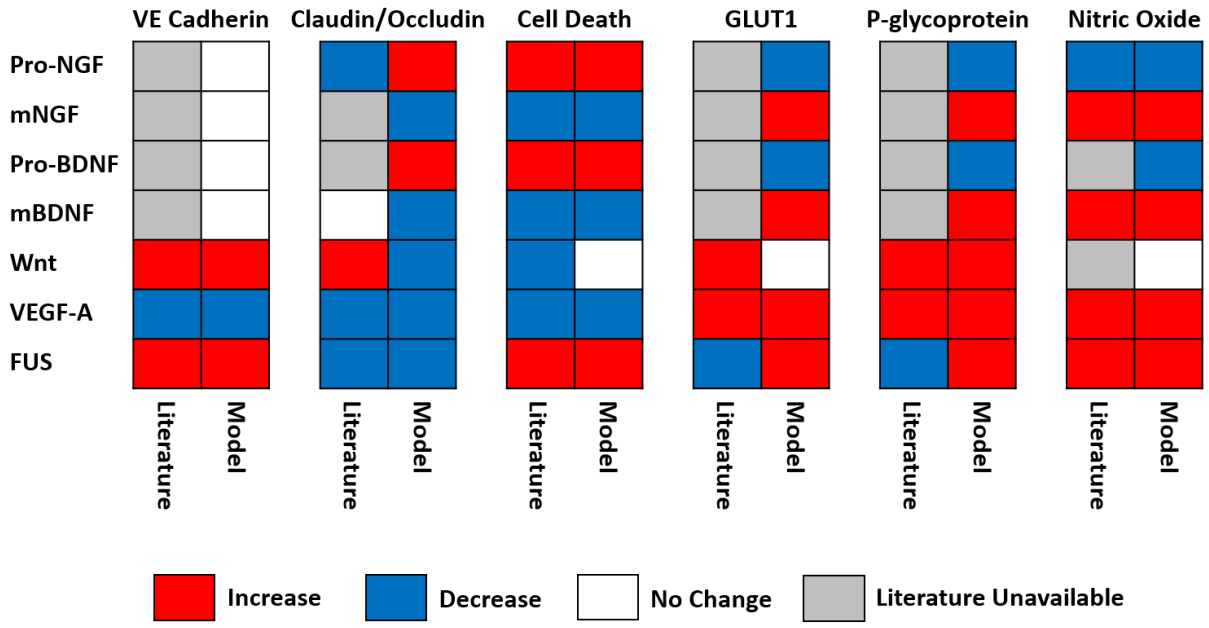

Figure 5.3 Validation of network input-output relationships predicted by the model. The qualitative response of selected model outputs is shown in response to each of 7 input stimuli. The responses of outputs to a single input from published experimental observations of endothelial cells are displayed in the first column. The model's predictions of the output responses are displayed in the second column. The model validates 19 of the 26 (73%) of the predictions for which there was experimental data available.

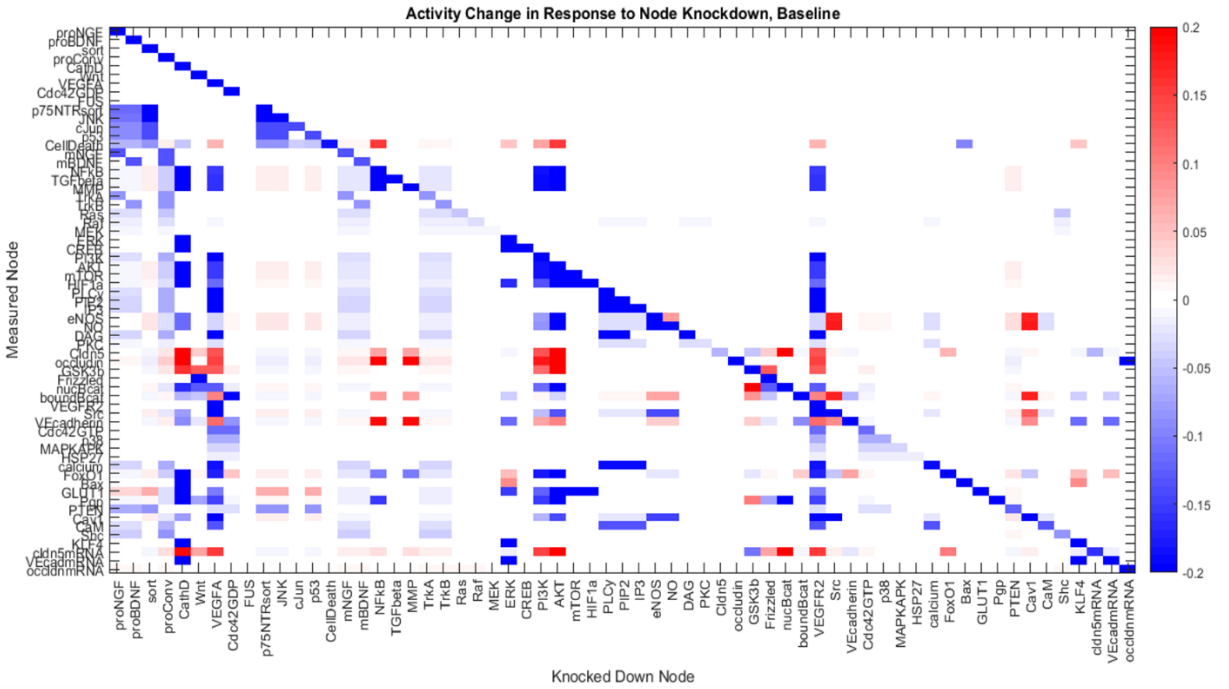

	proNGF	proBDNF	Pro-Conv	sortilin	VEGF-A	Wnt	Cath D	FUS
INPUT VALUE	0.4	0.4	0.4	0.4	0.4	0.4	0.4	0

Figure 5.4 Sensitivity analysis of model under baseline conditions. Results of a full sensitivity analysis where all possible knockdowns (x-axis) are performed under baseline conditions (0.4 weight for each input with the exception of FUS, 0). The change in activity (knockdown – control) for each output node (y-axis) is measured as a change in color ranging from 20% decrease in activity (blue) to 20% increase in activity (red).

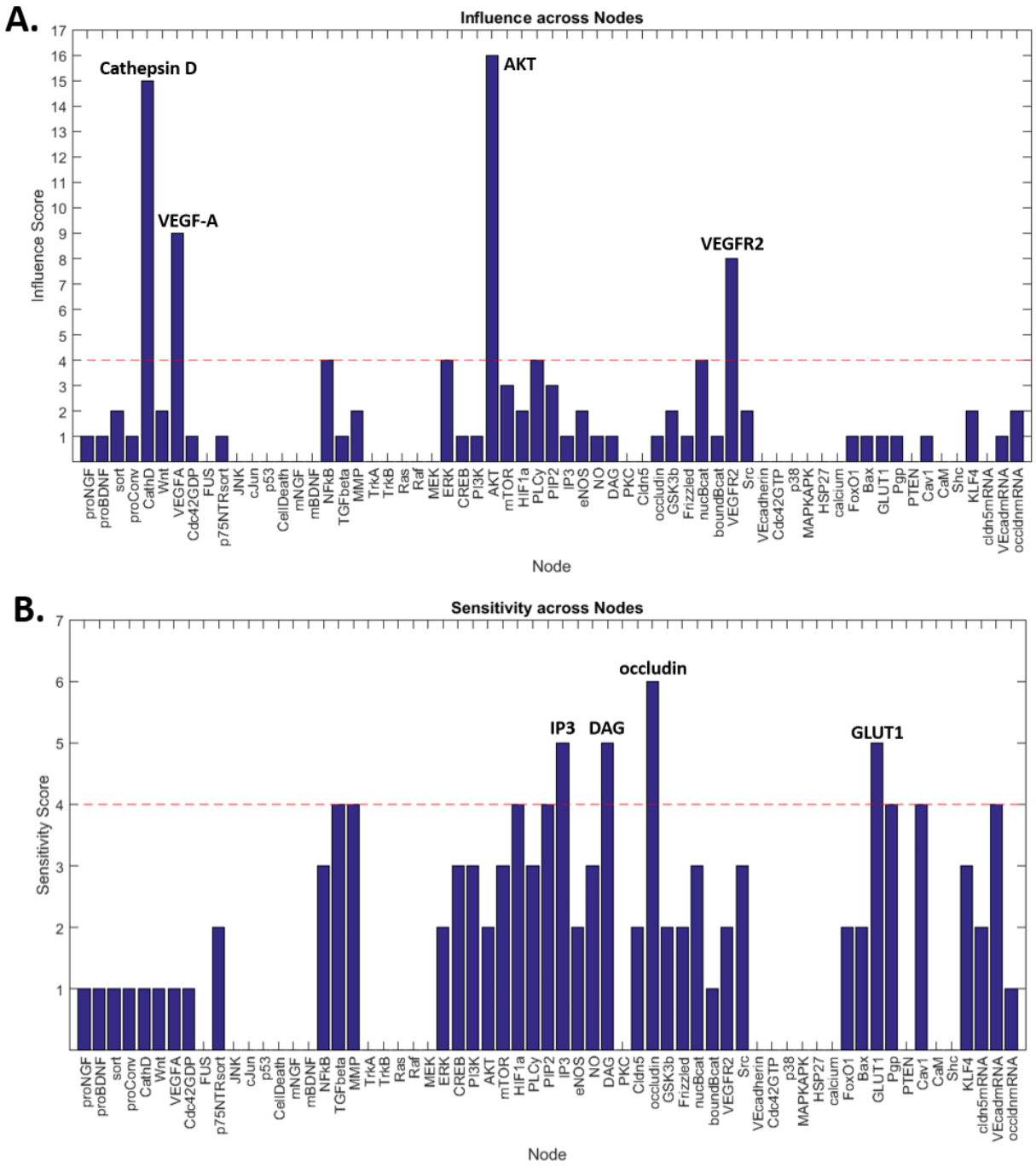

Figure 5.5 Full network sensitivity analysis reveals most influential and most sensitive nodes under baseline conditions. A) Influence of each node in the network under baseline conditions, defined as the number of species whose activity is altered by 20% or more following knockdown of that node. The most influential nodes at baseline are AKT, cathepsin D, VEGF-A, and VEGFR2. B) Sensitivity of each node in the network under baseline conditions, defined as the number of species knockdowns that result in a 20% or greater change in activity of that node. The sensitive nodes at baseline are occludin, IP3, DAG, and GLUT1.

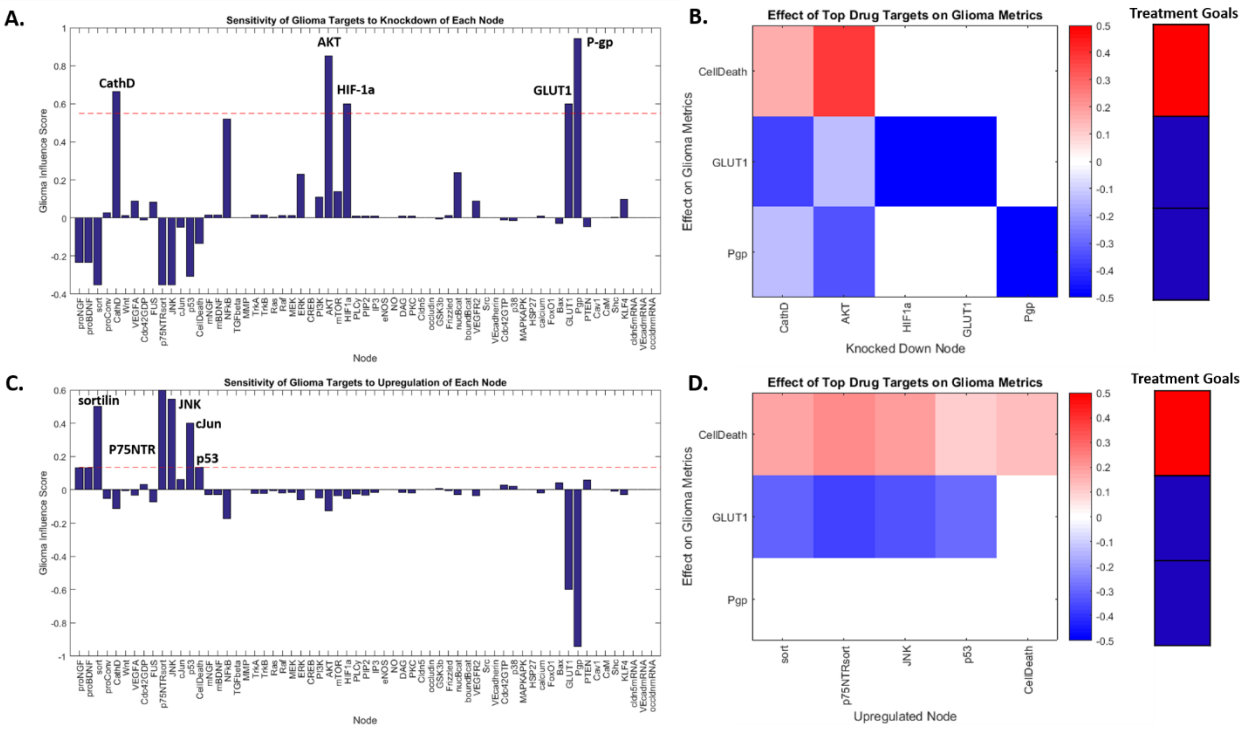

Figure 5.6 Identification of most influential nodes under glioma + FUS context for therapeutic glioma metrics. A) Sensitivity of glioma therapeutic metrics (increased cell death, decreased GLUT1, decreased p-glycoprotein) to knockdown of any node in the network. B) Effect of most influential knockdowns (cathepsin D, AKT, HIF1a, GLUT1, p-glycoprotein) on each of the individual contributing outputs in the glioma therapeutic metric. C) Sensitivity of glioma therapeutic metrics to overexpression of any node in the network. D) Effect of most influential overexpressions (sortilin, p75, JNK, cJun, p53) on the individual contributing outputs in the glioma therapeutic metric.

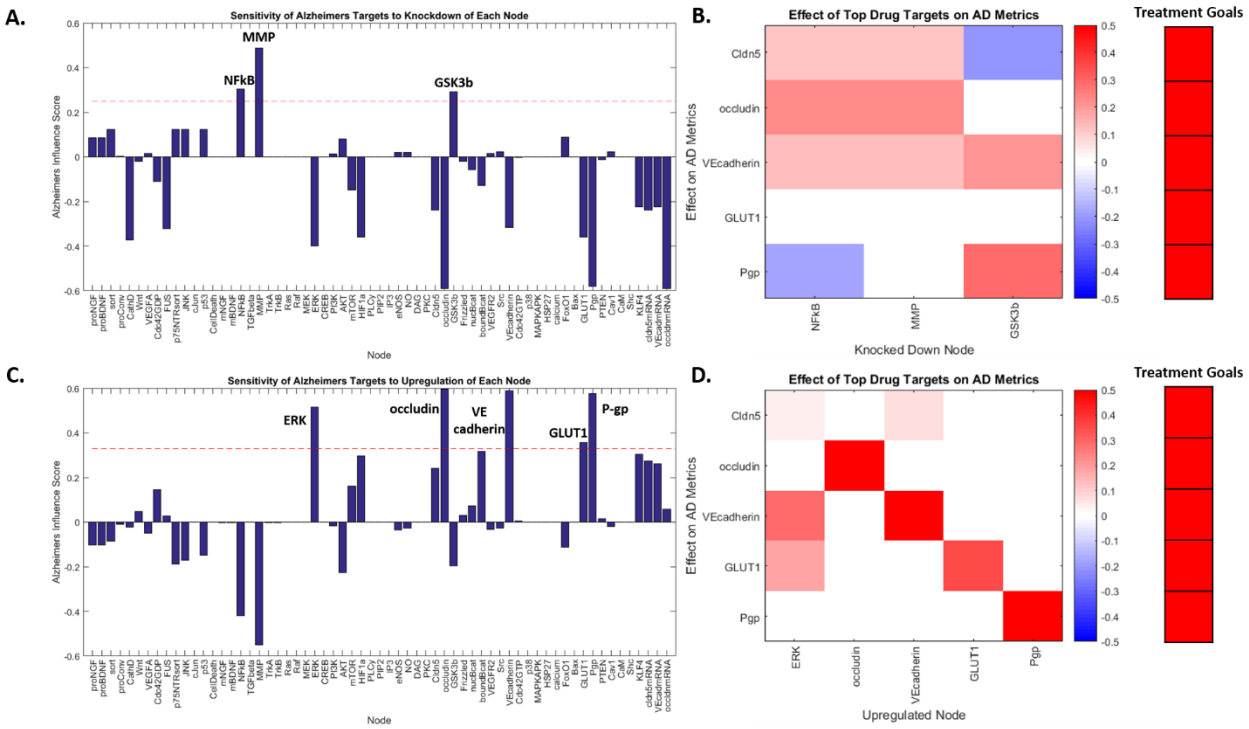

Figure 5.7 Identification of most influential nodes under Alzheimer's + FUS context for therapeutic Alzheimer's metrics. A) Sensitivity of Alzheimer's therapeutic metrics (increased claudin-5, occludin, VE cadherin, GLUT1, and p-glycoprotein) to knockdown of any node in the network. B) Effect of most influential knockdowns (NFkB, MMP, GSK3b) on each of the individual contributing outputs in the Alzheimer's therapeutic metric. C) Sensitivity of Alzheimer's therapeutic metrics to overexpression of any node in the network. D) Effect of most influential overexpressions (ERK, occludin, VE cadherin, GLUT1, p-glycoprotein) on the individual contributing outputs in the Alzheimer's therapeutic metric.

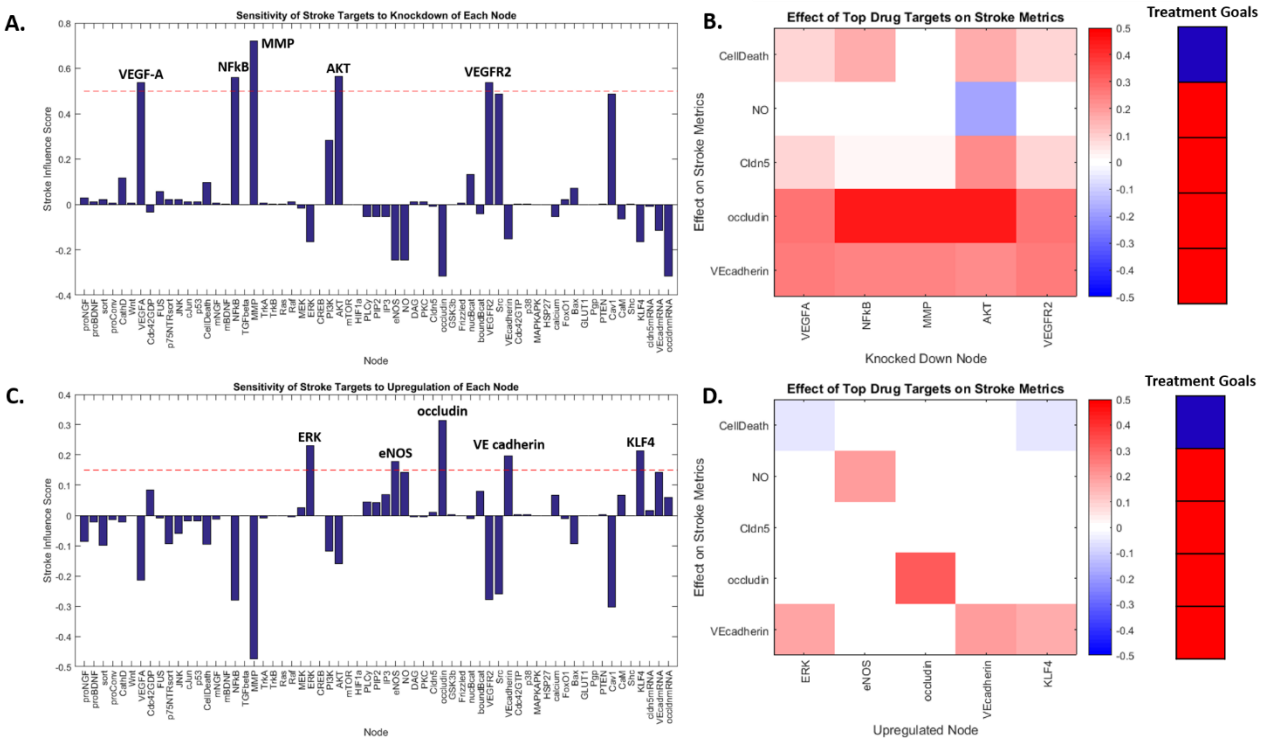

Figure 5.8 Identification of most influential nodes under stroke + FUS context for therapeutic stroke metrics. A) Sensitivity of stroke therapeutic metrics (decreased cell death, increased nitric oxide, claudin-5, occludin, and VE cadherin) to knockdown of any node in the network. B) Effect of most influential knockdowns (VEGF-A, NFkB, MMP, AKT, VEGFR2) on each of the individual contributing outputs in the stroke therapeutic metric. C) Sensitivity of stroke therapeutic metrics to overexpression of any node in the network. D) Effect of most influential overexpressions (ERK, eNOS, occludin, VE cadherin, KLF4) on the individual contributing outputs in the stroke therapeutic metric.

5.7 Chapter 5 Tables

Species information					
ID	**name**	**Yinit**	**Ymax**	**tau**	**type**
proNGF	proNGF	0	1	1	protein
proBDNF	proBDNF	0	1	1	protein
sort	sortilin	0	1	1	protein
proConv	pro-convertase (plasmin, tPa, etc)	0	1	1	protein
CathD	Cathepsin D	0	1	1	protein
Wnt	Wnt	0	1	1	protein
VEGFA	VEGF-A	0	1	1	protein
Cdc42GDP	Cdc42 * GDP	0	1	1	protein
FUS	FUS	0	1	1	phenotype
p75NTRsort	p75NTR:sortilin complex	0	1	1	protein
JNK	JNK	0	1	1	protein
cJun	cJun	0	1	1	protein
p53	p53	0	1	1	protein
CellDeath	Cell Death	0	1	1	phenotype
mNGF	mature cleaved NGF	0	1	1	protein
mBDNF	mature cleaved BDNF	0	1	1	protein
NFkB	NFkappaB	0	1	1	protein
TGFbeta	TGF beta	0	1	1	protein
MMP	matrix metalloprotease 2,9	0	1	1	protein
TrkA	TrkA receptor	0	1	1	protein
TrkB	TrkB receptor	0	1	1	protein
Ras	Ras	0	1	1	protein
Raf	Raf	0	1	1	protein
MEK	MEK	0	1	1	protein
ERK	ERK	0	1	1	protein
CREB	CREB	0	1	1	protein
PI3K	PI3 kinase	0	1	1	protein
AKT	AKT	0	1	1	protein
mTOR	mTOR	0	1	1	protein
HIF1a	HIF1alpha	0	1	1	protein
PLCy	PLC gamma	0	1	1	protein
PIP2	PIP2	0	1	1	protein
IP3	IP3	0	1	1	protein
eNOS	eNOS	0	1	1	protein
NO	nitric oxide	0	1	1	smallMolecule
DAG	DAG	0	1	1	protein
PKC	PKC	0	1	1	protein

Cldn5	claudin 5	0	1	1	protein
occludin	occludin	0	1	1	protein
GSK3b	GSK3beta	0	1	1	protein
Frizzled	Frizzled	0	1	1	protein
nucBcat	nuclear beta catenin	0	1	1	protein
boundBcat	membrane-bound beta catenin	0	1	1	protein
VEGFR2	VEGF receptor 2	0	1	1	protein
Src	Src	0	1	1	protein
VEcadherin	VE cadherin	0	1	1	protein
Cdc42GTP	Cdc42 * GTP	0	1	1	protein
p38	p38	0	1	1	protein
MAPKAPK	MAPKAPK	0	1	1	protein
HSP27	heat shock protein 27	0	1	1	protein
calcium	calcium	0	1	1	smallMolecule
FoxO1	FoxO1	0	1	1	protein
Bax	Bax	0	1	1	protein
GLUT1	glucose transporter 1	0	1	1	protein
Pgp	P-glycoprotein (multi drug resistance 1)	0	1	1	protein
PTEN	PTEN	0	1	1	protein
Cav1	caveolin 1	0	1	1	protein
CaM	calmodulin	0	1	1	protein
Shc	Shc	0	1	1	protein
KLF4	KLF4	0	1	1	protein
cldn5mRNA	claudin 5 mRNA	0	1	1	mRNA
VEcadmRNA	VE cadherin mRNA	0	1	1	mRNA
occldnmRNA	occludin mRNA	0	1	1	mRNA

Table 5.1 Species information for brain endothelial cell signaling network model.

Reaction Information						
module	**ID**	**Rule**	**Weight**	**n**	**EC50**	**PMID**
inputs	i1	=> proNGF	0.3	1.4	0.5	15169782
inputs	i2	=> proBDNF	0.3	1.4	0.5	15169782
inputs	i3	=> proConv	0.3	1.4	0.5	11896152
inputs	i4	=> Wnt	0.3	1.4	0.5	31873116
inputs	i5	=> VEGFA	0.3	1.4	0.5	19357264
inputs	i6	=> CathD	0.3	1.4	0.5	24466373
inputs	i7	=> sort	0.3	1.4	0.5	30046375
inputs	i8	=> Cdc42GDP	0.3	1.4	0.5	26253403
inputs	i9	=> FUS	0	1.4	0.5	33526842
middle	r1	proNGF & sort => p75NTRsort	0.9	1.4	0.5	26029724
middle	r2	proBDNF & sort => p75NTRsort	0.9	1.4	0.5	30046375
middle	r3	p75NTRsort => JNK	0.9	1.4	0.5	30046375
middle	r5	JNK => cJun	0.9	1.4	0.5	15979056
middle	r6	JNK => p53	0.9	1.4	0.5	10920209
middle	r7	p53 => PTEN	0.9	1.4	0.5	30790589
middle	r8	p38 => PTEN	0.9	1.4	0.5	16418168
middle	r9	proNGF & proConv => mNGF	0.9	1.4	0.5	16618925
middle	r10	proBDNF & proConv => mBDNF	0.9	1.4	0.5	15486301
middle	r11	VEGFA => VEGFR2	0.9	1.4	0.5	31524227
middle	r12	VEGFR2 => PLCy	0.9	1.4	0.5	11387210
middle	r13	VEGFR2 => Src	0.9	1.4	0.5	19050761
middle	r14	VEcadherin & !GSK3b & !Cav1 => boundBcat	0.9	1.4	0.5	16816383, 21960684, 22264731
middle	r15	Cdc42GDP & !GSK3b & !Cav1 => boundBcat	0.9	1.4	0.5	16816383, 21960684, 16322481
middle	r16	!GSK3b => nucBcat	0.9	1.4	0.5	16816383
middle	r17	Src => Cav1	0.9	1.4	0.5	27572515
middle	r18	VEGFR2 & Cdc42GDP => Cdc42GTP	0.9	1.4	0.5	14724572
middle	r19	VEGFR2 => PI3K	0.9	1.4	0.5	17303569
middle	r20	Cdc42GTP => p38	0.9	1.4	0.5	14724572
middle	r21	p38 => MAPKAPK	0.9	1.4	0.5	15371454
middle	r22	MAPKAPK => HSP27	0.9	1.4	0.5	22124154
middle	r23	mNGF => TrkA	0.9	1.4	0.5	28843696
middle	r24	mBDNF => TrkB	0.9	1.4	0.5	15169782
middle	r25	TrkA & !PTEN=> Shc	0.9	1.4	0.5	8155326, 20472716

middle	r26	TrkB & !PTEN => Shc	0.9	1.4	0.5	30926745, 20472716
middle	r27	Shc => Ras	0.9	1.4	0.5	10362356
middle	r28	Ras => Raf	0.9	1.4	0.5	30828992
middle	r29	Raf => MEK	0.9	1.4	0.5	26136364
output	r30	!Raf => occldnmRNA	0.9	1.4	0.5	16924233
middle	r31	MEK => ERK	0.9	1.4	0.5	29366810
output	r32	ERK => CREB	0.9	1.4	0.5	20067582
output	r33	ERK => HIF1a	0.9	1.4	0.5	10683440
middle	r34	ERK => KLF4	0.9	1.4	0.5	20551324
middle	r35	TrkA => PI3K	0.9	1.4	0.5	17666398
middle	r36	TrkB => PI3K	0.9	1.4	0.5	15169782
middle	r37	PI3K & !PTEN=> AKT	0.9	1.4	0.5	31787905
middle	r38	AKT => NFkB	0.9	1.4	0.5	28173835
output	r39	NFkB => TGFbeta	0.9	1.4	0.5	31934265
middle	r40	NFkB => MMP	0.9	1.4	0.5	23714001
middle	r41	NFkB => Pgp	0.9	1.4	0.5	30312753
middle	r42	AKT & !VEcadherin=> FoxO1	0.9	1.4	0.5	19887561, 18604199
middle	r43	AKT => mTOR	0.9	1.4	0.5	25582201
middle	r44	AKT & !Cav1 &!PTEN => eNOS	0.9	1.4	0.5	17303569, 22323292, 19962452
output	r45	mTOR => HIF1a	0.9	1.4	0.5	18519793
middle	r46	CathD => ERK	0.9	1.4	0.5	29024694
middle	r47	CathD => AKT	0.9	1.4	0.5	29024694
middle	r48	CathD & !KLF4 => Bax	0.9	1.4	0.5	17395004, 29203245
middle	r49	TrkA => PLCy	0.9	1.4	0.5	20434587
middle	r50	TrkB => PLCy	0.9	1.4	0.5	14603320
middle	r51	PLCy => PIP2	0.9	1.4	0.5	8612675
middle	r52	PIP2 => IP3	0.9	1.4	0.5	1982067
middle	r53	IP3 => calcium	0.9	1.4	0.5	21633077
middle	r54	calcium => CaM	0.9	1.4	0.5	27199448
middle	r55	CaM & !Cav1 & !PTEN => eNOS	0.9	1.4	0.5	14736917, 22323292, 19962452
output	r56	eNOS => NO	0.9	1.4	0.5	25366614
middle	r57	NO => Src	0.9	1.4	0.5	22323292
middle	r58	PIP2 => DAG	0.9	1.4	0.5	1982067
middle	r59	DAG & calcium => PKC	0.9	1.4	0.5	21193229
middle	r60	PKC => Raf	0.9	1.4	0.5	10327068
middle	r61	Wnt => Frizzled	0.9	1.4	0.5	27758766

middle	r62	!Frizzled & !AKT & !Cdc42GTP => GSK3b	0.9	1.4	0.5	20849862, 18156211, 12167628
middle	r63	nucBcat => Pgp	0.9	1.4	0.5	23771630
output	r64	cJun & !NFkB => CellDeath	0.9	1.4	0.5	10473668, 9585425
output	r65	p53 & !NFkB => CellDeath	0.9	1.4	0.5	29767244, 9585425
output	r66	Bax & !NFkB => CellDeath	0.9	1.4	0.5	29767244, 9585425
output	r67	HIF1a & !p53 => GLUT1	0.9	1.4	0.5	23047702, 24857662
output	r68	!nucBcat & !FoxO1 => cldn5mRNA	0.9	1.4	0.5	24522189
output	r69	cldn5mRNA & !MMP => Cldn5	0.9	1.4	0.5	21717368
output	r70	occldnmRNA & !MMP => occludin	0.9	1.4	0.5	22378877
output	r71	KLF4 => VEcadmRNA	0.9	1.4	0.5	20724706
output	r72	VEcadmRNA & !MMP => VEcadherin	0.9	1.4	0.5	16391847
output	r73	boundBcat & !MMP => VEcadherin	0.9	1.4	0.5	7698986, 16391847
middle	r74	FUS => CathD	0.9	1.4	0.5	33526842

Table 5.2 Reaction parameters and literature sources for brain endothelial cell signaling network model.

Input		Output		Measurement		PMID
proNGF		claudin-5/occludin		Decrease		31073629
proNGF		cell death		Increase		26029724
proNGF		nitric oxide		Increase		32696589
mNGF		cell death		Decrease		30680928
mNGF		nitric oxide		Increase		20569463
proBDNF		cell death		Increase		30046375
mBDNF		claudin-5/occludin		No change		22002662
mBDNF		cell death		Decrease		30877409
mBDNF		nitric oxide		Increase		30354255
Wnt		VE cadherin		Increase		30451830
Wnt		claudin-5/occludin		Increase		30932814
Wnt		cell death		Decrease		17035633
Wnt		GLUT1		Increase		19129494
Wnt		P-glycoprotein		Increase		18624906
VEGF-A		VE cadherin		Decrease		17060906
VEGF-A		claudin-5/occludin		Decrease		7873103
VEGF-A		cell death		Decrease		10066377
VEGF-A		GLUT1		Increase		10845612
VEGF-A		P-glycoprotein		Increase		22245726
VEGF-A		nitric oxide		Increase		9837777
FUS		VE cadherin		Increase		32275861
FUS		claudin-5/occludin		Decrease		18378064
FUS		cell death		Increase		30957188
FUS		GLUT1		Decrease		24368263
FUS		P-glycoprotein		Decrease		31920511
FUS		nitric oxide		Increase		29857968

Table 5.3 Literature validations of input-output relationships for brain endothelial cell signaling network model.

	NGF	BDNF	VEGF-A	Wnt	Cathepsin D
Control "healthy" brain	---	---	---	---	---
Glioma **PMID:**	Elevated 19074980	Elevated 28640008	Elevated 33125340	Elevated 29462960	Elevated 15958563
Alzheimer's Disease **PMID:**	Shift to pro-NGF 11520181	Shift to pro-BDNF 30428894	Reduced 17587256	Reduced 31191253	Reduced 33445607
Ischemic stroke **PMID:**	---	Reduced 33210043	Elevated 29342116	Elevated 33071819	Reduced 32450052

Table 5.4 Alterations in model inputs in different disease states. A review of the literature revealed that many of the inputs to our computational model display altered expression in the context of disease. In the case of glioma, elevated levels of NGF, BDNF, VEGF-A, Wnt, and cathepsin D have all been observed. In Alzheimer's, studies have demonstrated a reduction in VEGF-A, Wnt, and cathepsin D, and a shift towards the pro-neurotrophin forms of BDNF and NGF. The infarcted brain after ischemic stroke demonstrates reduced levels of BDNF and cathepsin D, but increased levels of VEGF-A and Wnt. These findings informed revised model input weights for the nodes noted in the table when simulating these disease states, with elevated levels corresponding to a 25% increase above baseline, and reduced levels corresponding to a 25% decrease from baseline.

	Glioma	Alzheimer's Disease	Ischemic Stroke
Adherens Junctions **PMID:**	---	Increase 28902142	Increase 29949404
Tight Junctions **PMID:**	---	Increase 28902142	Increase 29949404
Cell Death **PMID:**	Increase 30486451	---	Decrease 31799500
GLUT1 **PMID:**	Decrease 30990881	Increase 25730668	---
P-glycoprotein **PMID:**	Decrease 31248184	Increase 26159621	---
Nitric oxide **PMID:**	---	---	Increase 29152213

Table 5.5 Therapeutic goals for model outputs in different disease states. A review of the literature allowed for the identification of therapeutic goals for each pathology simulated with respect to the computational model outputs. Our treatment goals for glioma were to increase cell death while decreasing GLUT1 and p-glycoprotein expression. For Alzheimer's disease, we aimed to increase adherens and tight junctional proteins, as well as increasing GLUT1 and p-glycoprotein. In the context of stroke, our goals were to decrease cell death while increasing adherens junctions, tight junctions, and nitric oxide production.

5.8 Chapter 5 Supplemental Figures

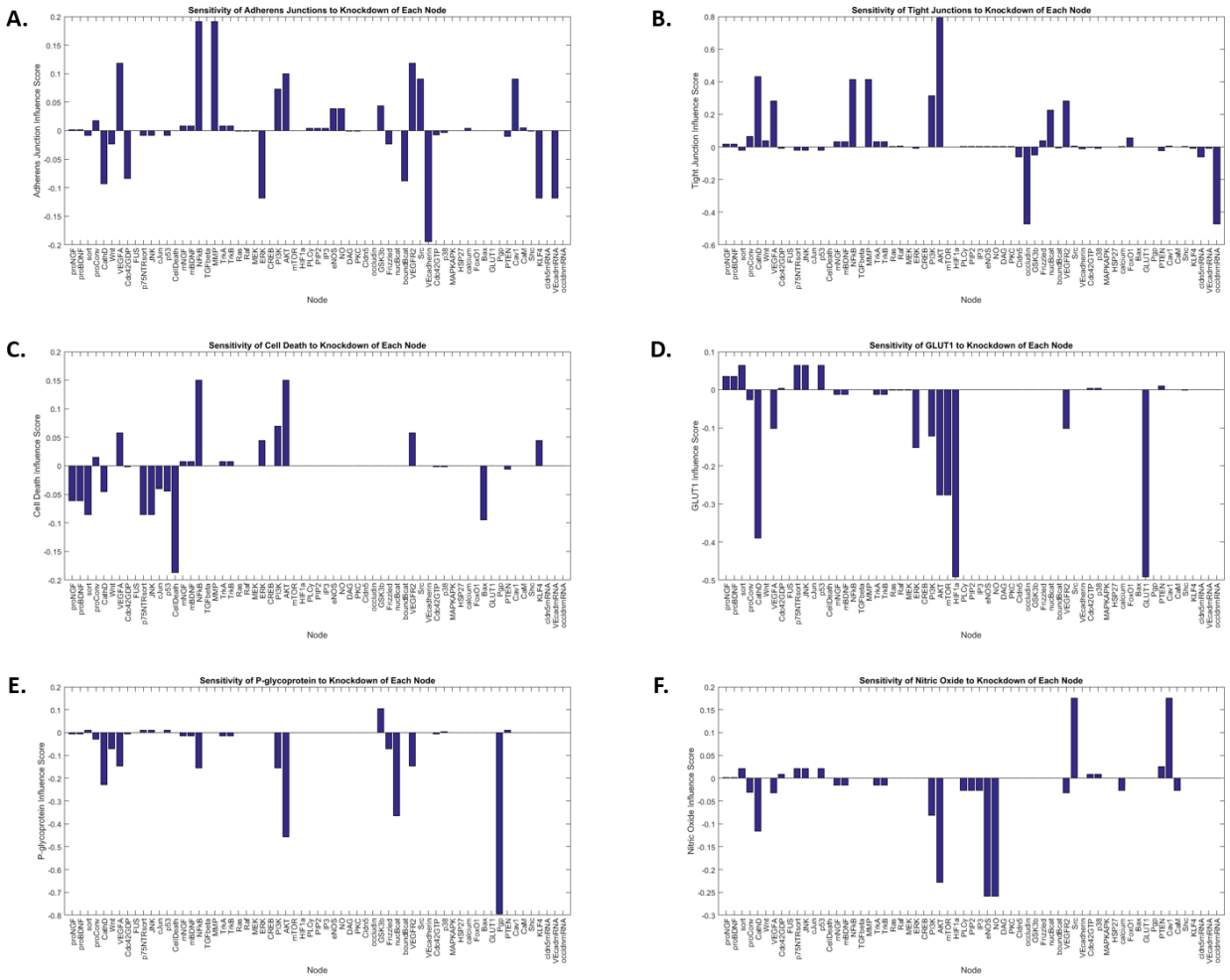

Figure 5.S1 Full network sensitivity analysis reveals nodes with the greatest influence on model outputs under baseline conditions. Sensitivity of A) VE cadherin, B) claudin-5 and occludin, C) cell death, D) GLUT1, E) p-glycoprotein, F) nitric oxide to each node knockdown in the network under baseline conditions.

A.

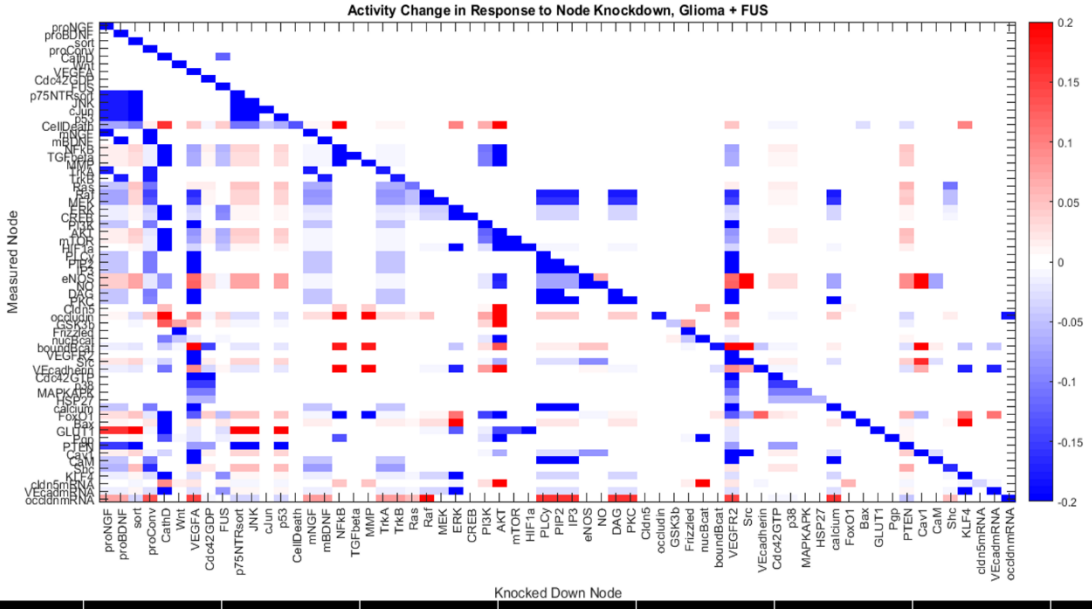

	proNGF	proBDNF	Pro-Conv	sortilin	VEGF-A	Wnt	Cath D	FUS
INPUT VALUE	0.65	0.65	0.4	0.4	0.65	0.65	0.65	0.4

B.

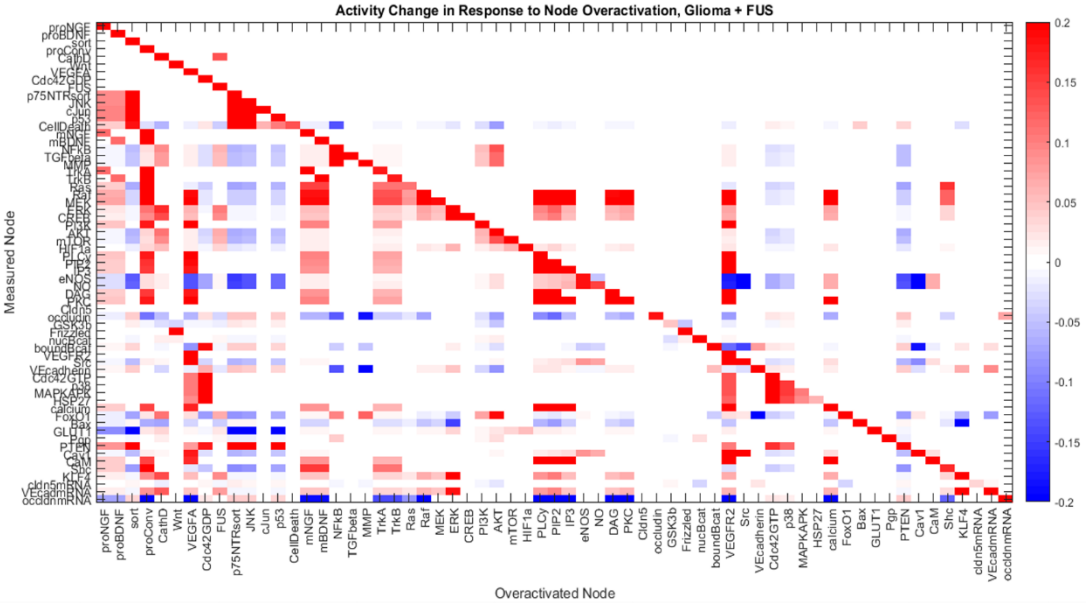

	proNGF	proBDNF	Pro-Conv	sortilin	VEGF-A	Wnt	Cath D	FUS
INPUT VALUE	0.65	0.65	0.4	0.4	0.65	0.65	0.65	0.4

Figure 5.S2 Full network sensitivity analysis under glioma + FUS input conditions. A) Results of a full sensitivity analysis where all possible knockdowns (x-axis) are performed under glioma + FUS conditions. B) Results of a full sensitivity analysis where all possible overexpressions (x-axis) are performed under glioma + FUS conditions.

A.

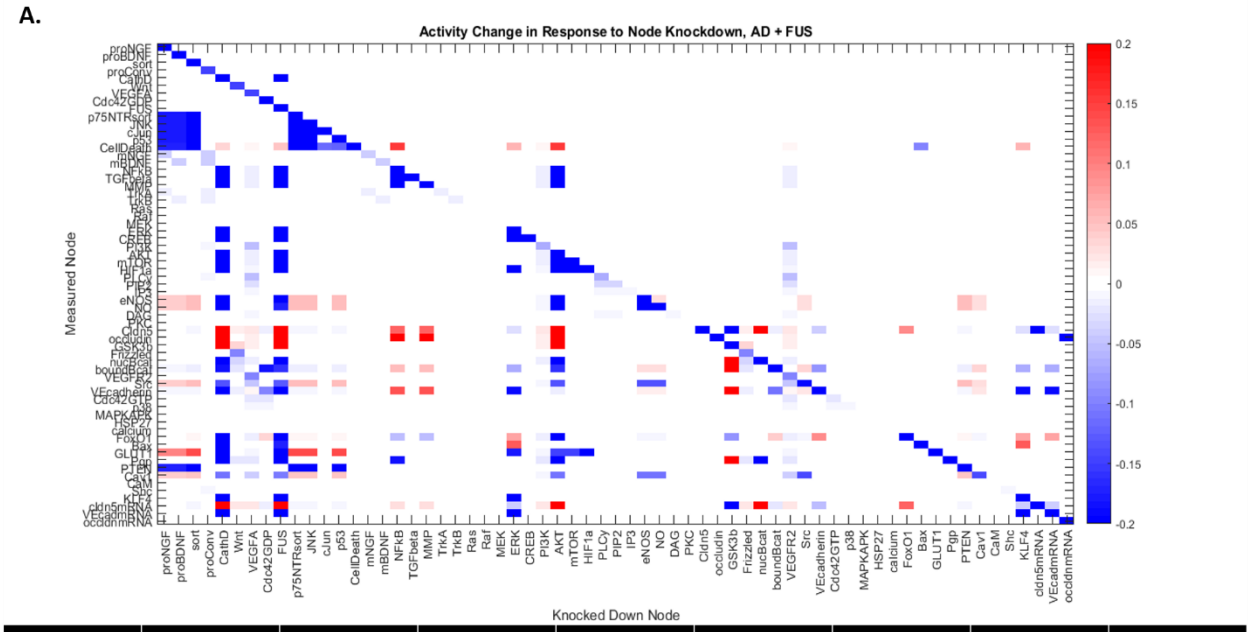

	proNGF	proBDNF	Pro-Conv	sortilin	VEGF-A	Wnt	Cath D	FUS
INPUT VALUE	0.4	0.4	0.15	0.65	0.15	0.15	0.15	0.4

B.

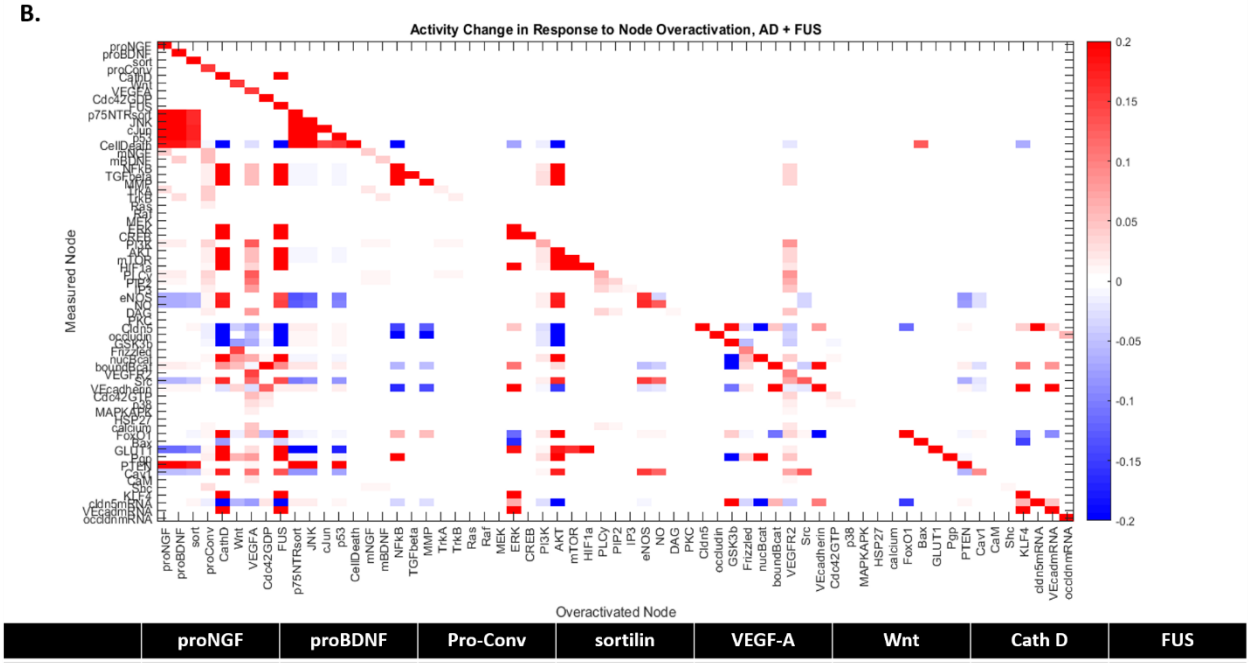

	proNGF	proBDNF	Pro-Conv	sortilin	VEGF-A	Wnt	Cath D	FUS
INPUT VALUE	0.4	0.4	0.15	0.65	0.15	0.15	0.15	0.4

Figure 5.S3 Full network sensitivity analysis under Alzheimer's disease + FUS input conditions. A) Results of a full sensitivity analysis where all possible knockdowns (x-axis) are performed under Alzheimer's disease + FUS conditions. B) Results of a full sensitivity analysis where all possible overexpressions (x-axis) are performed under Alzheimer's disease + FUS conditions.

A.

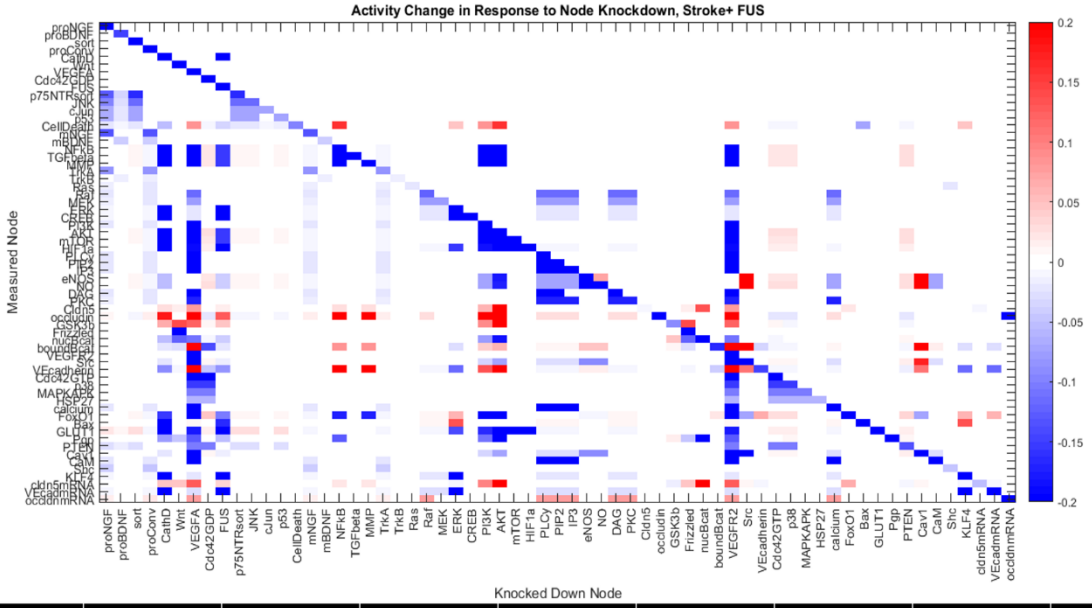

	proNGF	proBDNF	Pro-Conv	sortilin	VEGF-A	Wnt	Cath D	FUS
INPUT VALUE	0.4	0.15	0.4	0.4	0.65	0.65	0.15	0.4

B.

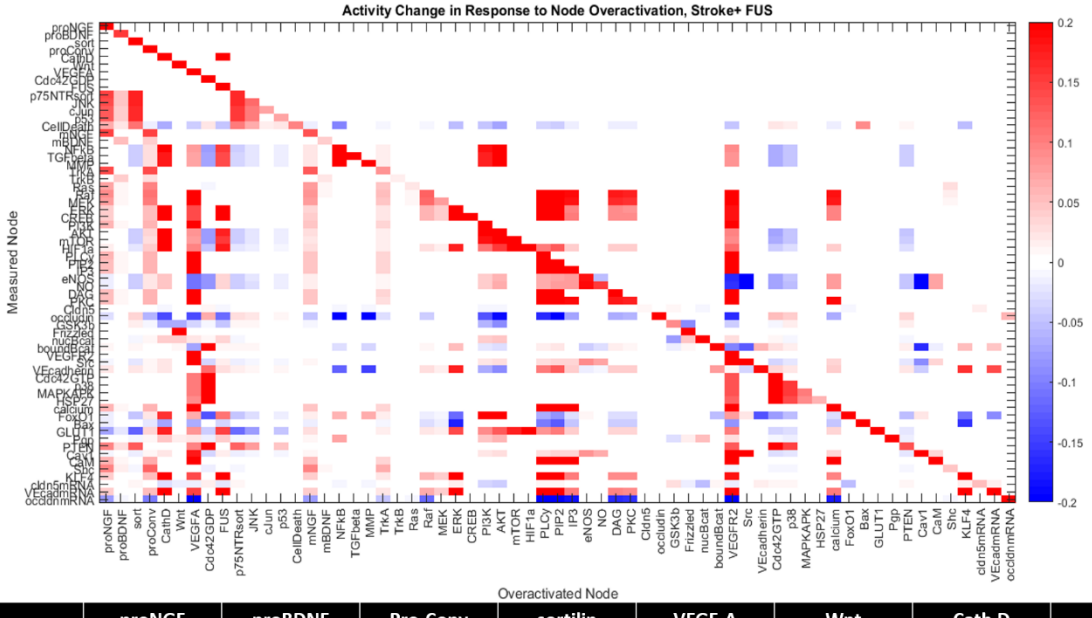

	proNGF	proBDNF	Pro-Conv	sortilin	VEGF-A	Wnt	Cath D	FUS
INPUT VALUE	0.4	0.15	0.4	0.4	0.65	0.65	0.15	0.4

Figure 5.S4 Full network sensitivity analysis under stroke + FUS input conditions. A) Results of a full sensitivity analysis where all possible knockdowns (x-axis) are performed under stroke + FUS conditions. B) Results of a full sensitivity analysis where all possible overexpressions (x-axis) are performed under stroke + FUS conditions.

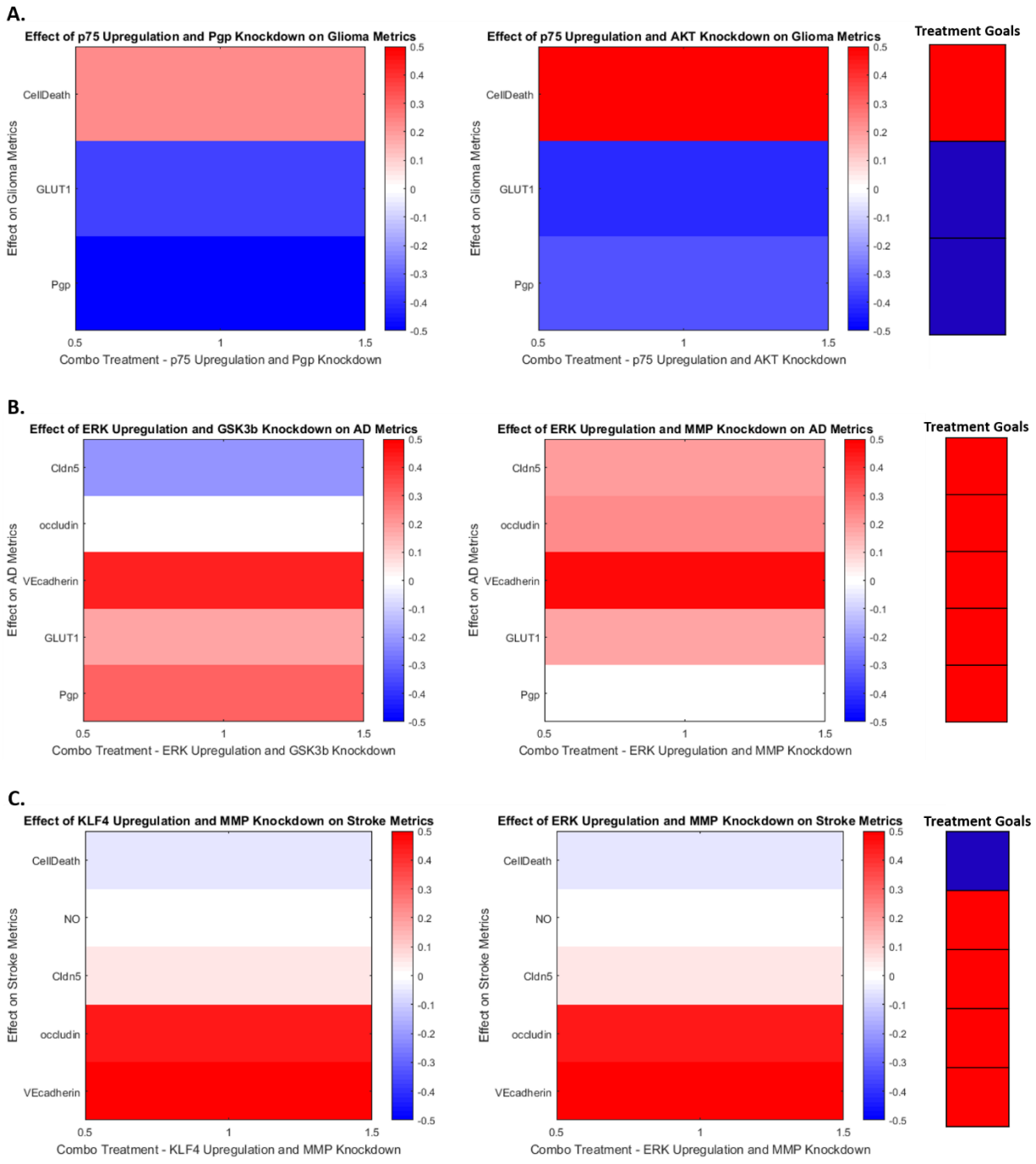

Figure 5.S5 Effects of combinatorial node alterations in different disease contexts. A) Predicted impact of two different combinations of two influential node alterations (one knockdown, one overexpression) on glioma therapeutic output metrics. B) Predicted impact of two different combinations of two influential node alterations (one knockdown, one overexpression) on Alzheimer's therapeutic output metrics. C) Predicted impact of two different combinations of two influential node alterations (one knockdown, one overexpression) on stroke therapeutic output metrics.

Chapter 6: Future Directions

6.1 Optimization of Pulse Length to Maximize Endothelial Sonoselective Transfection Efficiency

In Chapter 3 of this dissertation, we develop a method for targeted transfection of the cerebral vasculature using low-pressure focused ultrasound (FUS) in conjunction with gas-filled microbubbles electrostatically conjugated to plasmid DNA, which we term “sonoselective” transfection. We demonstrate an inverse correlation between the peak-negative pressure of FUS pulsing and the fraction of transfected cells positive for endothelial cell markers. While the peak-negative pressure is clearly a very influential parameter for affecting the extent and cell type specificity of gene delivery, there are a number of other FUS parameters which could be tuned to better optimize the desired bioeffects and cells targeted. The role of such parameters on BBB disruption is a topic of great interest in the field, with studies investigating the influence of transducer frequency(283), sonication duration(284), microbubble size(285), and microbubble dose(286, 287).

As with previous studies of FUS-mediated drug or gene delivery to the brain, our studies in Chapter 3 used pulsed ultrasound with short “on” periods separated by longer “off” periods. The length of time in each cycle when the transducer is on and generating pressure waves is referred to as the pulse length or burst length. In contrast to regimens intended to produce thermal damage and lesions, FUS for BBB-opening applications typically utilize very short pulse lengths, on the order of milliseconds or shorter. Continuous waves or long pulse lengths have been demonstrated to produce heating in the near-field region, as well as tissue damage, when applied to the brain in the presence of microbubbles(288, 289). Standing wave formation is an additional source of concern with longer pulse lengths, as this phenomenon results in highly variable bioeffects and in situ pressures at the focal region(290). Yet within the range of microseconds to tens of milliseconds, longer pulse lengths have been found to increase the extent of BBB disruption and payload delivery(234, 286, 291).

Given the conflicting interests of increasing therapeutic delivery and minimizing tissue heating and damage, FUS pulse length is a parameter whose optimization is nuanced and not yet fully understood. Particularly in our novel regime of sonoselective transfection, it would be very useful to conduct a parameter sweep to optimize the pulse length to maximize transfection efficiency to endothelial cells while continuing to minimize BBB disruption. This could be done by delivering plasmid-bound MBs in the same method as used in Chapter 3, but holding the peak-negative pressure consistent at 0.1 MPa and varying the pulse length. We could then measure the endothelial selectivity and fraction of endothelial cells transfected once again with immunofluorescent staining and single-cell RNA sequencing. We would likely expect any potential increases in transfection efficiency to occur with increased pulse lengths, as longer pulse lengths will increase the amount of time each cycle that the vasculature is exposed to oscillating microbubbles. Therefore, we would consider pulse lengths at the previous study length or longer (from 10 ms up to 50, 100, and 200 ms) to explore differential transfection effects. Additionally, an important consideration for this experiment will be to monitor for tissue heating (the primary concern with extending pulse length in the brain). To this end, we would conduct MR thermometry during FUS treatments to measure any temperature changes as a result of pulsing, and conduct both H&E for potential red blood cell extravasation from the vasculature and TUNEL staining to assess for potential apoptotic responses as indicators of tissue damage. If altered pulse length results in significant improvements in transfection efficiency, the potential therapeutic applications of our sonoselective approach would expand significantly.

6.2 Mechanistic Evaluation of Sonoselective Transfection

The sonoselective transfection approach detailed in Chapter 3 is described in terms of the cell types transfected and the transcriptomic effects of very low-pressure FUS, but the

precise mechanisms permitting endothelial transfection in the absence of detectable BBB opening are not described. Achieving a better understanding of the mechanisms of sonoselective transfection could inform potential modifications of the approach to augment transfection magnitude or efficiency. Previously, FUS in conjunction with MBs has been demonstrated to induce cell membrane deformation and sonoporation(292), generate shear stress against cell membranes(198, 199), disrupt endothelial tight junctions(72, 293), and increase transcellular uptake through vesicular transport(73, 201). Based on the lack of Evans Blue dye extravasation or MRI contrast enhancement observed following treatment with 0.1 MPa FUS, we hypothesized that our sonoselective transfection regime does not disrupt tight junctions or increase transcellular transport, but does result in some degree of endothelial membrane disruption or sonoporation to permit uptake of the circulating reporter plasmid. However, it is possible that BBB disruption (or transcellular transport across the brain endothelial cells) did in fact occur at this low pressure, but on a scale that could not be detected by our methods.

In order to better address the questions of the mechanisms at play during sonoselective transfection, future studies could be conducted to investigate these different processes. Immunohistochemical staining and high-power confocal microscopy to examine claudin-5, occludin, and ZO-1 expression and localization at a number of acute timepoints following 0.1 MPa FUS would reveal any possible tight junction disruption that may occur. Additional staining for caveolin-1 and vesicle-associated membrane proteins (VAMPs) could provide information about vesicular transport by BBB endothelial cells, as well. We could also deliver fluorescently-labeled dextrans of different sizes with our sonoselective regime, to determine potential size limitations of transport through these possible tight junctional disruptions or vesicle transports. While these findings may not directly impact the potential therapeutic applications of sonoselective transfection, they would contribute to the wider understanding of the mechanisms

and safety of FUS-mediated gene delivery, especially as the field at large experiments with greater variations on the commonly-used pulsing parameters.

6.3 Sonoselective Delivery of a Therapeutic Plasmid to the Cerebral Endothelium in the Context of Ischemic Stroke

The experiments detailed in Chapter 3 focus on proof-of-concept studies delivering a reporter transgene to the vasculature of the brain. We believe that this delivery regime has potential applications in a number of pathologies, if a therapeutic plasmid were to be delivered instead of a reporter. One pathology of particular interest for this approach is ischemic stroke. Following ischemic injury and reperfusion, the infarcted brain tissue is characterized by instability and extensive inflammatory responses(180–183). Given our findings in Chapter 3 demonstrating the inflammatory and immune response to BBB-opening FUS treatments(123), as well as other evidence in the literature for an acute sterile inflammatory response following FUS-mediated BBB opening(87, 173, 174), sonoselective transfection, which does not further disrupt the BBB structure and does not induce such inflammation, is an attractive therapeutic approach for stroke.

In preliminary studies, we have demonstrated in a rodent model of middle cerebral artery occlusion (which recapitulates several features of human ischemic stroke) that there is sufficient perfusion of MBs through the infarct to permit FUS activation and BBB disruption within the stroked brain tissue. Therefore, we hypothesize that the sonoselective transfection approach is feasible for endothelial gene delivery in the infarct, though the precise FUS pulsing parameters may need to modified slightly to reflect the differences in mechanical properties in the ischemic tissue(294). Following this parameter optimization, we could deliver any of a number of potentially therapeutic plasmids to the vasculature after stroke. The endothelial cell signaling

model developed in Chapter 5 could provide a number of candidate genes to deliver, based on what nodes in the model, when over-expressed, result in improvements in stroke metrics of interest (such as increased tight junctional integrity, increased nitric oxide production, and reduced apoptosis). Following delivery of a therapeutic plasmid with sonoselective FUS, we could assess a number of metrics of recovery and reperfusion, including infarct volume (through tetrazolium chloride staining), apoptosis (through TUNEL staining), BBB integrity (through Evans Blue extravasation studies), and overall blood flow (through laser doppler perfusion imaging). Should sonoselective transfection of a therapeutic plasmid provide measurable improvement in recovery in a rodent model of ischemic injury, future studies could explore adapting the approach to larger animal models.

6.4 Sonoselective Delivery of a CRISPR-Cas9 Gene Editing Plasmid to the Cerebral Endothelium

In addition to transient gene therapy for acute disease conditions such as ischemic stroke, we believe that the sonoselective transfection approach detailed in Chapter 3 of this dissertation could prove useful in the treatment of chronic genetic conditions. The therapeutic goals for such conditions would likely require some sort of permanent change to gene expression, either through the use of viral vectors or editing of chromosomal DNA. One attractive potential method would be to use our sonoselective FUS protocol to deliver a plasmid encoding a CRISPR-Cas9 gene editing system. Such a system could, upon transfection into the cerebral endothelium, produce lasting changes in the genetic code to ease or even reverse a disease pathology.

One genetic pathology of interest that may prove amenable to such a treatment approach is GLUT1 deficiency syndrome. The GLUT1 protein is responsible for transporting

glucose from the systemic circulation into the brain to promote normal metabolic activities. In the case of GLUT1 deficiency syndrome, a sporadic mutation or autosomal recessive inheritance pattern results in haploinsufficiency(295, 296). This can cause a range of symptoms including seizures, ataxia, microcephaly, and developmental delays. CRISPR-based gene editing approaches, which utilize an endonuclease under the direction of specific guide RNA to generate double- or single-stranded breaks in the DNA to permit insertions, deletions, or mutations at target locations(297, 298), have seen a tremendous increase in interest and funding in the past decade. A CRISPR plasmid encoding the Cas9 endonuclease as well as targeted guide RNAs could provide a method to correct the mutated GLUT1 gene to restore normal glucose transport.

We have already begun conducting preliminary trials in vitro of 10 different CRISPR plasmids engineered to target the GLUT1 gene. As an initial proof of concept, we have designed plasmids that will induce a double stranded break in the gene to knock out expression. These constructs will be tested for efficacy first in in vitro studies of human and mouse brain endothelial cells. The plasmids will be delivered via electroporation. Each plasmid has been designed with a fluorescent GFP reporter tag, so we can then stain for GLUT1 and use flow cytometry to quantify the differential GLUT1 expression in the GFP-positive population. In vivo trials will be conducted with the top candidates from the in vitro studies, and we will use the sonoselective parameters identified in Chapter 3 to deliver the plasmids. We will then use immunohistochemical staining for GLUT1 expression as well as ^{18}F-FDG PET(299) to quantify total glucose metabolism in the FUS-treated region. Once we have demonstrated reliably the ability to deliver a gene editing system to the cerebral vasculature with FUS, we will modify the CRISPR plasmid to attempt to correct the mutation responsible for GLUT1 insufficiency in a mouse model of the condition(300).

6.5 Characterization of the Temporal Transcriptomic Response of Different Brain Cell Types to FUS

In Chapter 4 of this dissertation, we provide a characterization of the cell-specific transcriptomic responses to different peak-negative pressures of FUS with MBs in the brain at 48 hours after FUS treatment. This allowed us to identify the fraction of different cell types transfected at the different pressures, which revealed a bias towards transfection of cell types typically located closer to the microcirculation. Additionally, the study revealed signatures of a sterile inflammatory response, based on the upregulation of several genes associated with cellular stress and inflammation across multiple cell types. However, based upon the harvest time point of 48 hours after FUS, it is likely we are observing resolving inflammation following an acute increase. Indeed, a 2017 study involving microarray analysis of brain microvessels following FUS-mediated BBB revealed an acute inflammatory response at 6 hours post-FUS that was resolving by 24 hours post-FUS(235). This is consistent with our bulk RNA sequencing findings in Chapter 3 of this thesis, as well(123).

In future studies, we would like to better characterize the temporal dynamics of inflammation onset and resolution at the level of individual cells and cell types. We would like to repeat the general experimental approach described in Chapter 4, but with harvest timepoints more acute than 48 hours. While this timepoint provided maximal reporter transgene expression for FACS sorting of transfected cells, other approaches could be utilized to enrich for FUS-treated cells. One method might be to inject Evans Blue dye at the time of BBB disruption, so that the region of the treated brain with dye extravasation can be identified and selected for digestion and sequencing. Conducting sequencing at 1 hour, 3 hours, 6 hours, 12 hours, and 24 hours post-FUS would provide an incredible quantity of information about how different cell types respond to initial FUS insult as well as the changing landscape of inflammation and

immune cell recruitment that follows, and could inform treatment approaches that either counteract or enhance these responses.

6.6 In Vitro Validation of Computational Signaling Network Model of Brain Endothelial Cells

In Chapter 5, we develop a computational signaling network model of brain endothelial cells. This model, which predicts the influence of different signaling pathways and molecules in a baseline “healthy” state, as well as numerous disease contexts, was validated against the existing literature in terms of input-output relationships. We found a 73% agreement between the model predictions and previous in vitro studies investigating these relationships. However, the literature surrounding brain endothelial cells is shockingly sparse, and a number of the relationships predicted in the model have not yet been studied. In fact, for 16 of the 42 predicted input-output relationships, no studies could be identified in the literature to validate or contradict our predictions. There is clearly an unmet need for further study of these cells and many of their brain-specific signaling pathways.

For this reason, we propose in-house in vitro validation of a number of the missing input-output relationships. By treating human and brain endothelial cells in vitro with the mature and pro-neurotrophin forms of BDNF and NGF, we could gather crucial data to inform the model as well as to support and expand the existing body of research on this cell type. In particular, we are interested in how the various forms of these neurotrophins impact expression and activity of VE cadherin, GLUT1, and p-glycoprotein, which together account for 12 of the 16 missing relationships. A combination of PCR, western blotting, and IHC staining for these outputs following addition of the appropriate neurotrophins into the endothelial cell culture media would permit us to further supplement our validation matrix and build confidence in the model. These

findings could also greatly impact our understanding of the roles of neurotrophic signaling in brain endothelium, an area very poorly characterized in the existing literature but critical for predicting the effects of potential gene therapy.

6.7 Tailoring of Endothelial Cell Signaling Model Parameters to Further Improve Model Accuracy

The computational signaling network reconstructed in Chapter 5 is governed by default parameters for minimal and maximal possible activation of species, as well as time constants and weights of reactions. This is largely due to both the scope of the model and the dearth of reliable literature characterizing these parameters, particularly in comparison to one another. However, as additional data becomes available, either in the literature or through our own in vitro and molecular biology studies, refinement of the model parameters could increase model accuracy. In particular, the reaction weighting could impact model predictions significantly. As we learn more about the relative activity levels of the different pathways involved in the network, perhaps the reaction weights can be adjusted accordingly. Additionally, more consistent and quantitative assessment of the activity change of different input species in the context of different disease states could allow for a more accurate recapitulation of the signaling that takes place in those pathologies. Lastly, in order to incorporate temporal dynamics into the model, the time constants for different reactions can be adjusted, either on an individual level if available data permits, or following basic simplifications utilized in previous such models, wherein time constants were scaled to an order of magnitude appropriate for the type of molecule (mRNA, protein, process, etc)(263).

6.8 Simulation of Different FUS Regimes in Brain Endothelial Cell Signaling Model

The signaling network model constructed in Chapter 5 recapitulates a number of brain endothelial cell pathways. In addition, we incorporated a FUS input node based on our single cell transcriptomic findings in Chapter 4 that FUS-mediated BBB opening results in the upregulation of cathepsin D in brain endothelial cells. We recognize, of course, that this is an oversimplification of the diverse effects of FUS and MBs on the vasculature. Additionally, this finding is based on a 48 hour timepoint. Thus, it does not represent the acute effects of FUS on endothelium. For this reason, future studies could be conducted as described in section 6.5 of this chapter, wherein multiple acute timepoints are selected for single cell RNA sequencing. This could provide a more accurate picture of changes in brain endothelial cell signaling immediately after FUS, and how those changes may interact with potential gene therapies.

Additionally, since low-pressure BBB opening is not the only application of FUS relevant to diseases of the central nervous system, it would be useful to collect data following other FUS regimes, such as hyperthermia(301) or histotripsy(302), to be able to simulate these treatments and their effects on endothelial cell signaling as well. The ability to simulate not just different gene therapies or pharmaceutical interventions, but different FUS delivery or treatment methods, would enhance the applicability of the model.

6.9 Summary

All together, the body of work presented here begins to build a platform for the use of FUS-mediated gene delivery to the cerebral vasculature, including computationally-driven predictions of gene therapy effects, and prompts many questions that may drive novel research

into the physiological mechanisms by which FUS and MBs interact with and affect the diverse cells of the brain.

References

1. Wyss-Coray T (2016) Ageing, neurodegeneration and brain rejuvenation. *Nature* 539(7628):180–186.

2. Gitler AD, Dhillon P, Shorter J (2017) Neurodegenerative disease: Models, mechanisms, and a new hope. *DMM Dis Model Mech* 10(5):499–502.

3. Achrol AS, et al. (2019) Brain metastases. *Nat Rev Dis Prim* 5(1). doi:10.1038/s41572-018-0055-y.

4. Ostrom QT, et al. (2014) CBTRUS statistical report: Primary brain and central nervous system tumors diagnosed in the United States in 2007–2011. *Neuro Oncol* 16(Suppl 4):iv1-iv63.

5. Krishnamurthi R V., et al. (2015) Stroke Prevalence, Mortality and Disability-Adjusted Life Years in Adults Aged 20-64 Years in 1990-2013: Data from the Global Burden of Disease 2013 Study. *Neuroepidemiology* 45(3):190–202.

6. Béjot Y, Daubail B, Giroud M (2016) Epidemiology of stroke and transient ischemic attacks: Current knowledge and perspectives. *Rev Neurol (Paris)* 172(1):59–68.

7. Pardridge WM (2005) The blood-brain barrier: bottleneck in brain drug development. *NeuroRx* 2(1):3–14.

8. Daneman R, Prat A (2015) The blood–brain barrier. *Cold Spring Harb Perspect Biol* 7(1). doi:10.1101/cshperspect.a020412.

9. Daneman R (2012) The blood-brain barrier in health and disease. *Ann Neurol* 72(5):648–672.

10. Coomber BL, Stewart PA (1985) Morphometric analysis of CNS microvascular endothelium. *Microvasc Res* 30(1):99–115.

11. Betz AL, Goldstein GW (1978) Polarity of the blood-brain barrier: Neutral amino acid transport into isolated brain capillaries. *Science (80-)* 202(4364):225–226.

12. Betz AL, Firth JA, Goldstein GW (1980) Polarity of the blood-brain barrier: Distribution of enzymes between the luminal and antiluminal membranes of brain capillary endothelial cells. *Brain Res* 192(1):17–28.

13. Furuse M (2010) Molecular basis of the core structure of tight junctions. *Cold Spring Harb Perspect Biol* 2(1). doi:10.1101/cshperspect.a002907.

14. Bauer H-C, Krizbai IA, Bauer H, Traweger A (2014) â€œYou Shall Not Passâ€□â€”tight junctions of the blood brain barrier. *Front Neurosci* 8:392.

15. Löscher W, Potschka H (2005) Drug resistance in brain diseases and the role of drug efflux transporters. *Nat Rev Neurosci* 6(8):591–602.

16. Abbott NJ (2013) Blood-brain barrier structure and function and the challenges for CNS

drug delivery. *J Inherit Metab Dis* 36(3):437–449.

17. Abbott NJ, Rönnbäck L, Hansson E (2006) Astrocyte-endothelial interactions at the blood-brain barrier. *Nat Rev Neurosci* 7(1):41–53.

18. Westphal M, et al. (2003) A phase 3 trial of local chemotherapy with biodegradable carmustine (BCNU) wafers (Gliadel wafers) in patients with primary malignant glioma. *Neuro Oncol* 5(2):79–88.

19. Brem H, et al. (1995) Placebo-controlled trial of safety and efficacy of intraoperative controlled delivery by biodegradable polymers of chemotherapy for recurrent gliomas. *Lancet* 345(8956):1008–1012.

20. Gómez-Chavarín M, et al. (2019) Dopamine Released from TiO 2 Semicrystalline Lattice Implants Attenuates Motor Symptoms in Rats Treated with 6-Hydroxydopamine. *ACS Omega* 4(5):7953–7962.

21. During MJ, et al. (1989) Controlled release of dopamine from a polymeric brain implant: In vivo characterization. *Ann Neurol* 25(4):351–356.

22. Fung LK, Shin M, Tyler B, Brem H, Saltzman WM (1996) Chemotherapeutic drugs released from polymers: Distribution of 1,3-bis(2-chloroethyl)-1-nitrosourea in the rat brain. *Pharm Res* 13(5):671–682.

23. Krewson CE, Klarman ML, Saltzman WM (1995) Distribution of nerve growth factor following direct delivery to brain interstitium. *Brain Res* 680(1–2):196–206.

24. Blasberg RG, Patlak C, Fenstermacher JD (1975) Intrathecal chemotherapy: brain tissue profiles after ventriculocisternal perfusion. *J Pharmacol Exp Ther* 195(1).

25. Billiau A, et al. (1981) Tissue distribution of human interferons after exogenous administration in rabbits, monkeys, and mice. *Arch Virol* 68(1):19–25.

26. CHRISTY NP, FISHMAN RA (1961) Studies of the blood-cerebrospinal fluid barrier to cortisol in the dog. *J Clin Invest* 40(11):1997–2006.

27. Bobo RH, et al. (1994) Convection-enhanced delivery of macromolecules in the brain. *Proc Natl Acad Sci* 91(6):2076–2080.

28. Lonser RR, Sarntinoranont M, Morrison PF, Oldfield EH (2015) Convection-enhanced delivery to the central nervous system. *J Neurosurg* 122(3):697–706.

29. Gasmi M, et al. (2007) AAV2-mediated delivery of human neurturin to the rat nigrostriatal system: Long-term efficacy and tolerability of CERE-120 for Parkinson's disease. *Neurobiol Dis* 27(1):67–76.

30. Marks WJ, et al. (2008) Safety and tolerability of intraputaminal delivery of CERE-120 (adeno-associated virus serotype 2-neurturin) to patients with idiopathic Parkinson's disease: an open-label, phase I trial. *Lancet Neurol* 7(5):400–408.

31. Zünkeler B, et al. (1996) Quantification and pharmacokinetics of blood-brain barrier

disruption in humans. *J Neurosurg* 85(6):1056–1065.

32. Salahuddin TS, Johansson BB, Kalimo H, Olsson Y (1988) Structural changes in the rat brain after carotid infusions of hyperosmolar solutions - An electron microscopic study. *Acta Neuropathol* 77(1):5–13.

33. Lossinsky AS, Vorbrodt AW, Wisniewski HM (1995) Scanning and transmission electron microscopic studies of microvascular pathology in the osmotically impaired blood-brain barrier. *J Neurocytol* 24(10):795–806.

34. Doolittle ND, Petrillo A, Bell S, Cummings P, Eriksen S (1998) Blood-brain barrier disruption for the treatment of malignant brain tumors: The National Program. *J Neurosci Nurs* 30(2):81–90.

35. Emerich DF, Dean RL, Osborn C, Bartus RT (2001) The development of the bradykinin agonist labradimil as a means to increase the permeability of the blood-brain barrier: From concept to clinical evaluation. *Clin Pharmacokinet* 40(2):105–123.

36. Bartus RT, et al. (1996) Permeability of the blood brain barrier by the bradykinin agonist, RMP-7: Evidence for a sensitive, auto-regulated, receptor-mediated system. *Immunopharmacology* (Elsevier B.V.), pp 270–278.

37. Matsukado K, Sugita M, Black KL (1998) Intracarotid low dose bradykinin infusion selectively increases tumor permeability through activation of bradykinin B2 receptors in malignant gliomas. *Brain Res* 792(1):10–15.

38. Prados MD, et al. (2003) A randomized, double-blind, placebo-controlled, phase 2 study of RMP-7 in combination with carboplatin administered intravenously for the treatment of recurrent malignant glioma. *Neuro Oncol* 5(2):96–103.

39. Kristensson K, Olsson Y (1971) Uptake of exogenous proteins in mouse olfactory cells. *Acta Neuropathol* 19(2):145–154.

40. Rezai AR, et al. (2020) Noninvasive hippocampal blood−brain barrier opening in Alzheimer's disease with focused ultrasound. *Proc Natl Acad Sci U S A* 117(17):9180–9182.

41. Abrahao A, et al. (2019) First-in-human trial of blood–brain barrier opening in amyotrophic lateral sclerosis using MR-guided focused ultrasound. *Nat Commun* 10(1):1–9.

42. Chen K-T, et al. (2020) Neuronavigation-guided focused ultrasound (NaviFUS) for transcranial blood-brain barrier opening in recurrent glioblastoma patients: clinical trial protocol. *Ann Transl Med* 8(11):673–673.

43. Abramowicz JS (2021) Obstetric ultrasound: Where are we and where are we going? *Ultrasonography* 40(1):57–74.

44. Christian E, Yu C, Apuzzo MLJ (2014) Focused ultrasound: Relevant history and prospects for the addition of mechanical energy to the neurosurgical armamentarium. *World Neurosurg* 82(3):354–365.

45. Cline HE, et al. (1992) Mr-guided focused ultrasound surgery. *J Comput Assist Tomogr* 16(6):965–986.

46. Hynynen K, McDannold N, Vykhodtseva N, Jolesz FA (2001) Noninvasive MR Imaging–guided Focal Opening of the Blood-Brain Barrier in Rabbits. *Radiology* 220(3):640–646.

47. Timbie KF, Mead BP, Price RJ (2015) Drug and gene delivery across the blood-brain barrier with focused ultrasound. *J Control Release* 219:61–75.

48. Wei K, et al. (1997) Interactions between microbubbles and ultrasound: in vitro and in vivo observations. *J Am Coll Cardiol* 29(5):1081–8.

49. Wei K, et al. (1998) Quantification of myocardial blood flow with ultrasound-induced destruction of microbubbles administered as a constant venous infusion. *Circulation* 97(5):473–83.

50. Ay T, et al. (2001) Destruction of contrast microbubbles by ultrasound: effects on myocardial function, coronary perfusion pressure, and microvascular integrity. *Circulation* 104(4):461–6.

51. Li P, Cao L, Dou C-Y, Armstrong WF, Miller D (2003) Impact of myocardial contrast echocardiography on vascular permeability: an in vivo dose response study of delivery mode, pressure amplitude and contrast dose. *Ultrasound Med Biol* 29(9):1341–9.

52. Skyba DM, Price RJ, Linka AZ, Skalak TC, Kaul S (1998) Direct in vivo visualization of intravascular destruction of microbubbles by ultrasound and its local effects on tissue. *Circulation* 98(4):290–3.

53. Price RJ, Skyba DM, Kaul S, Skalak TC (1998) Delivery of Colloidal Particles and Red Blood Cells to Tissue Through Microvessel Ruptures Created by Targeted Microbubble Destruction With Ultrasound. *Circulation* 98(13):1264–1267.

54. McDannold N, Vykhodtseva N, Raymond S, Jolesz FA, Hynynen K (2005) MRI-guided targeted blood-brain barrier disruption with focused ultrasound: Histological findings in rabbits. *Ultrasound Med Biol* 31(11):1527–1537.

55. MILLER D (2007) Overview of experimental studies of biological effects of medical ultrasound caused by gas body activation and inertial cavitation. *Prog Biophys Mol Biol* 93(1–3):314–330.

56. Helfield B, Chen X, Watkins SC, Villanueva FS (2016) Biophysical insight into mechanisms of sonoporation. *Proc Natl Acad Sci* 113(36):9983–9988.

57. Chen W-S, Brayman AA, Matula TJ, Crum LA, Miller MW (2003) The pulse length-dependence of inertial cavitation dose and hemolysis. *Ultrasound Med Biol* 29(5):739–48.

58. Chen W-S, Brayman AA, Matula TJ, Crum LA (2003) Inertial cavitation dose and hemolysis produced in vitro with or without Optison. *Ultrasound Med Biol* 29(5):725–37.

59. Dalecki D, et al. (1997) Hemolysis in vivo from exposure to pulsed ultrasound. *Ultrasound Med Biol* 23(2):307–13.

60. Poliachik SL, et al. (1999) Effect of high-intensity focused ultrasound on whole blood with and without microbubble contrast agent. *Ultrasound Med Biol* 25(6):991–8.

61. Raymond SB, Skoch J, Hynynen K, Bacskai BJ (2007) Multiphoton Imaging of Ultrasound/Optison Mediated Cerebrovascular Effects *in vivo*. *J Cereb Blood Flow Metab* 27(2):393–403.

62. Basta G, et al. (2003) In vitro modulation of intracellular oxidative stress of endothelial cells by diagnostic cardiac ultrasound. *Cardiovasc Res* 58(1):156–61.

63. Bertuglia S, Giusti A, Picano E (2004) Effects of diagnostic cardiac ultrasound on oxygen free radical production and microvascular perfusion during ischemia reperfusion. *Ultrasound Med Biol* 30(4):549–557.

64. Kondo T, Misík V, Riesz P (1998) Effect of gas-containing microspheres and echo contrast agents on free radical formation by ultrasound. *Free Radic Biol Med* 25(4–5):605–12.

65. Stride E, Saffari N (2004) The potential for thermal damage posed by microbubble ultrasound contrast agents. *Ultrasonics* 42(1–9):907–13.

66. Santos MA, Wu S-K, Li Z, Goertz DE, Hynynen K (2018) Microbubble-assisted MRI-guided focused ultrasound for hyperthermia at reduced power levels. *Int J Hyperth* 35(1):599–611.

67. Klotz AR, Lindvere L, Stefanovic B, Hynynen K (2010) Temperature change near microbubbles within a capillary network during focused ultrasound. *Phys Med Biol* 55(6):1549–1561.

68. Collis J, et al. (2010) Cavitation microstreaming and stress fields created by microbubbles. *Ultrasonics* 50(2):273–279.

69. Kooiman K, Vos HJ, Versluis M, de Jong N (2014) Acoustic behavior of microbubbles and implications for drug delivery. *Adv Drug Deliv Rev* 72:28–48.

70. Kim J, et al. (2017) Intravascular forward-looking ultrasound transducers for microbubble-mediated sonothrombolysis. *Sci Rep* 7(1):3454.

71. Chen H, Brayman AA, Kreider W, Bailey MR, Matula TJ (2011) Observations of Translation and Jetting of Ultrasound-Activated Microbubbles in Mesenteric Microvessels. *Ultrasound Med Biol* 37(12):2139–2148.

72. Sheikov N, McDannold N, Sharma S, Hynynen K (2008) Effect of focused ultrasound applied with an ultrasound contrast agent on the tight junctional integrity of the brain microvascular endothelium. *Ultrasound Med Biol* 34(7):1093–104.

73. Deng J, et al. (2012) The role of caveolin-1 in blood-brain barrier disruption induced by focused ultrasound combined with microbubbles. *J Mol Neurosci* 46(3):677–687.

74. Meijering BDM, et al. (2009) Ultrasound and Microbubble-Targeted Delivery of Macromolecules Is Regulated by Induction of Endocytosis and Pore Formation. *Circ Res*

104(5):679–687.

75. van Rooij T, et al. (2016) Viability of endothelial cells after ultrasound-mediated sonoporation: Influence of targeting, oscillation, and displacement of microbubbles. *J Control Release* 238:197–211.

76. Nhan T, et al. (2013) Drug delivery to the brain by focused ultrasound induced blood–brain barrier disruption: Quantitative evaluation of enhanced permeability of cerebral vasculature using two-photon microscopy. *J Control Release* 172(1):274–280.

77. Chen H, Konofagou EE (2014) The size of blood-brain barrier opening induced by focused ultrasound is dictated by the acoustic pressure. *J Cereb Blood Flow Metab* 34(7):1197–1204.

78. BURTON AC (1954) Relation of structure to function of the tissues of the wall of blood vessels. *Physiol Rev* 34(4):619–642.

79. Cho EE, Drazic J, Ganguly M, Stefanovic B, Hynynen K (2011) Two-photon fluorescence microscopy study of cerebrovascular dynamics in ultrasound-induced blood-brain barrier opening. *J Cereb Blood Flow Metab* 31(9):1852–1862.

80. Yang Y, Li Q, Guo X, Tu J, Zhang D (2020) Mechanisms underlying sonoporation: Interaction between microbubbles and cells. *Ultrason Sonochem* 67:105096.

81. Sheikov N, McDannold N, Vykhodtseva N, Jolesz F, Hynynen K (2004) Cellular mechanisms of the blood-brain barrier opening induced by ultrasound in presence of microbubbles. *Ultrasound Med Biol* 30(7):979–989.

82. Sheikov N, et al. (2006) Brain arterioles show more active vesicular transport of blood-borne tracer molecules than capillaries and venules after focused ultrasound-evoked opening of the blood-brain barrier. *Ultrasound Med Biol* 32(9):1399–1409.

83. Bader KB, Holland CK (2013) Gauging the likelihood of stable cavitation from ultrasound contrast agents. *Phys Med Biol* 58(1):127–144.

84. Apfel RE (1982) Acoustic cavitation: A possible consequence of biomedical uses of ultrasound. *Br J Cancer* 45(Suppl. 5):140–146.

85. McDannold N, Vykhodtseva N, Hynynen K (2006) Targeted disruption of the blood–brain barrier with focused ultrasound: association with cavitation activity. *Phys Med Biol* 51(4):793–807.

86. Samuel S, Cooper MA, Bull JL, Fowlkes JB, Miller DL (2009) An ex vivo Study of the Correlation Between Acoustic Emission and Microvascular Damage. *Ultrasound Med Biol* 35(9):1574–1586.

87. Kovacs ZI, et al. (2017) Disrupting the blood-brain barrier by focused ultrasound induces sterile inflammation. *Proc Natl Acad Sci U S A* 114(1):E75–E84.

88. McMahon D, Hynynen K (2017) Acute Inflammatory Response Following Increased Blood-Brain Barrier Permeability Induced by Focused Ultrasound is Dependent on

Microbubble Dose. *Theranostics* 7(16):3989–4000.

89. McDannold N, Vykhodtseva N, Hynynen K (2006) Targeted disruption of the blood–brain barrier with focused ultrasound: association with cavitation activity. *Phys Med Biol* 51(4):793–807.

90. Tung Y-S, et al. (2010) In vivo transcranial cavitation threshold detection during ultrasound-induced blood-brain barrier opening in mice. *Phys Med Biol* 55(20):6141–55.

91. Apfel RE (1991) Acoustic microcavitation: Its active and passive acoustic detection. *J Acoust Soc Am* 90(3):1515–1526.

92. Tung Y-S, et al. (2010) *In vivo* transcranial cavitation threshold detection during ultrasound-induced blood–brain barrier opening in mice. *Phys Med Biol* 55(20):6141–6155.

93. Ilyichev VI, Koretz VL, Melnikov NP (1989) Spectral characteristics of acoustic cavitation. *Ultrasonics* 27(6):357–361.

94. O'Reilly MA, Hynynen K (2012) Blood-brain barrier: real-time feedback-controlled focused ultrasound disruption by using an acoustic emissions-based controller. *Radiology* 263(1):96–106.

95. Arvanitis CD, Livingstone MS, Vykhodtseva N, McDannold N (2012) Controlled Ultrasound-Induced Blood-Brain Barrier Disruption Using Passive Acoustic Emissions Monitoring. *PLoS One* 7(9):45783.

96. McMahon D, Oakden W, Hynynen K (2020) Investigating the effects of dexamethasone on blood-brain barrier permeability and inflammatory response following focused ultrasound and microbubble exposure. *Theranostics* 10(4):1604–1618.

97. Xu S, et al. (2019) Correlation Between Brain Tissue Damage and Inertial Cavitation Dose Quantified Using Passive Cavitation Imaging. *Ultrasound Med Biol* 45(10):2758–2766.

98. Nilsson P, et al. (2010) Gene therapy in Alzheimer's disease - potential for disease modification. *J Cell Mol Med* 14(4):741–757.

99. Coune PG, Schneider BL, Aebischer P (2012) Parkinson's disease: Gene therapies. *Cold Spring Harb Perspect Med* 2(4). doi:10.1101/cshperspect.a009431.

100. G. Castro M, et al. (2011) Gene Therapy and Targeted Toxins for Glioma. *Curr Gene Ther* 11(3):155–180.

101. Choong CJ, Baba K, Mochizuki H (2016) Gene therapy for neurological disorders. *Expert Opin Biol Ther* 16(2):143–159.

102. Cappella M, Ciotti C, Cohen-Tannoudji M, Biferi MG (2019) Gene therapy for ALS-A perspective. *Int J Mol Sci* 20(18). doi:10.3390/ijms20184388.

103. Hsu PH, et al. (2013) Noninvasive and Targeted Gene Delivery into the Brain Using

Microbubble-Facilitated Focused Ultrasound. *PLoS One* 8(2):e57682.

104. Alonso A, et al. (2013) Focal delivery of AAV2/1-transgenes into the rat brain by localized ultrasound-induced BBB opening. *Mol Ther - Nucleic Acids* 2(2):e73.

105. Stavarache MA, et al. (2018) Safe and stable noninvasive focal gene delivery to the mammalian brain following focused ultrasound. *J Neurosurg* 130(3):1–10.

106. Thévenot E, et al. (2012) Targeted Delivery of Self-Complementary Adeno-Associated Virus Serotype 9 to the Brain, Using Magnetic Resonance Imaging-Guided Focused Ultrasound. *Hum Gene Ther* 23(11):1144–1155.

107. Touahri Y, et al. (2020) Focused ultrasound as a novel strategy for noninvasive gene delivery to retinal Müller glia. *Theranostics* 10(7):2982–2999.

108. Weber-Adrian D, et al. (2015) Gene delivery to the spinal cord using MRI-guided focused ultrasound. *Gene Ther* 22(7):568–577.

109. Wang S, Olumolade OO, Sun T, Samiotaki G, Konofagou EE (2015) Noninvasive, neuron-specific gene therapy can be facilitated by focused ultrasound and recombinant adeno-associated virus. *Gene Ther* 22(1):104–110.

110. Karakatsani ME, et al. (2019) Amelioration of the nigrostriatal pathway facilitated by ultrasound-mediated neurotrophic delivery in early Parkinson's disease. *J Control Release* 303:289–301.

111. Wang S, et al. (2017) Non-invasive, Focused Ultrasound-Facilitated Gene Delivery for Optogenetics. *Sci Rep* 7. doi:10.1038/srep39955.

112. Xhima K, Nabbouh F, Hynynen K, Aubert I, Tandon A (2018) Noninvasive delivery of an α-synuclein gene silencing vector with magnetic resonance-guided focused ultrasound. *Mov Disord* 33(10):1567–1579.

113. Lin CY, et al. (2015) Focused ultrasound-induced blood-brain barrier opening for non-viral, non-invasive, and targeted gene delivery. *J Control Release* 212:1–9.

114. Lin CY, et al. (2016) Non-invasive, neuron-specific gene therapy by focused ultrasound-induced blood-brain barrier opening in Parkinson's disease mouse model. *J Control Release* 235:72–81.

115. Lin CY, et al. (2019) Focused ultrasound-induced blood brain-barrier opening enhanced vascular permeability for GDNF delivery in Huntington's disease mouse model. *Brain Stimul* 12(5):1143–1150.

116. Zhao G, et al. (2018) Targeted shRNA-loaded liposome complex combined with focused ultrasound for blood brain barrier disruption and suppressing glioma growth. *Cancer Lett* 418:147–158.

117. Nomikou N, Tiwari P, Trehan T, Gulati K, McHale AP (2012) Studies on neutral, cationic and biotinylated cationic microbubbles in enhancing ultrasound-mediated gene delivery in vitro and in vivo. *Acta Biomater* 8(3):1273–1280.

118. Burke CW, et al. (2011) Covalently linking poly(lactic-co-glycolic acid) nanoparticles to microbubbles before intravenous injection improves their ultrasound-targeted delivery to skeletal muscle. *Small* 7(9):1227–35.

119. Wang DS, et al. (2012) Cationic versus neutral microbubbles for ultrasound-mediated gene delivery in cancer. *Radiology* 264(3):721–32.

120. Huang Q, et al. (2012) Targeted gene delivery to the mouse brain by MRI-guided focused ultrasound-induced blood-brain barrier disruption. *Exp Neurol* 233(1):350–356.

121. Fan CH, et al. (2016) Noninvasive, Targeted, and Non-Viral Ultrasound-Mediated GDNF-Plasmid Delivery for Treatment of Parkinson's Disease. *Sci Rep* 6:19579–19579.

122. Huang Q, et al. (2012) Effective Gene Transfer into Central Nervous System Following Ultrasound-Microbubbles-Induced Opening of the Blood-Brain Barrier. *Ultrasound Med Biol* 38(7):1234–1243.

123. Gorick CM, et al. (2020) Sonoselective transfection of cerebral vasculature without blood–brain barrier disruption. *Proc Natl Acad Sci* 117(11):5644–5654.

124. Mead BP, et al. (2016) Targeted gene transfer to the brain via the delivery of brain-penetrating DNA nanoparticles with focused ultrasound. *J Control Release* 223:109–117.

125. Mead BP, et al. (2017) Novel Focused Ultrasound Gene Therapy Approach Noninvasively Restores Dopaminergic Neuron Function in a Rat Parkinson's Disease Model. *Nano Lett* 17(6):3533–3542.

126. Negron K, et al. (2019) Widespread gene transfer to malignant gliomas with In vitro-to-In vivo correlation. *J Control Release* 303:1–11.

127. Mastorakos P, et al. (2015) Highly PEGylated DNA Nanoparticles Provide Uniform and Widespread Gene Transfer in the Brain. *Adv Healthc Mater* 4(7):1023–1033.

128. Guzik A, Bushnell C (2017) Stroke Epidemiology and Risk Factor Management. *Contin Lifelong Learn Neurol* 23(1):15–39.

129. Hankey GJ (2017) Stroke. *Lancet* 389(10069):641–654.

130. Vigo D, Thornicroft G, Atun R (2016) Estimating the true global burden of mental illness. *The Lancet Psychiatry* 3(2):171–178.

131. McNeill KA (2016) Epidemiology of Brain Tumors. *Neurol Clin* 34(4):981–998.

132. Gavrilovic IT, Posner JB (2005) Brain metastases: epidemiology and pathophysiology. *J Neurooncol* 75(1):5–14.

133. Erkkinen MG, Kim M-O, Geschwind MD (2018) Clinical Neurology and Epidemiology of the Major Neurodegenerative Diseases. *Cold Spring Harb Perspect Biol* 10(4):a033118.

134. Kitchen Andren KA, Gabel NM, Stelmokas J, Rich AM, Bieliauskas LA (2017) Population Base Rates and Disease Course of Common Psychiatric and Neurodegenerative Disorders. *Neuropsychol Rev* 27(3):284–301.

135. McCurdy VJ, et al. (2015) Widespread correction of central nervous system disease after intracranial gene therapy in a feline model of Sandhoff disease. *Gene Ther* 22(2):181–189.

136. Kantor B, McCown T, Leone P, Gray SJ (2014) Clinical Applications Involving CNS Gene Transfer. *Advances in Genetics*, pp 71–124.

137. Tereshchenko J, Maddalena A, Bähr M, Kügler S (2014) Pharmacologically controlled, discontinuous GDNF gene therapy restores motor function in a rat model of Parkinson's disease. *Neurobiol Dis* 65:35–42.

138. Bjorklund T, Kordower JH (2010) Gene therapy for Parkinson's disease. *Mov Disord* 25(S1):S161–S173.

139. Murphy SR, et al. (2013) Acat1 Knockdown Gene Therapy Decreases Amyloid-β in a Mouse Model of Alzheimer's Disease. *Mol Ther* 21(8):1497–1506.

140. Berry M, Barrett L, Seymour L, Baird A, Logan A (2001) Gene therapy for central nervous system repair. *Curr Opin Mol Ther* 3(4):338–49.

141. Pardridge WM (2012) Drug transport across the blood-brain barrier. *J Cereb Blood Flow Metab* 32(11):1959–1972.

142. Hawkins BT, Davis TP (2005) The Blood-Brain Barrier/Neurovascular Unit in Health and Disease. *Pharmacol Rev* 57(2):173–185.

143. Nance E, et al. (2014) Non-invasive delivery of stealth, brain-penetrating nanoparticles across the blood−brain barrier using MRI-guided focused ultrasound. *J Control Release* 189:123–132.

144. Timbie KF, Mead BP, Price RJ (2015) Drug and gene delivery across the blood-brain barrier with focused ultrasound. *J Control Release* 219:61–75.

145. Mead BP, et al. (2016) Targeted gene transfer to the brain via the delivery of brain-penetrating DNA nanoparticles with focused ultrasound. *J Control Release* 223:109–117.

146. Hynynen K, Jolesz FA (1998) Demonstration of potential noninvasive ultrasound brain therapy through an intact skull. *Ultrasound Med Biol* 24(2):275–83.

147. Sheikov N, McDannold N, Sharma S, Hynynen K (2008) Effect of Focused Ultrasound Applied With an Ultrasound Contrast Agent on the Tight Junctional Integrity of the Brain Microvascular Endothelium. *Ultrasound Med Biol* 34(7):1093–1104.

148. Shang X, Wang P, Liu Y, Zhang Z, Xue Y (2011) Mechanism of Low-Frequency Ultrasound in Opening Blood–Tumor Barrier by Tight Junction. *J Mol Neurosci* 43(3):364–369.

149. Escoffre J-M, Bouakaz A (2018) Mini-review - Biophysical mechanisms of cell membrane sonopermeabilization: Knowns and unknowns. *Langmuir*:acs.langmuir.8b03538.

150. Escoffre J-M, Zeghimi A, Novell A, Bouakaz A (2013) In-vivo gene delivery by

sonoporation: recent progress and prospects. *Curr Gene Ther* 13(1):2–14.

151. Vlachos F, Tung Y-S, Konofagou EE (2010) Permeability assessment of the focused ultrasound-induced blood–brain barrier opening using dynamic contrast-enhanced MRI. *Phys Med Biol* 55(18):5451–5466.

152. Tung Y-S, Vlachos F, Feshitan JA, Borden MA, Konofagou EE (2011) The mechanism of interaction between focused ultrasound and microbubbles in blood-brain barrier opening in mice. *J Acoust Soc Am* 130(5):3059–67.

153. Meairs S (2015) Facilitation of Drug Transport across the Blood–Brain Barrier with Ultrasound and Microbubbles. *Pharmaceutics* 7(3):275.

154. Jordão JF, et al. (2013) Amyloid-β plaque reduction, endogenous antibody delivery and glial activation by brain-targeted, transcranial focused ultrasound. *Exp Neurol* 248:16–29.

155. Alecou T, Giannakou M, Damianou C (2017) Amyloid β Plaque Reduction With Antibodies Crossing the Blood-Brain Barrier, Which Was Opened in 3 Sessions of Focused Ultrasound in a Rabbit Model. *J Ultrasound Med* 36(11):2257–2270.

156. Kobus T, Zervantonakis IK, Zhang Y, McDannold NJ (2016) Growth inhibition in a brain metastasis model by antibody delivery using focused ultrasound-mediated blood-brain barrier disruption. *J Control Release* 238:281–288.

157. Baseri B, et al. (2012) Activation of signaling pathways following localized delivery of systemically administered neurotrophic factors across the blood–brain barrier using focused ultrasound and microbubbles. *Phys Med Biol* 57(7):N65–N81.

158. Samiotaki G, Acosta C, Wang S, Konofagou EE (2015) Enhanced Delivery and Bioactivity of the Neurturin Neurotrophic Factor through Focused Ultrasound—Mediated Blood—Brain Barrier Opening *in vivo*. *J Cereb Blood Flow Metab* 35(4):611–622.

159. Timbie KF, et al. (2017) MR image-guided delivery of cisplatin-loaded brain-penetrating nanoparticles to invasive glioma with focused ultrasound. *J Control Release* 263:120–131.

160. Burgess A, et al. (2011) Targeted Delivery of Neural Stem Cells to the Brain Using MRI-Guided Focused Ultrasound to Disrupt the Blood-Brain Barrier. *PLoS One* 6(11):e27877.

161. Shen W-B, et al. (2017) Magnetic Enhancement of Stem Cell–Targeted Delivery into the Brain Following MR-Guided Focused Ultrasound for Opening the Blood–Brain Barrier. *Cell Transplant* 26(7):1235–1246.

162. Fan C-H, et al. (2016) Folate-conjugated gene-carrying microbubbles with focused ultrasound for concurrent blood-brain barrier opening and local gene delivery. *Biomaterials* 106:46–57.

163. Nafee N, Gouda N (2017) Nucleic Acids-based Nanotherapeutics Crossing the Blood Brain Barrier. *Curr Gene Ther* 17(2):154–169.

164. Sirsi SR, Borden MA (2014) State-of-the-art materials for ultrasound-triggered drug

delivery. *Adv Drug Deliv Rev* 72:3–14.

165. Sirsi SR, et al. (2012) Polyplex-microbubble hybrids for ultrasound-guided plasmid DNA delivery to solid tumors. *J Control Release* 157(2):224–234.

166. Borden MA, Caskey CF, Little E, Gillies RJ, Ferrara KW (2007) DNA and Polylysine Adsorption and Multilayer Construction onto Cationic Lipid-Coated Microbubbles. *Langmuir* 23(18):9401–9408.

167. Kopechek JA, et al. (2016) Cardiac Gene Expression Knockdown Using Small Inhibitory RNA-Loaded Microbubbles and Ultrasound. *PLoS One* 11(7):e0159751.

168. Villanueva FS (2009) Ultrasound Mediated Destruction of DNA-Loaded Microbubbles for Enhancement of Cell-Based Therapies. *JACC Cardiovasc Imaging* 2(7):880–882.

169. Leinenga G, Götz J (2015) Scanning ultrasound removes amyloid-b and restores memory in an Alzheimer's disease mouse model. *Sci Transl Med* 7(278). doi:10.1126/scitranslmed.aaa2512.

170. Lipsman N, et al. (2018) Blood–brain barrier opening in Alzheimer's disease using MR-guided focused ultrasound. *Nat Commun* 9(1):2336.

171. Mainprize T, et al. (2019) Blood-Brain Barrier Opening in Primary Brain Tumors with Non-invasive MR-Guided Focused Ultrasound: A Clinical Safety and Feasibility Study. *Sci Rep* 9(1):321.

172. Kovacs ZI, et al. (2017) Disrupting the blood-brain barrier by focused ultrasound induces sterile inflammation. *Proc Natl Acad Sci U S A* 114(1):E75–E84.

173. Kovacs ZI, et al. (2018) MRI and histological evaluation of pulsed focused ultrasound and microbubbles treatment effects in the brain. *Theranostics* 8(17):4837–4855.

174. McMahon D, Hynynen K (2017) Acute Inflammatory Response Following Increased Blood-Brain Barrier Permeability Induced by Focused Ultrasound is Dependent on Microbubble Dose. *Theranostics* 7(16):3989–4000.

175. Chen PY, Wei KC, Liu HL (2015) Neural immune modulation and immunotherapy assisted by focused ultrasound induced blood-brain barrier opening. *Hum Vaccines Immunother* 11(11):2682–2687.

176. Chen PY, et al. (2015) Focused ultrasound-induced blood-brain barrier opening to enhance interleukin-12 delivery for brain tumor immunotherapy: A preclinical feasibility study. *J Transl Med* 13(1). doi:10.1186/s12967-015-0451-y.

177. Scarcelli T, et al. (2014) Stimulation of hippocampal neurogenesis by transcranial focused ultrasound and microbubbles in adult mice. *Brain Stimul* 7(2):304–307.

178. Mooney SJ, et al. (2016) Focused ultrasound-induced neurogenesis requires an increase in blood-brain barrier permeability. *PLoS One* 11(7). doi:10.1371/journal.pone.0159892.

179. Aryal M, et al. (2017) Effects on P-glycoprotein expression after blood-brain barrier

disruption using focused ultrasound and microbubbles. *PLoS One* 12(1). doi:10.1371/journal.pone.0166061.

180. Deb P, Sharma S, Hassan KM (2010) Pathophysiologic mechanisms of acute ischemic stroke: An overview with emphasis on therapeutic significance beyond thrombolysis. *Pathophysiology* 17(3):197–218.

181. del Zoppo G, et al. (2000) Inflammation and stroke: putative role for cytokines, adhesion molecules and iNOS in brain response to ischemia. *Brain Pathol* 10(1):95–112.

182. Tănăsescu R, et al. (2008) An immunological approach to cerebral ischemia (I). Immune cells and adhesion molecules. *Rom J Intern Med* 46(1):3–8.

183. Jin R, Liu L, Zhang S, Nanda A, Li G (2013) Role of Inflammation and Its Mediators in Acute Ischemic Stroke. *J Cardiovasc Transl Res* 6(5):834–851.

184. Schain M, Kreisl WC (2017) Neuroinflammation in Neurodegenerative Disorders—a Review. *Curr Neurol Neurosci Rep* 17(3):25.

185. Kooiman K, Foppen-Harteveld M, de Jong N (2010) Ultrasound-mediated targeted microbubble sonoporation of endothelial cells. *J Control Release* 148(1):e62–e63.

186. Kooiman K, Foppen-Harteveld M, der Steen AFW van, de Jong N (2011) Sonoporation of endothelial cells by vibrating targeted microbubbles. *J Control Release* 154(1):35–41.

187. Nagel T, Resnick N, Atkinson WJ, Dewey CF, Gimbrone MA (1994) Shear stress selectively upregulates intercellular adhesion molecule-1 expression in cultured human vascular endothelial cells. *J Clin Invest* 94(August):885–891.

188. Hu Y, Wan JMF, Yu ACH (2013) Membrane Perforation and Recovery Dynamics in Microbubble-Mediated Sonoporation. *Ultrasound Med Biol* 39(12):2393–2405.

189. Lentacker I, De Cock I, Deckers R, De Smedt SC, Moonen CTW (2014) Understanding ultrasound induced sonoporation: Definitions and underlying mechanisms. *Adv Drug Deliv Rev* 72:49–64.

190. Li F, et al. (2018) Dynamics and mechanisms of intracellular calcium waves elicited by tandem bubble-induced jetting flow. *Proc Natl Acad Sci U S A* 115(3):E353–E362.

191. Iwanaga K, et al. (2007) Local delivery system of cytotoxic agents to tumors by focused sonoporation. *Cancer Gene Ther* 14(4):354–363.

192. Assmann JC, Körbelin J (2016) Genetic manipulation of brain endothelial cells in vivo. *Biochim Biophys Acta - Mol Basis Dis* 1862(3):381–394.

193. Prandini M-H, et al. (2005) The human VE-cadherin promoter is subjected to organ-specific regulation and is activated in tumour angiogenesis. *Oncogene* 24(18):2992–3001.

194. Claxton S, et al. (2008) Efficient, inducible Cre-recombinase activation in vascular endothelium. *genesis* 46(2):74–80.

195. Park SO, et al. (2008) ALK5- and TGFBR2-independent role of ALK1 in the pathogenesis of hereditary hemorrhagic telangiectasia type 2. *Blood* 111(2):633–42.

196. Bouakaz A, Zeghimi A, Doinikov AA (2016) Sonoporation: Concept and Mechanisms. *Advances in Experimental Medicine and Biology*, pp 175–189.

197. van Wamel A, et al. (2006) Vibrating microbubbles poking individual cells: Drug transfer into cells via sonoporation. *J Control Release* 112(2):149–155.

198. Wu J (2002) Theoretical study on shear stress generated by microstreaming surrounding contrast agents attached to living cells. *Ultrasound Med Biol* 28(1):125–9.

199. Chen C, Gu Y, Tu J, Guo X, Zhang D (2016) Microbubble oscillating in a microvessel filled with viscous fluid: A finite element modeling study. *Ultrasonics* 66:54–64.

200. Hynynen K, McDannold N, Sheikov NA, Jolesz FA, Vykhodtseva N (2005) Local and reversible blood–brain barrier disruption by noninvasive focused ultrasound at frequencies suitable for trans-skull sonications. *Neuroimage* 24(1):12–20.

201. Alonso A (2015) Ultrasound-induced blood-brain barrier opening for drug delivery. *Front Neurol Neurosci* 36:106–115.

202. Boutet A, et al. (2019) The relevance of skull density ratio in selecting candidates for transcranial MR-guided focused ultrasound. *J Neurosurg*:1–7.

203. Mueller JK, Ai L, Bansal P, Legon W (2017) Numerical evaluation of the skull for human neuromodulation with transcranial focused ultrasound. *J Neural Eng* 14(6):66012.

204. Caballero-Insaurriaga J, et al. (2019) Zero TE MRI Applications to Transcranial MR-Guided Focused Ultrasound: Patient Screening and Treatment Efficiency Estimation. *J Magn Reson Imaging*:jmri.26746.

205. O'Reilly MA, Hynynen K (2012) Blood-Brain Barrier: Real-time Feedback-controlled Focused Ultrasound Disruption by Using an Acoustic Emissions–based Controller. *Radiology* 263(1):96–106.

206. Konofagou EE, et al. (2012) Ultrasound-induced blood-brain barrier opening. *Curr Pharm Biotechnol* 13(7):1332–45.

207. Burgess MT, Apostolakis I, Konofagou EE (2018) Power cavitation-guided blood-brain barrier opening with focused ultrasound and microbubbles. *Phys Med Biol* 63(6):65009.

208. Jones RM, et al. (2018) Three-dimensional transcranial microbubble imaging for guiding volumetric ultrasound-mediated blood-brain barrier opening. *Theranostics* 8(11):2909–2926.

209. Carson AR, et al. (2011) Gene therapy of carcinoma using ultrasound-targeted microbubble destruction. *Ultrasound Med Biol* 37(3):393–402.

210. Christiansen JP, French BA, Klibanov AL, Kaul S, Lindner JR (2003) Targeted tissue transfection with ultrasound destruction of plasmid-bearing cationic microbubbles.

Ultrasound Med Biol 29(12):1759–67.

211. Panje CM, et al. (2012) Ultrasound-Mediated Gene Delivery with Cationic Versus Neutral Microbubbles: Effect of DNA and Microbubble Dose on *In Vivo* Transfection Efficiency. *Theranostics* 2(11):1078–1091.

212. Christiansen JP, French BA, Klibanov AL, Kaul S, Lindner JR (2003) Targeted tissue transfection with ultrasound destruction of plasmid-bearing cationic microbubbles. *Ultrasound Med Biol* 29(12):1759–1767.

213. Patro R, Duggal G, Love MI, Irizarry RA, Kingsford C (2017) Salmon provides fast and bias-aware quantification of transcript expression. *Nat Methods* 14(4):417–419.

214. Soneson C, Love MI, Robinson MD (2016) Differential analyses for RNA-seq: transcript-level estimates improve gene-level inferences. *F1000Research* 4:1521.

215. Love MI, Huber W, Anders S (2014) Moderated estimation of fold change and dispersion for RNA-seq data with DESeq2. *Genome Biol* 15(12):550.

216. Liberzon A, et al. (2011) Molecular signatures database (MSigDB) 3.0. *Bioinformatics* 27(12):1739–1740.

217. Sergushichev AA (2016) An algorithm for fast preranked gene set enrichment analysis using cumulative statistic calculation. *bioRxiv*:60012.

218. Butler A, Hoffman P, Smibert P, Papalexi E, Satija R (2018) Integrating single-cell transcriptomic data across different conditions, technologies, and species. *Nat Biotechnol* 36(5):411–420.

219. Franzén O, Gan L-M, Björkegren JLM (2019) PanglaoDB: a web server for exploration of mouse and human single-cell RNA sequencing data. *Database* 2019. doi:10.1093/database/baz046.

220. Finak G, et al. (2015) MAST: a flexible statistical framework for assessing transcriptional changes and characterizing heterogeneity in single-cell RNA sequencing data. *Genome Biol* 16(1):278.

221. Choi JJ, Pernot M, Small SA, Konofagou EE (2007) Noninvasive, transcranial and localized opening of the blood-brain barrier using focused ultrasound in mice. *Ultrasound Med Biol* 33(1):95–104.

222. Aryal M, Vykhodtseva N, Zhang YZ, Park J, McDannold N (2013) Multiple treatments with liposomal doxorubicin and ultrasound-induced disruption of blood-tumor and blood-brain barriers improve outcomes in a rat glioma model. *J Control Release* 169(1–2):103–111.

223. Liu HL, et al. (2010) Blood-brain barrier disruption with focused ultrasound enhances delivery of chemotherapeutic drugs for glioblastoma treatment. *Radiology* 255(2):415–425.

224. McDannold N, et al. (2019) Acoustic feedback enables safe and reliable carboplatin delivery across the blood-brain barrier with a clinical focused ultrasound system and

improves survival in a rat glioma model. *Theranostics* 9(21):6284–6299.

225. Janowicz PW, Leinenga G, Götz J, Nisbet RM (2019) Ultrasound-mediated blood-brain barrier opening enhances delivery of therapeutically relevant formats of a tau-specific antibody. *Sci Rep* 9(1):1–9.

226. Park EJ, Zhang YZ, Vykhodtseva N, McDannold N (2012) Ultrasound-mediated blood-brain/blood-tumor barrier disruption improves outcomes with trastuzumab in a breast cancer brain metastasis model. *J Control Release* 163(3):277–284.

227. Kinoshita M, McDannold N, Jolesz FA, Hynynen K (2006) Noninvasive localized delivery of Herceptin to the mouse brain by MRI-guided focused ultrasound-induced blood-brain barrier disruption. *Proc Natl Acad Sci U S A* 103(31):11719–11723.

228. Stavarache MA, et al. (2019) Safe and stable noninvasive focal gene delivery to the mammalian brain following focused ultrasound. *J Neurosurg* 130(3):989–998.

229. Fan CH, et al. (2016) Noninvasive, Targeted, and Non-Viral Ultrasound-Mediated GDNF-Plasmid Delivery for Treatment of Parkinson's Disease. *Sci Rep* 6(1):1–11.

230. Curley CT, et al. (2020) Augmentation of brain tumor interstitial flow via focused ultrasound promotes brain-penetrating nanoparticle dispersion and transfection. *Sci Adv* 6(18):eaay1344.

231. Mead BP, et al. (2019) Focused Ultrasound Preconditioning for Augmented Nanoparticle Penetration and Efficacy in the Central Nervous System. *Small* 15(49):1903460.

232. Wu F, et al. (2003) A randomised clinical trial of high-intensity focused ultrasound ablation for the treatment of patients with localised breast cancer. *Br J Cancer* 89(12):2227–2233.

233. Hsu P-H, et al. (2013) Noninvasive and Targeted Gene Delivery into the Brain Using Microbubble-Facilitated Focused Ultrasound. *PLoS One* 8(2):e57682.

234. Choi JJ, et al. (2011) Noninvasive and localized blood-brain barrier disruption using focused ultrasound can be achieved at short pulse lengths and low pulse repetition frequencies. *J Cereb Blood Flow Metab* 31(2):725–737.

235. McMahon D, Bendayan R, Hynynen K (2017) Acute effects of focused ultrasound-induced increases in blood-brain barrier permeability on rat microvascular transcriptome. *Sci Rep* 7:45657.

236. Kovacs ZI, et al. (2017) Disrupting the blood–brain barrier by focused ultrasound induces sterile inflammation. *Proc Natl Acad Sci* 114(1):E75–E84.

237. Jia C, et al. (2018) Generation of Reactive Oxygen Species in Heterogeneously Sonoporated Cells by Microbubbles with Single-Pulse Ultrasound. *Ultrasound Med Biol* 44(5):1074–1085.

238. Zhong W, Sit WH, Wan JMF, Yu ACH (2011) Sonoporation induces apoptosis and cell cycle arrest in human promyelocytic leukemia cells. *Ultrasound Med Biol* 37(12):2149–

2159.

239. Bańkowska A, Gacko M, Chyczewska E, Worowska A (1997) Biological and diagnostic role of cathepsin D. *Rocz Akad Med Bialymst* 42 Suppl 1:79–85.

240. Benes P, Vetvicka V, Fusek M (2008) Cathepsin D-Many functions of one aspartic protease. *Crit Rev Oncol Hematol* 68(1):12–28.

241. Cataldo AM, et al. (1995) Gene expression and cellular content of cathepsin D in Alzheimer's disease brain: Evidence for early up-regulation of the endosomal-lysosomal system. *Neuron* 14(3):671–680.

242. Hook GR, et al. (2014) The cysteine protease cathepsin B is a key drug target and cysteine protease inhibitors are potential therapeutics for traumatic brain injury. *J Neurotrauma* 31(5):515–529.

243. Luo C-L, et al. (2010) Cathepsin B contributes to traumatic brain injury-induced cell death through a mitochondria-mediated apoptotic pathway. *J Neurosci Res* 88(13):n/a-n/a.

244. Su S, et al. (2014) DNA methylation of the LY86 gene is associated with obesity, insulin resistance, and inflammation. *Twin Res Hum Genet* 17(3):183–191.

245. Divanovic S, et al. (2005) Inhibition of TLR-4/MD-2 signaling by RP105/MD-1. *J Endotoxin Res* 11(6):363–368.

246. Perego C, Fumagalli S, De Simoni MG (2011) Temporal pattern of expression and colocalization of microglia/macrophage phenotype markers following brain ischemic injury in mice. *J Neuroinflammation* 8(1):174.

247. Chistiakov DA, Killingsworth MC, Myasoedova VA, Orekhov AN, Bobryshev Y V. (2017) CD68/macrosialin: Not just a histochemical marker. *Lab Investig* 97(1):4–13.

248. Cougnoux A, et al. (2020) Toll-like receptor mediated lysozyme expression in Niemann-pick disease, type C1. *Mol Genet Metab*. doi:10.1016/j.ymgme.2020.10.009.

249. Ma J, Jiang T, Tan L, Yu JT (2015) TYROBP in Alzheimer's Disease. *Mol Neurobiol* 51(2):820–826.

250. Cunningham C, Dunne A, Lopez-Rodriguez AB (2019) Astrocytes: Heterogeneous and Dynamic Phenotypes in Neurodegeneration and Innate Immunity. *Neuroscientist* 25(5):455–474.

251. Davies CL, Patir A, McColl BW (2019) Myeloid Cell and Transcriptome Signatures Associated With Inflammation Resolution in a Model of Self-Limiting Acute Brain Inflammation. *Front Immunol* 10(MAY):1048.

252. Lee C-M, et al. Single-cell RNA-seq analysis revealed long-lasting adverse effects of tamoxifen on neurogenesis in prenatal and adult brains. doi:10.1073/pnas.1918883117/-/DCSupplemental.

253. Peng J, et al. (2019) Single-cell RNA-seq highlights intra-tumoral heterogeneity and

malignant progression in pancreatic ductal adenocarcinoma. *Cell Res* 29(9):725–738.

254. Tung PY, et al. (2017) Batch effects and the effective design of single-cell gene expression studies. *Sci Rep* 7(1):1–15.

255. Hicks SC, Townes FW, Teng M, Irizarry RA (2018) Missing data and technical variability in single-cell RNA-sequencing experiments. *Biostatistics* 19(4):562–578.

256. Feigin VL, et al. (2019) Global, regional, and national burden of neurological disorders, 1990–2016: a systematic analysis for the Global Burden of Disease Study 2016. *Lancet Neurol* 18(5):459–480.

257. Timbie KF, Mead BP, Price RJ (2015) Drug and Gene Delivery Across the Blood-Brain Barrier with Focused Ultrasound. *J Control Release* 219:61.

258. Wu SY, et al. (2016) Characterizing Focused-Ultrasound Mediated Drug Delivery to the Heterogeneous Primate Brain in Vivo with Acoustic Monitoring. *Sci Rep* 6(1):1–13.

259. Lee R, Kermani P, Teng KK, Hempstead BL (2001) Regulation of cell survival by secreted proneurotrophins. *Science (80-)* 294(5548):1945–1948.

260. Zhang ZG, et al. (2000) VEGF enhances angiogenesis and promotes blood-brain barrier leakage in the ischemic brain. *J Clin Invest* 106(7):829–838.

261. Liebner S, et al. (2008) Wnt/β-catenin signaling controls development of the blood - brain barrier. *J Cell Biol* 183(3):409–417.

262. Mathew AS, Gorick CM, Price RJ (2021) Single-cell mapping of focused ultrasound-transfected brain. *Gene Ther*. doi:10.1038/s41434-021-00226-0.

263. Zeigler AC, Richardson WJ, Holmes JW, Saucerman JJ (2016) A computational model of cardiac fibroblast signaling predicts context-dependent drivers of myofibroblast differentiation. *J Mol Cell Cardiol* 94:72–81.

264. Tan PM, Buchholz KS, Omens JH, McCulloch AD, Saucerman JJ (2017) Predictive model identifies key network regulators of cardiomyocyte mechano-signaling. *PLoS Comput Biol* 13(11). doi:10.1371/journal.pcbi.1005854.

265. Zeigler AC, et al. (2020) Computational model predicts paracrine and intracellular drivers of fibroblast phenotype after myocardial infarction. *Matrix Biol* 91–92:136–151.

266. Ryall KA, et al. (2012) Network reconstruction and systems analysis of cardiac myocyte hypertrophy signaling. *J Biol Chem* 287(50):42259–42268.

267. Lim JC, et al. (2008) Activation of β-catenin signalling by GSK-3 inhibition increases p-glycoprotein expression in brain endothelial cells. *J Neurochem* 106(4):1855–1865.

268. Lo Dico A, Martelli C, Diceglie C, Lucignani G, Ottobrini L (2018) Hypoxia-inducible factor-1α activity as a switch for glioblastoma responsiveness to temozolomide. *Front Oncol* 8(JUL):249.

269. Kaley TJ, et al. (2019) Phase II trial of an AKT inhibitor (perifosine) for recurrent

glioblastoma. *J Neurooncol* 144(2):403–407.

270. Zheng W, et al. (2020) Inhibition of Cathepsin D (CTSD) enhances radiosensitivity of glioblastoma cells by attenuating autophagy. *Mol Carcinog* 59(6):651–660.

271. Vega R, Carretero M, Travasso RDM, Bonilla LL (2020) Notch signaling and taxis mechanims regulate early stage angiogenesis: A mathematical and computational model. *PLoS Comput Biol* 16(1):e1006919.

272. Kuhn C, Checa S (2019) Computational modeling to quantify the contributions of VEGFR1, VEGFR2, and lateral inhibition in sprouting angiogenesis. *Front Physiol* 10(MAR):288.

273. Kleinstreuer N, et al. (2013) A Computational Model Predicting Disruption of Blood Vessel Development. *PLoS Comput Biol* 9(4):1002996.

274. Stepanova D, Byrne HM, Maini PK, Alarcon T (2021) A multiscale model of complex endothelial cell dynamics in early angiogenesis. *PLoS Comput Biol* 17(1):e1008055.

275. Zhang Y, Kontos CD, Annex BH, Popel AS (2019) Angiopoietin-Tie Signaling Pathway in Endothelial Cells: A Computational Model. *iScience* 20:497–511.

276. Weinstein N, Mendoza L, Álvarez-Buylla ER (2020) A Computational Model of the Endothelial to Mesenchymal Transition. *Front Genet* 11:1.

277. Cho HS, et al. (2016) Localized Down-regulation of P-glycoprotein by Focused Ultrasound and Microbubbles induced Blood-Brain Barrier Disruption in Rat Brain. *Sci Rep* 6. doi:10.1038/srep31201.

278. Guda MR, et al. (2019) GLUT1 and TUBB4 in Glioblastoma could be effcacious targets. *Cancers (Basel)* 11(9). doi:10.3390/cancers11091308.

279. Fallacara AL, et al. (2019) A new strategy for glioblastoma treatment: In vitro and in vivo preclinical characterization of Si306, a pyrazolo[3,4-d]pyrimidine dual Src/P-Glycoprotein inhibitor. *Cancers (Basel)* 11(6). doi:10.3390/cancers11060848.

280. Gareus R, et al. (2008) Endothelial Cell-Specific NF-κB Inhibition Protects Mice from Atherosclerosis. *Cell Metab* 8(5):372–383.

281. Henke N, et al. (2007) Vascular endothelial cell-specific NF-κB suppression attenuates hypertension-induced renal damage. *Circ Res* 101(3):268–276.

282. Gupta SC, Sundaram C, Reuter S, Aggarwal BB (2010) Inhibiting NF-κB activation by small molecules as a therapeutic strategy. *Biochim Biophys Acta - Gene Regul Mech* 1799(10–12):775–787.

283. McDannold N, Vykhodtseva N, Hynynen K (2008) Blood-Brain Barrier Disruption Induced by Focused Ultrasound and Circulating Preformed Microbubbles Appears to Be Characterized by the Mechanical Index. *Ultrasound Med Biol* 34(5):834–840.

284. Chopra R, Vykhodtseva N, Hynynen K (2010) Influence of exposure time and pressure

amplitude on blood-brain-barrier opening using transcranial ultrasound exposures. *ACS Chem Neurosci* 1(5):391–398.

285. Choi JJ, et al. (2010) Microbubble-size dependence of focused ultrasound-induced bloodBrain barrier opening in mice in vivo. *IEEE Trans Biomed Eng* 57(1):145–154.

286. McDannold N, Vykhodtseva N, Hynynen K (2008) Effects of Acoustic Parameters and Ultrasound Contrast Agent Dose on Focused-Ultrasound Induced Blood-Brain Barrier Disruption. *Ultrasound Med Biol* 34(6):930–937.

287. Yang FY, Fu WM, Chen WS, Yeh WL, Lin WL (2008) Quantitative evaluation of the use of microbubbles with transcranial focused ultrasound on blood-brain-barrier disruption. *Ultrason Sonochem* 15(4):636–643.

288. McDannold NJ, Vykhodtseva NI, Hynynen K (2006) Microbubble contrast agent with focused ultrasound to create brain lesions at low power levels: MR imaging and histologic study in rabbits. *Radiology* 241(1):95–106.

289. Tung YS, et al. (2006) Contrast-agent-enhanced ultrasound thermal ablation. *Ultrasound Med Biol* 32(7):1103–1110.

290. O'Reilly MA, Huang Y, Hynynen K (2010) The impact of standing wave effects on transcranial focused ultrasound disruption of the blood-brain barrier in a rat model. *Phys Med Biol* 55(18):5251–5267.

291. Samiotaki G, Konofagou EE (2013) Dependence of the reversibility of focused-ultrasound-induced blood-brain barrier opening on pressure and pulse length in vivo. *IEEE Trans Ultrason Ferroelectr Freq Control* 60(11):2257–2265.

292. van Wamel A, et al. (2006) Vibrating microbubbles poking individual cells: Drug transfer into cells via sonoporation. *J Control Release* 112(2):149–155.

293. Hynynen K, McDannold N, Sheikov NA, Jolesz FA, Vykhodtseva N (2005) Local and reversible blood–brain barrier disruption by noninvasive focused ultrasound at frequencies suitable for trans-skull sonications. *Neuroimage* 24(1):12–20.

294. Freimann FB, et al. (2013) MR elastography in a murine stroke model reveals correlation of macroscopic viscoelastic properties of the brain with neuronal density. *NMR Biomed* 26(11):1534–1539.

295. Et W (2000) *Mutational Analysis of GLUT1 (SLC2A1) in Glut-1 Deficiency Syndrome* doi:10.1002/1098-1004.

296. Rotstein M, et al. (2010) Glut1 deficiency: Inheritance pattern determined by haploinsufficiency. *Ann Neurol* 68(6):955–958.

297. Jinek M, et al. (2012) A programmable dual-RNA-guided DNA endonuclease in adaptive bacterial immunity. *Science (80-)* 337(6096):816–821.

298. Cong L, et al. (2013) Multiplex genome engineering using CRISPR/Cas systems. *Science (80-)* 339(6121):819–823.

299. Kawada K, Iwamoto M, Sakai Y (2016) Mechanisms underlying 18 F-fluorodeoxyglucose accumulation in colorectal cancer . *World J Radiol* 8(11):880.

300. Furuse T, et al. (2019) A new mouse model of GLUT1 deficiency syndrome exhibits abnormal sleep-wake patterns and alterations of glucose kinetics in the brain. *DMM Dis Model Mech* 12(9). doi:10.1242/dmm.038828.

301. Wu SK, et al. (2014) Short-time focused ultrasound hyperthermia enhances liposomal doxorubicin delivery and antitumor efficacy for brain metastasis of breast cancer. *Int J Nanomedicine* 9:4485–4494.

302. Sukovich JR, et al. (2019) In vivo histotripsy brain treatment. *J Neurosurg* 131(4):1331–1338.